# Thickness and structure of the Martian crust from InSight seismic data

Brigitte Knapmeyer-Endrun, Mark P Panning, Felix Bissig, Rakshit Joshi, Amir Khan, Doyeon Kim, Vedran Lekić, Benoit Tauzin, Saikiran Tharimena, Matthieu Plasman, et al.

# Thickness and structure of the Martian crust from InSight seismic data

Brigitte Knapmeyer-Endrun[1]*, Mark P. Panning[2], Felix Bissig[3], Rakshit Joshi[4], Amir Khan[3,5], Doyeon Kim[6], Vedran Lekić[6], Benoit Tauzin[7,8], Saikiran Tharimena[2,9], Matthieu Plasman[10], Nicolas Compaire[11], Raphael F. Garcia[11], Ludovic Margerin[12], Martin Schimmel[13], Éléonore Stutzmann[10], Nicholas Schmerr[6,] E. Bozdağ[14], Ana-Catalina Plesa[15], Mark A. Wieczorek[16], Adrien Broquet[17,16], Daniele Antonangeli[18], Scott M. McLennan[19], Henri Samuel[10], Chloé Michaut[7,20], Lu Pan[21],Suzanne E. Smrekar[2], Catherine L. Johnson[22,23], Nienke Brinkman[3], Anna Mittelholz[3], Attilio Rivoldini[24], Paul M. Davis[25], Philippe Lognonné[10,20], Baptiste Pinot[11], John-Robert Scholz[4], Simon Stähler[3], Martin Knapmeyer[15], Martin van Driel[3], Domenico Giardini[3], W. Bruce Banerdt[2]

[1] Bensberg Observatory, University of Cologne, Vinzenz-Pallotti-Str. 26, 51429 Bergisch Gladbach, Germany.

[2] Jet Propulsion Laboratory, California Institute of Technology; 4800 Oak Grove Dr., M/S 183-301, Pasadena, CA 91109, USA.

[3] Institute of Geophysics, ETH Zurich, Sonneggstr. 5, 8092 Zürich, Switzerland.

[4] Max Planck Institute for Solar System Research, Justus-von-Liebig-Weg 3, 37077 Göttingen, Germany.

[5] Physik-Institut, University of Zurich, Zurich, Switzerland.

[6] University of Maryland, College Park, Department of Geology, 8000 Regents Dr., College Park, MD, 20782-4211, USA.

[7] Université de Lyon, Ecole Normale Supérieure de Lyon, Université Claude Bernard Lyon 1, CNRS, Laboratoire de Géologie de Lyon : Terre, Planètes, Environnement, 69622 Villeurbanne, France.

[8] Research School of Earth Sciences, The Australian National University, Canberra, Australian Capital Territory 0200, Australia.

[9] now at University of Vienna, Althanstrasse 14, 1090 Vienna, Austria.

[10]Université de Paris, Institut de Physique du Globe de Paris, CNRS, F-75005 Paris, France.

[11] Institut Supérieur de l'Aéronautique et de l'Espace SUPAERO, 10 Avenue Edouard Belin, 31400 Toulouse, France.

[12] Institut de Recherche en Astrophysique et Planétologie, Université Toulouse III Paul Sabatier, CNRS, CNES, 14 Av. E. Belin, 31400, Toulouse, France.

[13] Geosciences Barcelona - CSIC, Barcelona, Spain.

[14] Colorado School of Mines, Department of Geophysics, 1500 Illinois Street, Golden, CO 80401, USA.

[15] Institute of Planetary Research, German Aerospace Center (DLR), 12489 Berlin, Germany.

[16] Université Côte d'Azur, Observatoire de la Côte d'Azur, CNRS, Laboratoire Lagrange, France.

[17] Lunar and Planetary Laboratory, University of Arizona, Tucson, AZ 85721, USA.

[18] Sorbonne Université, Muséum National d'Histoire Naturelle, UMR CNRS 7590, Institut de Minéralogie, de Physique des Matériaux et de Cosmochimie, IMPMC, 75005 Paris, France.

[19] Department of Geosciences, Stony Brook University, Stony Brook, NY, 11794-2100, USA.

[20] Institut Universitaire de France.

[21] University of Copenhagen, GLOBE Institute, Center for Star and Planet Formation, Copenhagen, Denmark.

[22] Department of Earth, Ocean and Atmospheric Sciences, University of British Columbia, Vancouver, BC, V6T 1Z4, Canada.

[23] Planetary Science Institute, Tucson, 1700 East Fort Lowell, Suite 106, Tucson, AZ 85719-2395, USA.

[24] Royal Observatory of Belgium, Brussels, Belgium.

[25] Department of Earth, Planetary, and Space Sciences, University of California Los Angeles, CA90095, USA.

*Correspondence to: bknapmey@uni-koeln.de.

**A planet's crust bears witness to the history of planetary formation and evolution, but for Mars, no absolute measurement of crustal thickness was available. Here, we determine the structure of the crust beneath the InSight landing site on Mars using both marsquake recordings and the ambient wavefield. Analyzing seismic phases that are reflected and converted at subsurface interfaces, we find that the observations are consistent with models with at least two, and possibly three interfaces. If the second interface is the boundary of the crust, the thickness is 20±5 km, while if the third interface is the boundary, the thickness is 39±8 km. Global maps of gravity and topography allow extrapolation of this point measurement to the whole planet, showing that the average thickness of the Martian crust lies between 24 and 72 km. Independent bulk composition and geodynamic constraints show that the thicker model is consistent with the abundances of crustal heat-producing elements observed for the shallow surface, whereas the thinner model requires greater concentration at depth.**

**One Sentence Summary:**
Based on multiple approaches, direct seismic measurements constrain global crustal thickness, geochemistry and geodynamic processes.

Planetary crusts form as a result of mantle differentiation and subsequent magmatic processes, including partial melting of mantle reservoirs that may continue to the present day *(1)*. For Mars, the cratering record shows that much of its crust formed early in the planet's history and was accompanied by substantial volcanism *(2,3)*. During both the initial crystallization of a putative magma ocean as well as later-stage partial melting, incompatible components, including heat-producing elements (HPE) and volatiles, concentrated in the melt and were largely sequestered into the crust. The thickness of the crust of Mars thus provides fundamental constraints on how the planet differentiated, how incompatible elements were partitioned among the major silicate reservoirs, and how the planet evolved thermally and magmatically over geologic time *(4-6)*.

Previous estimates of the crustal thickness of Mars and its spatial variations were made by modeling the relationship between gravity and topography. By assuming Airy isostasy and using a restrictive range of crustal densities of 2700-3100 kg $m^{-3}$, the average crustal thickness of the planet was reported to be 57±24 km *(7)*. More recent analyses, however, have used elemental abundances of the surface *(8)* along with major element chemistry of Martian meteorites to argue that the crust could be considerably denser, with values close to ~3300 kg $m^{-3}$. If these higher densities were representative of the underlying crust, the gravity data would allow average crustal thicknesses up to 110 km *(9)*. In contrast, bulk crustal densities lower than previously assumed (~2600 kg $m^{-3}$) have been inferred from gravity analyses and would allow a thinner average crustal thickness *(10)*. Low densities were confirmed locally for the near-surface sediments in Gale crater *(11)* as well as the pyroclastic deposit of the Medusa Fossae Formation *(12)*. Low bulk crustal densities could result from either substantial porosity or the presence of buried silica- and feldspar-rich rocks *(13)*. Silica-rich magmatic rocks are potentially consistent with ancient evolved lithologies identified in Martian meteorite breccias *(14)*.

We used data from the Seismic Experiment for Interior Structure (SEIS) on NASA's InSight mission *(15)* to provide an absolute measurement of Mars' crustal thickness and layering. Our assessment of the crustal structure at the landing site is based on a combination of methods using both converted and reflected seismic phases, in order to resolve trade-offs between the depth of a layer and its seismic velocity *(16)*. By calculating receiver functions *(17,18)*, we extracted P-to-S conversions from the P-wave coda of three seismic events with the clearest P-wave onsets and polarizations. In addition, we applied seismic interferometric techniques by calculating autocorrelations of both ambient noise and event coda using the vertical component. Under

the assumption of a diffuse wavefield, as expected in the case of noise from homogeneously distributed, uncorrelated sources as well as in the coda of high-frequency events, the correlations can be interpreted as zero-offset vertical reflection responses *(19)*. By focusing on the reflected wavefield, the autocorrelations provide independent and complementary information to the receiver function conversion-based methods that make use of the transmitted wavefield *(20)*.

In a previous study *(18)*, we already considered P-to-S receiver functions for two of the same events, but only inverted for the properties of the interface at the base of the shallowest layer (interpreted there as a transition from fractured to unfractured basalt within the crust), causing the first converted arrival at 2.4 s. Including an additional event and applying extensive re-analysis to the data *(16)*, the P-to-S receiver functions for 9 different processing methods *(16)* show three consistent positive arrivals within the first 8 s, but no clear and consistent negative arrivals or later phases (Fig. 1A). As all three events are located at epicentral distances between 25° and 59° *(21,22)*, no strong move-out of either direct arrivals or multiple reflections is expected, which impedes the unambiguous identification of multiples. The third positive arrival at 7.2-7.5 s could be either simply a PpPs multiple of the first arrival at 2.4 s (ray path 3 in Fig. 2B), or contain additional energy from a direct conversion from a third, deeper discontinuity (ray path 3 in Fig. 2D). We applied two inversion approaches to the P-to-S receiver functions *(16)*, and both can match the three clear peaks with either two (Fig. 2A-B) or three interfaces (Fig. 2C-D). In both inversion approaches, our models showed robust and consistent depths of the two shallowest interfaces. The first layer with a thickness of 6-11 km and an S-wave velocity between 1.2 and 2.1 km/s is consistent with the previous results for the shallow crust *(18)*, whereas a second interface is found at 15-25 km depth independent of the model parameterization. The third interface, the existence of which is supported but not absolutely required by the data, showed greater variability in depth between different inversion choices and generally required a smaller velocity contrast at the base of this layer than for the shallower second interface (Figs. S18, S19). Based on the ensemble of models from the two inversion approaches, our results are consistent with either a local crustal thickness at the InSight landing site of 15-25 km, when the base of layer 2 is the Moho (thin crust models), or 27-47 km, when the base of layer 3 is the Moho (thick crust models; Figs. 2, S18, S19). S-to-P receiver functions can also be calculated for 2 events (S0173a and S0235b; Figs. S4, S6, S7) and both show a signal consistent with conversion at the first interface, while S0235b also shows possible arrivals consistent with deeper conversions *(16)*. Further support for the P-to-S receiver function-derived models is provided by waveform fits in inversions for source mechanisms *(16)*, where a strong interface around 24 km depth is required to match S-precursors.

Vertical component autocorrelations based on different data sets and processing algorithms *(16,23)* show consistent energy maxima in the 5 to 6 s, 10 to 11 s, and 20 to 21.5 s time ranges (Fig. 3). Comparison with predicted arrival times from representative models produced by the receiver function inversion shows that these energy maxima can be explained by P-wave reflections in those models interacting with the first two interfaces, without any clear observations requiring the third interface. Previously published autocorrelations *(24)* contain an arrival near 10 s that is consistent with our results, and which can be explained as a P-wave reflection from the bottom of the second layer at around 22 km depth. A second arrival reported by *(24)* near 20 s, that is also present in many of the autocorrelation functions calculated here, is consistent with a multiple reflection from that layer (Fig. 3). These arrivals were interpreted by Deng and Levander *(24)* as P and S reflections, respectively, from a crust-mantle discontinuity at a depth of 35 km. However, we do not expect a strong S reflection in a vertical autocorrelation as vertically propagating S waves are horizontally polarized. Interpreting the second arrival as a multiple P reflection instead is consistent with our receiver function-derived results and more likely to be observed in a vertical component autocorrelation. The previously published crustal thickness estimate of 35 km based on autocorrelations *(24)* is consistent with the possible range of the thick crust models, but the specific arrivals identified in that study are more consistent with a reflection and multiple from the shallower second interface around 20 km depth.

We inverted for the thickness of the crust at global scale using the seismically-estimated thickness at the InSight landing site and observed gravity field as constraints *(16)*. Our models consider the gravity of hydrostatic relief along density interfaces beneath the lithosphere, surface relief, variations in thickness of a constant density crust, and the low-density polar cap deposits *(25)*. We employed several different interior pre-landing models *(26)* that specify the density profile of the mantle and core, and for each, we constructed crustal thickness models for all permissible crustal densities. For a given seismic thickness, the mean thickness of the crust depends almost exclusively on the density contrast across the crust-mantle interface (Fig. S22). To ensure that the thickness of the crust is positive within the major impact basins, each reference model has a maximum permissible crustal density. If the thin crust seismic model is used as a constraint, the global mean crustal thickness is predicted to lie between 24 and 38 km and the maximum permissible density of the crust is 2850 kg $m^{-3}$ (Figs. 4, S22, S23). For the thick crust seismic model, the average crustal thickness lies between 39 and 72 km and the maximum permissible crustal density is 3100 kg $m^{-3}$ (Figs. 4, S22, S23). For both seismic constraints, the crustal density is substantially less than would be expected based on the composition of surface materials *(9)*, which is close to 3300 kg $m^{-3}$. The lower bulk densities are signatures of highly altered layers and can be accounted for by the presence of more than 5% porosity in the crust on average, the presence of fluids or low-density cements filling fractures and pore space, the existence of abundant petrologically evolved felsic rocks beneath the surface layer, or a combination thereof.

The seismic observations argue for a relatively thin crust, or at least thinner than some earlier predictions *(9)*, providing constraints on crustal heat production and the degree of planetary silicate differentiation (Fig. 4). As the present-day crustal thickness is the outcome of the planet's differentiation history *(27,28)*, geodynamic and geologic modeling can place constraints on the composition of the crust and of the mantle, and on the cooling rate of the planet *(16)*. Our results indicate that average crustal thickness models that are consistent with the thick crust seismic model are compatible with currently accepted bulk *(29,30)* and crustal *(8,31)* heat producing element contents, and the occurrence of present-day melting only in an ascending plume below the thickened crust of the Tharsis province (Fig. S27). Such a scenario implies a crust that is about 13 times more enriched in heat producing elements than the primitive mantle (Fig. S24), consistent with 55-70% of the Martian heat producing elements being sequestered into the crust. In contrast, the thin crust seismic model requires a crust that is about 21 times more enriched than a relatively cold primitive mantle (Fig. S25). This is more than two times larger than estimates from gamma-ray spectroscopy data which constrains the surface layer of the crust (Table S6) and would point towards an enrichment in heat-producing elements beneath the surface layer *(16)*. Furthermore, this would call for an efficient process of incompatible element extraction from the mantle, possibly by upward segregation during the solidification of a magma ocean, or by a secondary differentiation mechanism, as for the continental crust of Earth. In both crustal models, assuming a Wänke and Dreibus *(29)* bulk composition, the present-day heat flux is predicted to lie between 20 and 25 mW $m^{-2}$ (Fig. 4). The depth to the crust-mantle boundary, as well as layering in the crust can further constrain crustal magnetization amplitudes, depending on whether the magnetization is carried in upper or lower crustal layers, or both *(16)*. We can also investigate whether crustal thickness and density models are consistent with moment-of-inertia measurements and constraints on the properties of Mars core from the $k_2$ tidal Love number *(16)*. Generally, these constraints are easier to match for most mantle composition models with the thick crust seismic models, although some models also allow for the thin crust model. Overall, when considering geodynamic, geochemical, and geodetic constraints, the thin crust models place tighter constraints on the density and enrichment of heat producing elements within the crust, as well as on the mantle composition, than the thick crust models, but neither of the two can be excluded.

**References and Notes:**

1. L. T. Elkins-Tanton, Magma oceans in the inner solar system. *Annu. Rev. Earth. Planet. Sci.* **40**, 113-139 (2012).

2. M. Grott et al., Long-term evolution of the Martian crust-mantle system. *Space Sci. Rev.* **174**, 49-111 (2013).
3. F. Nimmo, K. Tanaka, Early crustal evolution of Mars. *Annu. Rev. Earth Planet. Sci.* **33**, 133-161 (2005).
4. D. Breuer, W.B. Moore, "10.08—Dynamics and thermal history of the terrestrial planets, the Moon, and Io", in *Treatise on Geophysics*, G. Schubert Ed. (Elsevier, Oxford, ed. 2, 2015), pp. 255–305.
5. S. A. Hauck II, R. J. Philips, Thermal and crustal evolution of Mars. J. Geophys. Res. 107, 5052 (2002).
6. A.-C. Plesa et al., The thermal state and interior structure of Mars. *Geophys. Res. Lett.* **45**, 12198-12209 (2018).
7. M. A. Wieczorek, M. T. Zuber, Thickness of the Martian crust: Improved constraints from geoid-to-topography ratios. *J. Geophys. Res.* **109**, E01009 (2004).
8. B. C. Hahn, S. M. McLennan, E. C. Klein, Martian surface heat production and crustal heat flow from Mars Odyssey Gamma-Ray spectrometry. *Geophys. Res. Lett.* **38**, L14203 (2011).
9. D. Baratoux et al., Petrological constraints on the density of the Martian crust. *J. Geophys. Res.* **119**, 1707– 1727 (2014).
10. S. Goossens et al., Evidence for a low bulk crustal density for Mars from gravity and topography. *Geophys. Res. Lett.* **44**, 7686– 7694 (2017).
11. K. W. Lewis et al., A surface gravity traverse on Mars indicates low bedrock density at Gale crater. *Science* **363**, 535-537 (2019).
12. L. Ojha, K. Lewis, The density of the Medusae Fossae Formation: Implications for its composition, origin, and importance in Martian history. *J. Geophys. Res.* **123**, 1368– 1379 (2018).
13. V. Sautter et al., In situ evidence for continental crust on early Mars. *Nature Geoscience* **8**, 605-609 (2015).
14. M. Humayun et al., Origin and age of the earliest Martian crust from meteorite NWA7533. *Nature* **503**, 513-516 (2013).
15. P. Lognonné et al., SEIS: Insight's Seismic Experiment for Internal Structure of Mars. *Space. Sci. Rev.* **215**, 12 (2019).
16. Methods and additional materials are available as supplementary materials on Science Online.
17. C. A. Langston, Structure under Mount Rainier, Washington, inferred from teleseismic body waves. *J. Geophys. Res.* **84**, 4749-4762 (1979).
18. P. Lognonné et al., Constraints on the shallow elastic and anelastic structure of Mars from InSight seismic data. *Nature Geoscience* **13**, 213-220 (2020).
19. K. Wapenaar, D. Draganov, R. Snieder, X. Campman, A. Verdel, Tutorial on seismic interferometry: Part 1—Basic principles and applications. *Geophysics* **75**, 75A195-75A209 (2010).
20. D. Kim, V. Lekić, Groundwater variations from autocorrelations and receiver functions. *Geophys. Res. Lett.* **46**, 13722-13729 (2019).
21. D. Giardini et al., The seismicity of Mars. *Nature Geoscience* **13**, 205- 212 (2020).
22. A. Khan et al., Imaging the upper mantle structure of Mars with InSight seismic data. *Science*, submitted (2021).
23. N. Compaire et al., Autocorrelation of the ground vibrations recorded by the SEIS-InSight seismometer on Mars. *J. Geophys. Res*. **126**, e2020JE006498, doi:10.1029/2020JE006498 (2021).
24. S. Deng, A. Levander, Autocorrelation Reflectivity of Mars, Geophys. Res. Lett. 47, e2020GL089630 (2020).
25. M. A. Wieczorek, M. Beuthe, A. Rivoldini, T. Van Hoolst. Hydrostatic interfaces in bodies with nonhydrostatic lithospheres, J. Geophys. Res. Planets, 124, doi:10.1029/2018JE005909 (2019).

26. S. E. Smrekar et al., Pre-mission InSights on the Interior of Mars. *Space Sci Rev* **215**, 3 (2019). https://doi.org/10.1007/s11214-018-0563-9.
27. H. Samuel, P. Lognonné, M. Panning, V. Lainey, The rheology and thermal history of Mars revealed by the orbital evolution of Phobos, *Nature* **569**, 523–527 (2019).
28. M. Thiriet, C. Michaut, D. Breuer, A. C. Plesa, Hemispheric dichotomy in lithosphere thickness on Mars caused by differences in crustal structure and composition, *J. Geophys. Res. Planets* **123**, 823–848 (2018).
29. H. Wänke, G. Dreibus, Chemistry and accretion history of Mars, *Philos. Trans. R. Soc. London. Ser. A Phys. Eng. Sci.* **349**, 285–293 (1994).
30. G. J. Taylor, The bulk composition of Mars, *Geochemistry* **73**, 401-420 (2013).
31. S. R Taylor, S. M McLennan, Planetary Crusts: Their composition, origin and evolution (Cambridge Univ. Press, Cambridge, 2009).
32. InSight Mars SEIS Data Service, SEIS raw data, InSight Mission, IPGP, JPL, CNES, ETHZ, ICL, MPS, ISAE-Supaero, LPG, MFSC, https://doi.org/10.18715/SEIS.INSIGHT.XB_2016 (2019).
33. D. L. Abt, K. M. Fischer, S. W. French, H. A. Ford, H. Yuan, B. Romanowicz, North American lithospheric discontinuity structure imaged by Ps and Sp receiver functions. *J. Geophys. Res.* **115**, B09301 (2010).
34. B. Knapmeyer-Endrun, F. Krüger, the PASSEQ Working Group, Moho depth across the Trans-European Suture Zone from P- and S-receiver functions. *Geophys. J. Int.* **197**, 1048–1075 (2014).
35. J. F. Lawrence, P. M. Shearer, A global study of transition zone thickness using receiver functions. *J. Geophys. Res.*, **111**, B0630 (2006).
36. L. Vinnik, H. Chenet, J. Gagnepain-Beyneix, P. Lognonné, First seismic receiver functions on the Moon. *Geophys. Res. Lett.* **28**, 3031–3034 (2001).
37. P. Lognonné, J. Gagnepain-Beyneix, H. Chenet. A new seismic model of the Moon: implication in terms of structure, formation and evolution. *Earth Planet. Sci. Lett.* **112**, 27–44 (2003).
38. J.-R. Scholz et al., Detection, analysis and removal of glitches from InSight's seismic data from Mars. *Earth and Space Science* **7**, e2020EA001317-T, doi:10.1029/2020EA001317 (2020).
39. J. M. Kolb, V. Lekic, Receiver function deconvolution using transdimensional hierarchical Bayesian inference. *Geophys. J. Int.* **193**, 1791-1735 (2014).
40. B. L. N. Kennett, The removal of free surface interactions from three-component seismograms. *Geophys. J. Int.*, **104**, 153-163 (1991).
41. R. W. Clayton, R. A. Wiggins, Source shape estimation and deconvolution of teleseismic bodywaves, *Geophys. J. Int*. **47**, 151-177, doi:10.1111/j.1365-246X.1976.tb01267.x (1976).
42. J. P. Ligorria, C. J. Ammon, Iterative deconvolution and receiver-function estimation. *Bull. Seism. Soc. Am.* **89**, 1395-1400 (1999).
43. R. Kind, G. L. Kosarev, N. V. Petersen, Receiver functions at the stations of the German Regional Seismic Network (GRSN). *Geophys. J. Int* **121**, 191-202 (1995).
44. K. Hannemann, F. Krüger, T. Dahm, D. Lange, Structure of the oceanic lithosphere and upper mantle north of the Gloria Fault in the eastern mid-Atlantic by receiver function analysis. *J. Geophys. Res.* **122**, 7927-7950 (2017).
45. G. Helffrich, Extended-time multitaper frequency domain cross-correlation receiver function estimation. *Bull. Seism. Soc. Am.* **96**, 344-347 (2006).
46. T. Shibutani, T. Ueno, K. Hirahara, Improvement in the extended-time multitaper receiver function estimation technique. *Bull. Seis. Soc. Am.* **98**, 812-816 (2008).
47. Eagar, K.C., M.J. Fouch, FuncLab: A MATLAB interactive toolbox for handling receiver function datasets, *Seis. Res. Lett.* **83**, doi:10.1785/gssrl.83.3.596, (2012).
48. G. D. Bensen et al., Processing seismic ambient noise data to obtain reliable broad-band surface wave dispersion measurements. *Geophys. J. Int.* **169**, 1239–1260 (2007).

49. R. S. M. De Plaen, T. Lecocq, C. Caudron, V. Ferrazzini, O. Francis, Single-station monitoring of volcanoes using seismic ambient noise. *Geophys. Res. Lett.* **43**, 8511–8518 (2016).
50. Y. Ito, K. Shiomi, Seismic scatterers within subducting slab revealed from ambient noise autocorrelation. *Geophys. Res. Lett.* **39**, L19303 (2012).
51. F. J. Sánchez-Sesma, M. Campillo, Retrieval of the Green's function from cross correlation: the canonical elastic problem. *Bull. Seism. Soc. Am.* **96**, 1182-1191 (2006).
52. R. Snieder, Extracting the Green's function from the correlation of coda waves: A derivation based on stationary phase. *Phys. Rev. E* **69**, 046610 (2004).
53. W. Sun, B. L. N. Kennett, Receiver structure from teleseisms: Autocorrelation and cross correlation. *Geophys. Res. Lett.* **43**, 6234–6242 (2016).
54. InSight Marsquake Service, Mars Seismic Catalogue, InSight Mission; V1 2/1/2020. ETHZ, IPGP, JPL, ICL, ISAE-Supaero, MPS, Univ. Bristol. doi:10.12686/a6 (2020).
55. D. Clarke, L. Zaccarelli, N. M. Shapiro, F. Brenguier. Assessment of resolution and accuracy of the Moving Window Cross Spectral technique for monitoring crustal temporal variations using ambient seismic noise. *Geophys. J. Int.* **186**, 867–882 (2011).
56. M. Schimmel et al., Seismic Noise Autocorrelations on Mars. *Earth and Space Science Open Archive*, doi: 10.1002/essoar.10506669.1 (2021).
57. S. Ceylan et al., Companion guide to the marsquake catalog from InSight, Sols 0–478: Data content and non-seismic events. *Physics Earth Planet. Int.* **310**, 106597, doi:10.1016/j.pepi.2020.106597 (2021).
58. M. Schimmel, Phase cross-correlations: design, comparisons and applications. *Bull. Seismol. Soc. Am.* **89**, 1366-1378 (1999).
59. G. Taylor, S. Rost, G. Houseman, Crustal imaging across the North Anatolian Fault Zone from the autocorrelation of ambient seismic noise. *Geophys. Res. Lett.* **43**, 2502–2509, doi: 10.1002/2016GL067715 (2016).
60. P. Romero, M. Schimmel, Mapping the basement of the Ebro Basin in Spain with seismic ambient noise autocorrelations. *J. Geophys. Res.* **123**, 5052-5067, doi: 10.1029/2018JB015498 (2018).
61. M. Schimmel, E. Stutzmann, S. Ventosa, Low-frequency ambient noise autocorrelations: Waveforms and normal modes. *Seism. Res. Lett.* **89** (4), 1488-1496, doi: 10.1785/0220180027 (2018).
62. C. Buffoni, M. Schimmel, N.C. Sabbione, M.L. Rosa, G. Connon, Crustal structure beneath Tierra del Fuego, Argentina, inferred from seismic P-wave receiver functions and ambient noise autocorrelations. *Tectonophysics* **751**, 41-53, doi: 10.1016/j.tecto.2018.12.013 (2019).
63. S. Ventosa, M. Schimmel, E. Stutzmann, Towards the processing of large data volumes with phase cross-correlation. *Seism. Res. Lett.* **90**(4), 1663-1669, doi: 10.1785/0220190022 (2019).
64. M. Schimmel, J. Gallart, Frequency-dependent phase coherence for noise suppression in seismic array data. *J. Geophys. Res.*, **112**, B04303, doi:10.1029/2006JB004680 (2007).
65. M. Schimmel, E. Stutzmann, J. Gallart, Using instantaneous phase coherence for signal extraction from ambient noise data at a local to a global scale. *Geophys. J. Int.* 184, 494-506, doi: 10.1111/j.1365-246X.2010.04861.x (2011).
66. T. S. Pham, H. Tkalčić, On the feasibility and use of teleseismic P wave coda autocorrelation for mapping shallow seismic discontinuities. *J. Geophys. Res.* **122**, 3776-3791 (2017).
67. J. C. VanDecar, R. S. Crosson, Determination of teleseismic relative phase arrival times using multi-channel cross-correlation and least squares. *Bull. Seism. Soc. Am.* **80**, 150-169 (1990).
68. F. Bissig et al., Multifrequency Inversion of Ps and Sp Receiver Functions: Methodology and Application to USArray Data. *J. Geophys. Res.* **126**, e2020JB020350, doi: 10.1029/2020JB020350 (2021).
69. A. Khan et al., A geophysical perspective on the bulk composition of Mars. *J. Geophys. Res.* **123**, 1-37, doi: 10.1002/2017JE005371 (2018).

70. K. Fuchs, G. Müller, Computation of synthetic seismograms with the reflectivity method and comparison with observations. *Geophys. J. Int.* **23**, 417-433, doi:10.1111/j.1365-246X.1971.tb01834.x (1971).
71. H. P. Crotwell, T. J. Owens, J. Ritsema, The TauP Toolkit: Flexible seismic travel-time and ray-path utilities. *Seismol. Res. Lett.* **70**, 154-160, doi:10.1785/gssrl.70.2.154 (1999).
72. K. Mosegaard, A. Tarantola, Monte Carlo sampling of solutions to inverse problems. *J. Geophys. Res.* **100**, 12431-12447, doi:10.1029/94JB03097 (1995).
73. A. Tarantola, Inverse problem theory and methods for model parameter estimation. Society of Industrial and Applied Mathematics (2005).
74. K. Mosegaard, A. Tarantola, Probabilistic Approach to Inverse Problems. In: International Handbook of Earthquake and Engineering Seismology, 237-265. Academic Press (2002).
75. M. Wathelet, An improved neighborhood algorithm: Parameter conditions and dynamic scaling. *Geophys. Res.Lett.* **35**, L09301 (2008).
76. M. Sambridge, Geophysical inversion with a neighbourhood algorithm–I. Searching a parameter space. *Geophys. J. Int.* **138**, 479–494 (1999).
77. R. Joshi, B. Knapmeyer-Endrun, K. Mosegaard, H. Igel, U. Christensen, Joint inversion of receiver functions and apparent incidence angles for sparse seismic data. *Earth and Space Science Open Archive*, doi:10.1002/essoar.10506471.1 (2021).
78. T. Shibutani, M. Sambridge, B. Kennett, Genetic algorithm in-version for receiver functions with application to crust and uppermost mantle structure beneath eastern Australia. *Geophys. Res. Lett.* **23**, 1829–1832 (1996).
79. T. Nissen-Meyer et al., AxiSEM: Broadband 3-D seismic wavefields in axisymmetric media. *Solid Earth* **5**, 425–445 (2014).
80. B. Knapmeyer-Endrun, S. Ceylan, S., M. van Driel, Crustal S-wave velocity from apparent incidence angles: a case study in preparation for InSight. *Space Sci. Rev.* **214**, 83 (2018).
81. F. Birch, The velocities of compressional waves in rocks to 10 kilobars, Part 2. *J. Geophys. Res.* **66**, 2199–2224 (1961).
82. N. Brinkman et al., First focal mechanisms of marsquakes. *J. Geophys. Res.* **126**, e2020JE006546, (2021).
83. M. A. Wieczoreket al., The crust of the Moon as seen by GRAIL. *Science* **339**, 671-675 (2013).
84. T. Yoshizaki, W. F. McDonough, The composition of Mars. *Geochim. Cosmochim. Acta* **273**, 137-162 (2020).
85. M. A. Wieczorek and R. J. Phillips, Potential anomalies on a sphere: Applications to the thickness of the lunar crust, *J. Geophys. Res*. **103**(E1), 1715-1724 (1998).
86. A. Broquet et al., Flexure of the lithosphere beneath the North Polar Cap of Mars: Implications for ice composition and heat flow. *Geophys. Res. Lett*. **47**, e2019GL086746 (2020).
87. M. A. Wieczorek, Gravity and Topography of the Terrestrial Planets. *Treatise on Geophysics*, 2nd edition, Oxford, 153-193 (2015).
88. A. Genova et al., Seasonal and static gravity field of Mars from MGS, Mars Odyssey and MRO radio science, *Icarus* **272**, 228-245 (2016).
89. T. Ruedas, D. Breuer, On the relative importance of thermal and chemical buoyancy in regular and impact-induced melting in a Mars-like planet, *J. Geophys. Res. Planets* **122**, 1554–1579 (2017).
90. E. Takahashi, Speculations on the Archean mantle: missing link between komatiite and depleted garnet peridotite, *J. Geophys. Res.* **95**, 15941–15954 (1990).
91. M. Duncan, N. Schmerr, C. M. Bertka, Y. Fei, Extending the solidus for a model iron-rich Martian mantle composition to 25 GPa. *Geophys. Res. Lett.* **45**, 10,211– 10,220 (2018). https://doi.org/10.1029/2018GL078182
92. A. C. Plesa, N. Tosi, M. Grott, D. Breuer, Thermal evolution and Urey ratio of Mars. *J. Geophys. Res. Planets* **120**, 995–1010 (2015).

93. N. Tosi, M. Grott, A.C. Plesa, D. Breuer, Thermochemical evolution of Mercury's interior. *J. Geophys. Res. E Planets* **118**, 2474–2487 (2013).
94. A. Plesa et al., How large are present-day heat flux variations across the surface of Mars? *J. Geophys. Res.* **121**, 2386–2403 (2016).
95. W. K. Hartmann, Evidence for recent volcanism on Mars from crater counts. *Nature* **397**, 586–589 (1999).
96. G. Neukum, Recent and episodic volcanic and glacial activity on Mars revealed by the High Resolution Stereo Camera, *Nature* **432**, 971–979 (2004).
97. M. Thiriet, D. Breuer, C. Michaut, A.-C. Plesa, Scaling laws of convection for cooling planets in a stagnant lid regime. *Phys. Earth Planet. Inter.* **286**, 138–153 (2019).
98. W. V. Boynton et al., Concentration of H, Si, Cl, K, Fe, and Th in the low- and mid-latitude regions of Mars. *J. Geophys. Res.* **112**, E12S99, doi:10.1029/2007JE002887 (2007).
99. H. E. Newsom et al., Geochemistry of Martian soil and bedrock in mantled and less mantled terrains with gamma ray data from Mars Odyssey. *J. Geophys. Res.* **112**, E03S12, doi:10.1029/2006JE002680 (2007).
100. H. Y. McSween Jr, S. M. McLennan, Mars. In: H. D. Holland and K. Turekian, eds., Treatise on Geochemistry, 2nd Ed.; Vol. 2, A. M. Davis, ed., Planets, Asteroids, Comets and The Solar System (Elsevier, Amsterdam) pp. 251-300 (2014).
101. C. B. Agee et al. Unique meteorite from early Amazonian Mars: Water-rich basaltic breccia Northwest Africa 7034. *Science* **339**, 780-785, doi_10.1126/science.1228858 (2013).
102. B. C.Hahn, B. C. et al., Mars Odyssey gamma-ray spectrometer elemental abundances and apparent relative surface age: Implications for martian crustal evolution. *J. Geophys. Res.* **112**, E03S11, doi:10.1029/2006JE002821 (2007).
103. S. Karunatillake et al., Chemically striking regions on Mars and Stealth revisited. *J. Geophys. Res.* **114**, E12001, doi:10.1029/2008JE03303 (2009).
104. G. J. Taylor et al., Mapping Mars geochemically. *Geology* **38**, 183-186, doi:10.1130/G30470 (2010).
105. P. L. King, S. M. McLennan, Sulfur on Mars. *Elements* **6**, 107-112 (2010).
106. C. L. Johnson et al., Crustal and time-varying magnetic fields at the InSight landing site on Mars. *Nature Geoscience* **13**, 199-204 (2020).
107. B. Langlais et al. A new model of the crustal magnetic field of Mars using MGS and MAVEN. *J. Geophy. Res.* **124**, 1542-1569 (2019).
108. A. Mittelholz, C. L. Johnson, A. Morschhauser. A new magnetic field activity proxy for Mars from MAVEN data. *Geophys. Res. Lett.* **45**, 5899-5907 (2018).
109. R. L. Parker, Ideal bodies for Mars magnetics. *J. Geophys. Res*. **108**, 5006 (2003).
110. A. Mittelholz, C. L. Johnson, J. M. Feinberg, B. Langlais, R. J. Phillips, Timing of the martian dynamo: New constraints for a core field 4.5 and 3.7 Ga ago. *Science Advance*s **6** (2020).
111. A. S. Konopliv et al. Detection of the Chandler wobble of Mars from orbiting spacecraft. *Geophys. Res. Lett.* **47**, e2020GL090568, doi:10.1029/2020GL090568 (2020).
112. D. Kahan et al., Mars precession rate determined from radiometric tracking of the InSight lander. *Planet. Space Sci.* **199**, 105208, doi:10.1016/j.pss.2021.105208 (2021).
113. M. P. Panning et al., Planned products of the Mars structure service for the InSight mission to Mars. *Space Sci. Rev.* **211**, 611–650 (2017).
114. A. Rivoldini, T. Van Hoolst, O. Verhoeven, A. Mocquet, V. Dehant, Geodesy constraints on the interior structure and composition of Mars. *Icarus* **213**, 451-472, doi: 10.1016/j.icarus.2011.03.024 (2011).
115. J. A. D. Connolly, Computation of phase equilibria by linear programming: A tool for geodynamic modeling and its application to subduction zone decarbonation. *Earth Planet. Sci. Lett.* **236**, 524-541, doi: 10.1016/j.epsl.2005.04.033 (2005).
116. L. Stixrude, C. Lithgow-Bertelloni, Thermodynamics of mantle minerals - II. Phase equilibria. *Geophys. J. Int.* **184**, 1180–1213, doi:10.1111/j.1365-246X.2010.04890.x (2011).

117. G. J. Taylor et al., Variations in K/Th on Mars. *J. Geophys. Res.* **111**, E03S06, doi:10.1029/2006JE002676 (2007).

**Acknowledgments:** This is Insight Contribution Number (ICN) 187. We acknowledge NASA, CNES, their partner agencies and Institutions (UKSA, SSO, DLR, JPL, IPGP-CNRS, ETHZ, IC, MPS-MPG) and the flight operations team at JPL, SISMOC, MSDS, IRIS-DMC and PDS for providing SEED SEIS data. **Funding:** MPP, ST, EB, SES, and WBB were supported by the NASA InSight mission and funds from the Jet Propulsion Laboratory, California Institute of Technology, under a contract with the National Aeronautics and Space Administration. FB was supported by research grant ETH-05 17-1. AK, DG, MVD and SS acknowledge funding by the Swiss National Science Foundation, the Swiss State Secretariat for Education, Research and Innovation, and support from ETHZ through the ETH+ funding scheme (ETH+02 19-1). VL and DK acknowledge funding from Packard Foundation Fellowship to VL. BT is supported by the European Union's Horizon 2020 research and innovation program under the Marie Sklodowska-Curie grant agreement 793824. French co-authors acknowledge the support of CNES and ANR (MAGIS, ANR-19-CE31-0008-08). NS was supported by NASA Grant 80NSSC18K1628. EB was funded through NASA Participating Scientist Program Grant 80NSSC18K1680. ACP gratefully acknowledges the financial support and endorsement from the DLR Management Board Young Research Group Leader Program and the Executive Board Member for Space Research and Technology. Geodynamical models used in this work were performed on the supercomputer ForHLR funded by the Ministry of Science, Research and the Arts Baden-Württemberg and by the Federal Ministry of Education and Research. SMM was funded through NASA InSight Participating Scientist Program Award No. 80NSSC18K1622. CM acknowledges the support of the Institut Universitaire de France (IUF). CLJ and AM acknowledge support from the InSight Mission, the Canadian Space Agency and ETH Zurich (ETH fellowship 19-2 FEL-34). NB is supported by research grant ETH-06 17-02. The work of AR was financially supported by the Belgian PRODEX program managed by the European Space Agency in collaboration with the Belgian Federal Science Policy Office. **Author contributions:** BKE, MPP, FB, RJ, AK, DK, VL, BT, ST, MP, NC, RFG, LM, MS, ES, NS, ACP, MW, DA, SMM, HS, CM, LP, SES, CLJ, PL, MK, DG and WBB contributed to the conceptualization of this study. The applied methodologies were developed by BKE, FB, RJ, AK, DK, VL, BT, ST, MP, NC, RFG, LM, MS, ES, ACP, MW, HS, CM, LP, PMD, PL, BP and JRS. BKE, FB, RJ, AK, DK, NC, MS, ES, ACP, MW, HS, CM, PMD, PL, BP and JRS developed, implemented and tested used software. BKE, MPP, NS, NB and MVD provided validation. Formal analyses were conducted by BKE, RB, RJ, AK, DK, VL, BT, ST, MP, NC, MS, ES, ACP, MW, AB, HS, CM, CLJ, NB, AM, AR, PMD, PL, BP, JRS and SS. BKE, FB, RJ, AK, DK, VL, ST, MP, NC, MS, ES, ACP, MW, SMM, HS, CM, CLJ, NB, AM, AR, PMD, PL, BP, JRS and SS provided investigations. Data curation activities were done by PL, SS, MVD and DG. BKE, MPP, FB, RJ, AK, DK, VL, BT, ST, NC, RFG, LM, MS, ES, ACP, MW, SMM, HS, CM, CLJ, NB, AM, AR and PMD contributed to the writing of the original draft. Review and editing were performed by BKE, MPP, NS, EB, AB, DA, SES, CLJ and MK. BKE, MPP, FB, RJ, AK, DK, VL, BT, NC, MS, ES, NS, ACP, MW, HS, CM, AM, AR and PMD worked on visualizing the results. BKE, MPP, AK, RFG, LM, NS, CLJ, PL and DG supervised junior scientists involved in the project. The project was administrated by SES, PL, DG and WBB, who also acquired funding. **Competing interests:** Authors declare no competing interests. **Data and materials availability:** All InSight SEIS data *(32)* used in this paper are available from the IPGP Data Center, IRIS-DMC and NASA PDS.

**Supplementary Materials:**

Materials and Methods

Figures S1-S29

Tables S1-S6

References (33-117)

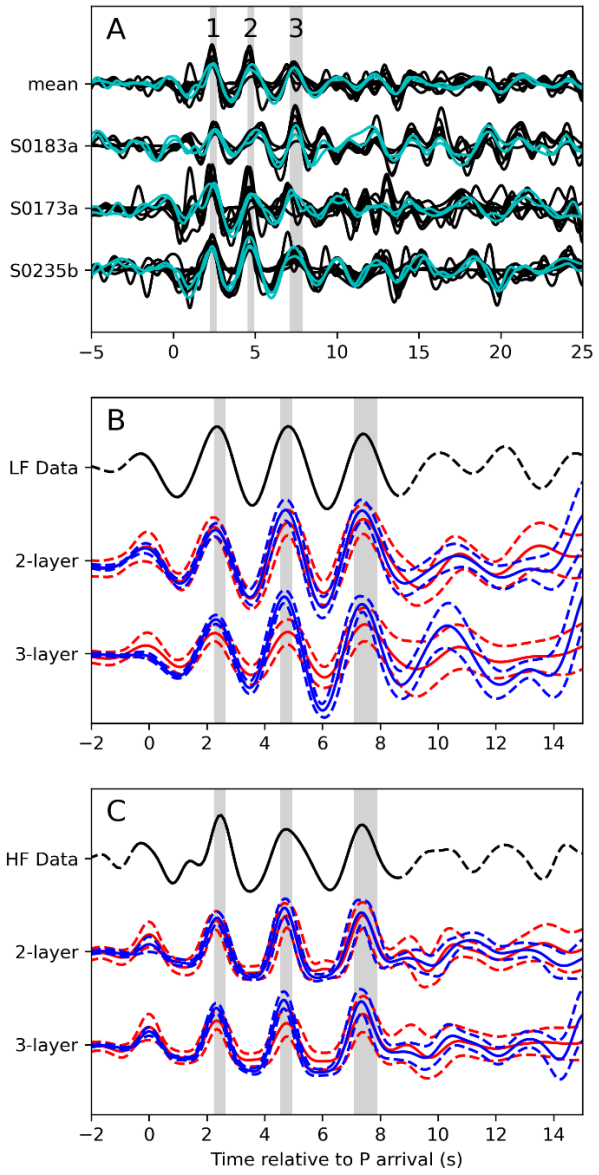


**Fig. 1.** Measured and modeled converted phases that constrain the crustal structure at the InSight landing site. (**A**) P-to-S receiver functions for the three events considered, and the summed trace. Different traces for each event correspond to different processing methods as described in the Supplementary Materials. Gray shading highlights the three clear positive phases within the first 8 s. Numbered labels correspond to predicted ray paths shown in Fig. 2B,D. The two datasets used for model inversions shown in Fig. 2 are highlighted in cyan. (**B**) Comparison between the low-frequency representative receiver function sum trace and synthetic summed P-to-S receiver functions for the 2- and 3-layer models. Data is shown in black on top, with the time window used in the inversion drawn solid. Solid and dashed red lines show the synthetics computed by the range of models produced by inversion method A *(16)*, while solid and dashed blue lines show the mean receiver functions with standard deviations based on the 5000 best fitting receiver functions derived from inversion method B *(16)*. Gray shaded regions are the same as in **(A)**. **(C)** Same as panel **(B)**, but for the high-frequency receiver functions.

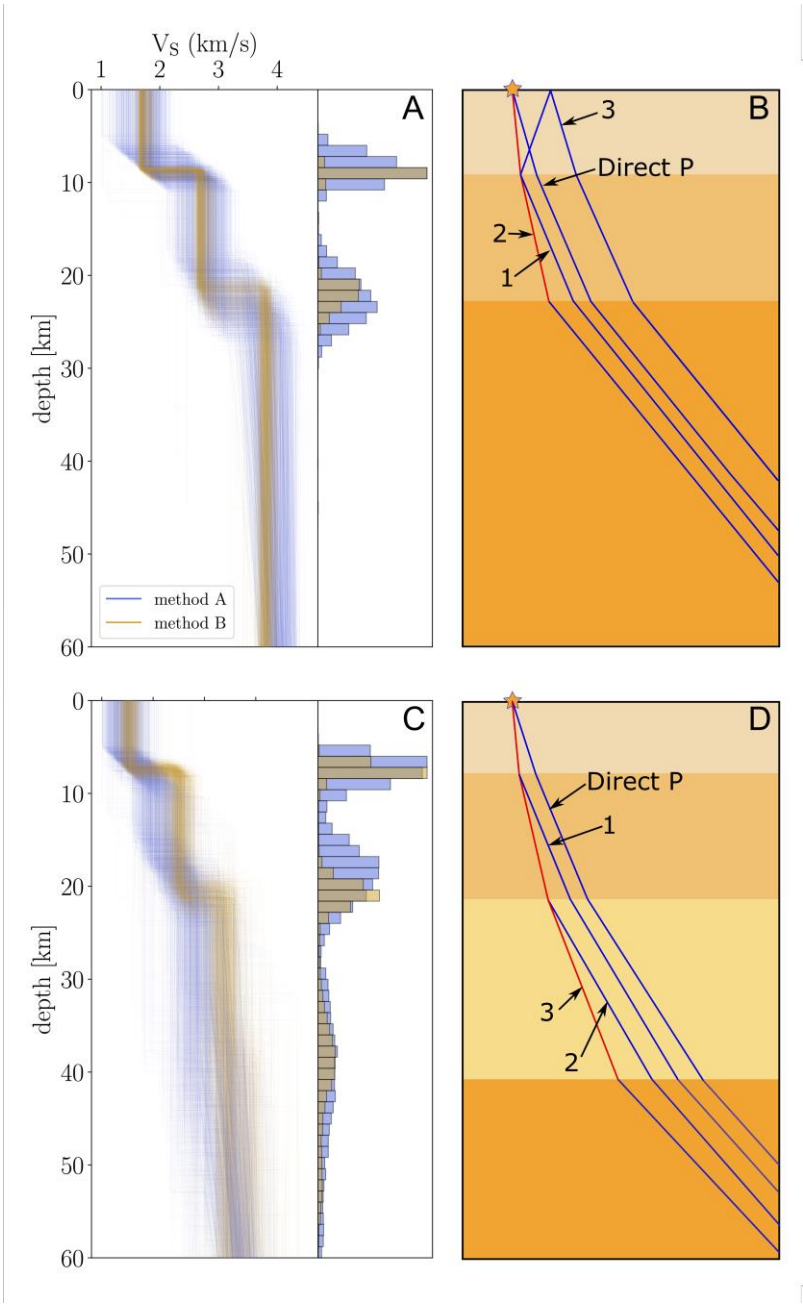


**Fig. 2.** Synopsis of the crustal structure of Mars at the InSight landing site from receiver function analyses. **(A)** Inversion results for all three events using inversion method A (in blue lines) and method B (in brown) using a two-layer parameterization. **(B)** Cartoon showing the ray paths of the main direct and converted phases present in the data. Blue lines show P phase paths, while the red lines show conversions to S phases at the interfaces below the lander. Direct conversions and one P multiple are shown and numbered labels correspond to arrivals identified in Fig. 1A. **(C-D)** Same as **(A-B)**, except for assuming a three-layer model and excluding the multiple arrival.

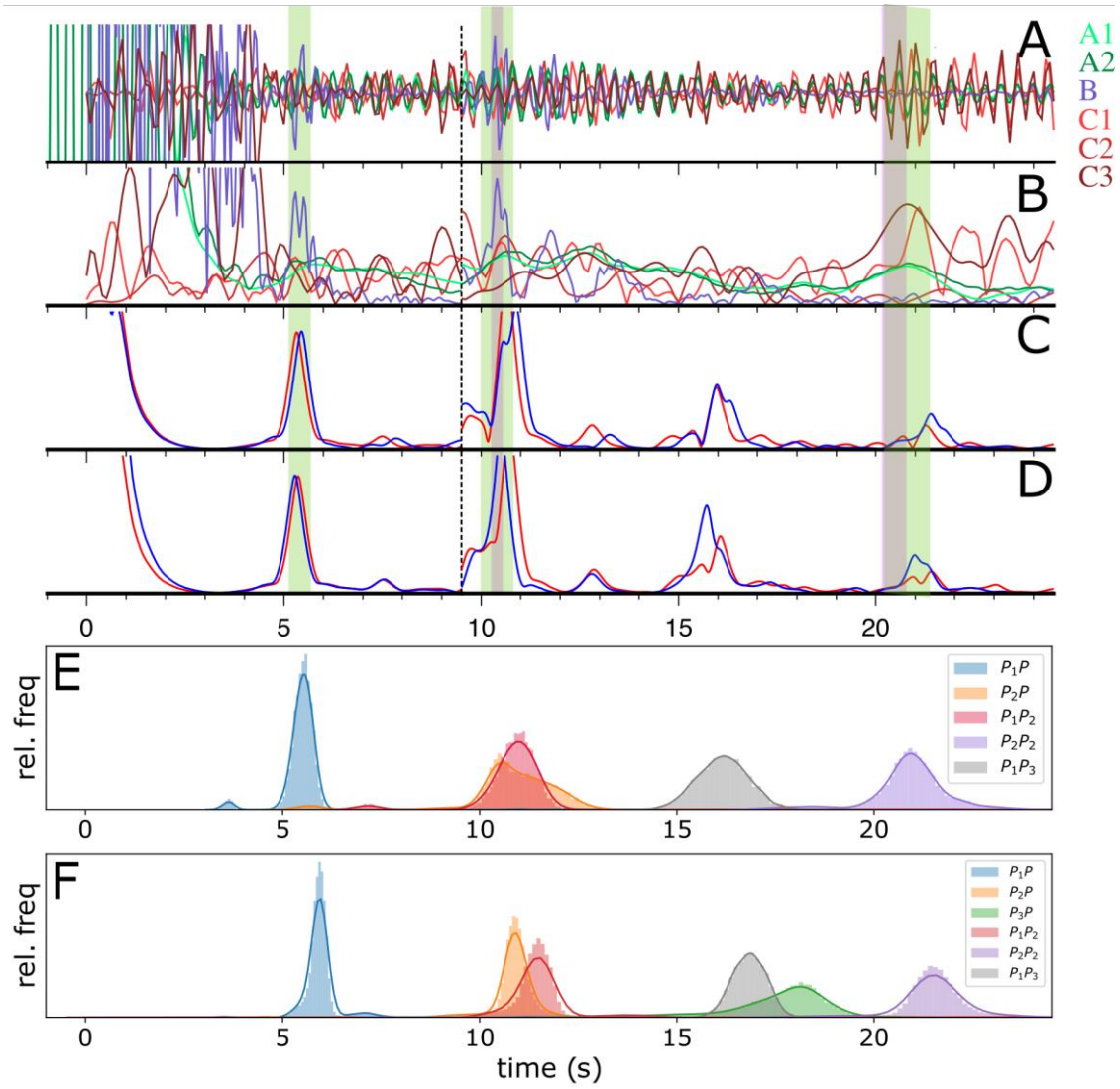


**Fig. 3.** Autocorrelation functions for different data sets, components, and processing methods. **(A)** Overlaid traces are from the three analysis methods discussed in the supplementary material. The dashed bar at 9.5 s corresponds to a change in normalization in order to see smaller amplitude arrivals later in the trace. Green bars highlight areas where all methods are nearly in-phase and show potential arrivals, whereas purple bars highlight arrivals indicated from an independent study *(24)*. **(B)** Envelopes of the ACFs displayed in **(A)**. **(C)** Envelopes of synthetic zero-offset Green's functions for a representative model from the family of two-layer models in Fig. 2A for method A in blue and method B in red. **(D)** Same as **(C)**, but for the three-layer models from Fig. 2C. **(E)** Histograms of predicted arrivals from the family of two-layer models as shown in Fig. 2A. The first subscript of the arrival in the legend refers to the interface of reflection, and the second subscript (if present) represents a second or third bounce between the free surface and that interface. **(F)** Same as **(E)**, but for the three-layer models in Fig. 2C.

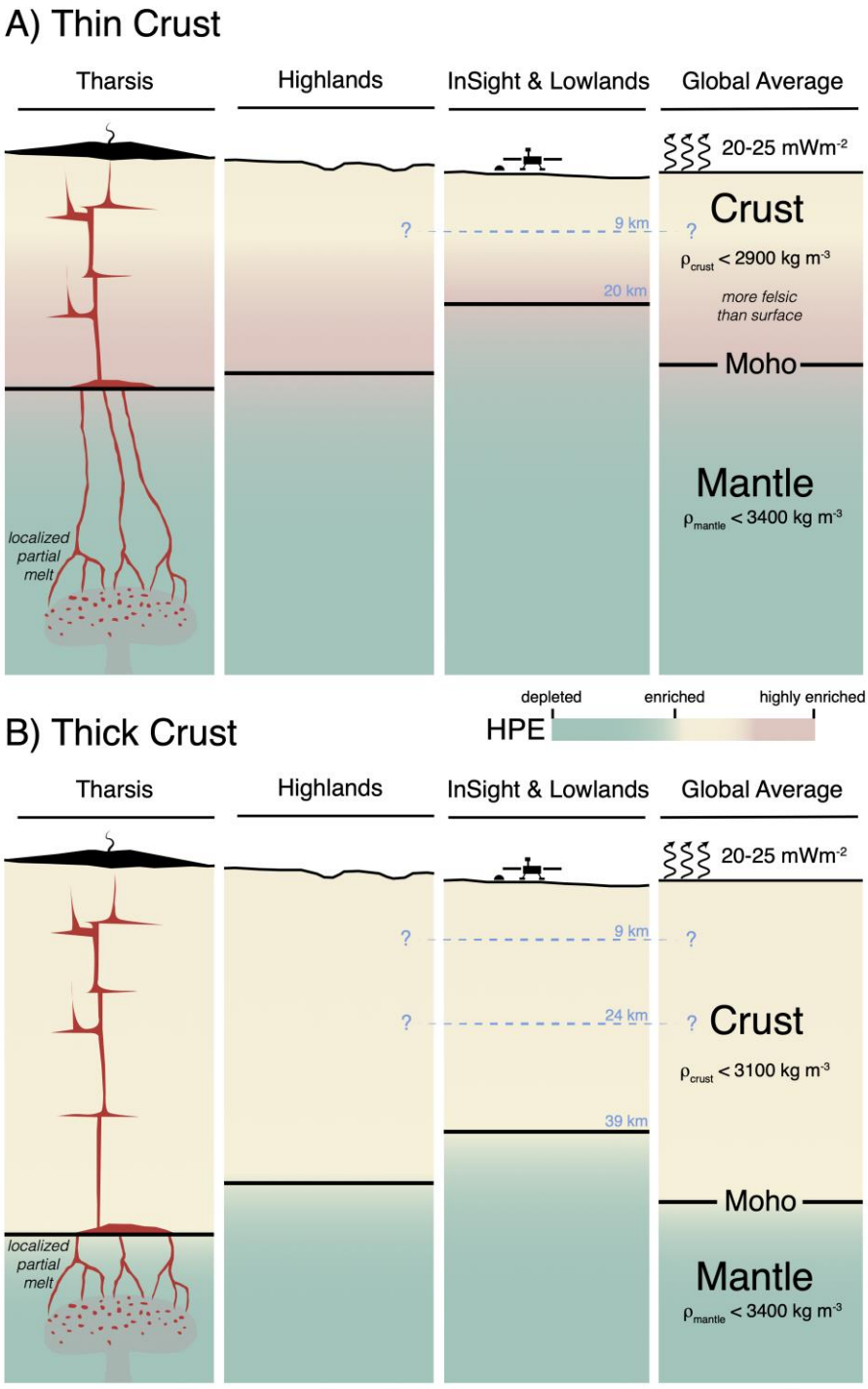


**Fig. 4.** Schematic interpretations of the geochemical and geodynamical implications for the thin and thick crust models (**A** and **B**, respectively). In order to match geodynamic constraints, an enrichment of heat producing elements, shown in color, and lower density than observed from the surface are required in the thin crust model, whereas the thick crust model is consistent with surface observations.

# Supplementary Materials for

## Thickness and structure of the Martian crust from InSight seismic data

Brigitte Knapmeyer-Endrun[1]*, Mark P. Panning[2], Felix Bissig[3], Rakshit Joshi[4], Amir Khan[3,5], Doyeon Kim[6], Vedran Lekić[6], Benoit Tauzin[7,8], Saikiran Tharimena[2,9], Matthieu Plasman[10], Nicolas Compaire[11], Raphael F. Garcia[11], Ludovic Margerin[12], Martin Schimmel[13], Éléonore Stutzmann[10], Nicholas Schmerr[6,] E. Bozdağ[14], Ana-Catalina Plesa[15], Mark A. Wieczorek[16], Adrien Broquet[17],[16], Daniele Antonangeli[18], Scott M. McLennan[19], Henri Samuel[10], Chloé Michaut[7,20], Lu Pan[21], Suzanne E. Smrekar[2], Catherine L. Johnson[22,23], Nienke Brinkman[3], Anna Mittelholz[3], Attilio Rivoldini[24], Paul M. Davis[25], Philippe Lognonné[10,20], Baptiste Pinot[11], John-Robert Scholz[4], Simon Stähler[3], Martin Knapmeyer[15], Martin van Driel[3], Domenico Giardini[3], W. Bruce Banerdt[2]

[1] Bensberg Observatory, University of Cologne, Vinzenz-Pallotti-Str. 26, 51429 Bergisch Gladbach, Germany.

[2] Jet Propulsion Laboratory, California Institute of Technology; 4800 Oak Grove Dr., M/S 183-301, Pasadena, CA 91109, USA.

[3] Institute of Geophysics, ETH Zurich, Sonneggstr. 5, 8092 Zürich, Switzerland.

[4] Max Planck Institute for Solar System Research, Justus-von-Liebig-Weg 3, 37077 Göttingen, Germany.

[5] Physik-Institut, University of Zurich, Zurich, Switzerland.

[6] University of Maryland, College Park, Department of Geology, 8000 Regents Dr., College Park, MD, 20782-4211, USA.

[7] Université de Lyon, Ecole Normale Supérieure de Lyon, Université Claude Bernard Lyon 1, CNRS, Laboratoire de Géologie de Lyon : Terre, Planètes, Environnement, 69622 Villeurbanne, France.

[8] Research School of Earth Sciences, The Australian National University, Canberra, Australian Capital Territory 0200, Australia.

[9] now at University of Vienna, Althanstrasse 14, 1090 Vienna, Austria.

[10] Université de Paris, Institut de Physique du Globe de Paris, CNRS, F-75005 Paris, France.

[11] Institut Supérieur de l'Aéronautique et de l'Espace SUPAERO, 10 Avenue Edouard Belin, 31400 Toulouse, France.

[12] Institut de Recherche en Astrophysique et Planétologie, Université Toulouse III Paul Sabatier, CNRS, CNES, 14 Av. E. Belin, 31400, Toulouse, France.

[13] Geosciences Barcelona - CSIC, Barcelona, Spain.

[14] Colorado School of Mines, Department of Geophysics, 1500 Illinois Street, Golden, CO 80401, USA.

[15] Institute of Planetary Research, German Aerospace Center (DLR), 12489 Berlin, Germany.

[16] Université Côte d'Azur, Observatoire de la Côte d'Azur, CNRS, Laboratoire Lagrange, France.

[17] Lunar and Planetary Laboratory, University of Arizona, Tucson, AZ 85721, USA.

[18] Sorbonne Université, Muséum National d'Histoire Naturelle, UMR CNRS 7590, Institut de Minéralogie, de Physique des Matériaux et de Cosmochimie, IMPMC, 75005 Paris, France.

[19] Department of Geosciences, Stony Brook University, Stony Brook, NY, 11794-2100, USA.

[20] Institut Universitaire de France.

[21] University of Copenhagen, GLOBE Institute, Center for Star and Planet Formation, Copenhagen, Denmark.

[22] Department of Earth, Ocean and Atmospheric Sciences, University of British Columbia, Vancouver, BC, V6T 1Z4, Canada.

[23] Planetary Science Institute, Tucson, 1700 East Fort Lowell, Suite 106, Tucson, AZ 85719-2395, USA.

[24] Royal Observatory of Belgium, Brussels, Belgium.

[25] Department of Earth, Planetary, and Space Sciences, University of California Los Angeles, CA90095, USA.

Correspondence to: bknapmey@uni-koeln.de

## This PDF file includes:

Materials and Methods
Figs. S1-S29
Tables S1-S6

## Materials and Methods

### S1. Receiver functions

The P-to-S receiver function (RF) method is based on the assumption that the P-component of a teleseismic P-wave recording approximates the source and distant path effects in the three-component seismogram. The P-component is obtained by removal of the instrument response, and transfer of the recorded seismograms into the ray coordinate system. Then, deconvolution of the P- from the SV-component of the P-wave and its coda results in the impulse response of the subsurface for transmitted S-waves, the so-called receiver function (*17*). On Earth, this is a standard method for determining and mapping crustal and upper mantle structure (*33-35*). The S-to-P RF method is based on the same principle, but uses P-precursors to the S-wave. It has the additional benefit that, while direct S-to-P conversions arrive before the S-onset, all multiply converted and reflected phases arrive after it. S-to-P receiver functions have previously been applied to extract crustal structure from the Apollo lunar data (*36,37*). Fig. S1 shows seismograms of two events for which precursors to the S-wave onset can tentatively be identified on the vertical component before any further processing. The timing of the initial precursor is consistent with the phase observed in S-to-P receiver functions (see sections S1.1, S1.3, and S1.4).

P-to-S RFs were calculated by seven groups using nine different algorithms and parameter settings for the rotation and deconvolution steps. This allows assessing the influence of a specific processing method on the resulting receiver function waveform. The different algorithms are described briefly below and summarized in Tab. S1. In contrast to the previous analysis of two events for shallow crustal layering *(18)*, RFs are calculated in the LQT ray coordinate system here instead of the ZRT system. While this involves an additional rotation around the P-wave incidence angle that needs to be determined from the data first, it has the advantage of better separating P- and SV-energy on the L- and Q-component, respectively, and thus, by removing energy from multiple P-wave reflections, providing a cleaner P-to-S RF. The P-wave recording of event S0173a contained a prominent glitch on all three components, and a deglitching method was first applied to remove this glitch (*18,38*). All P-to-S receiver functions are plotted overlaid on each other in Fig. 1A, and on the same scale but offset for clarity in Fig. S2. While the general shape of the different RFs and the timing of the prominent arrivals within the first 8 seconds is generally consistent between different methods, the frequency content and the amplitude of the arrivals varies, with higher frequencies contained in the RFs resulting from processing methods A1, A2, B1, C2, D, E1 and E2 compared to B2, C1, F and G. Accordingly, we chose one set of high-frequency and one set of low-frequency RFs as exemplary data sets representing the range of RFs for the inversions (section S3), to investigate both the effect of differences in RF processing and in inversion method on the resulting models. S-to-P RFs were calculated by a subset of three groups. The methods used are also detailed below and summarized in Tab. S1.

### S1.1 Method A: (Vedran Lekic, Doyeon Kim)

We computed P-to-S and S-to-P RFs of two Mars events, S0173a and S0235b using transdimensional hierarchical Bayesian deconvolution (THBD, *39*). Instead of a single deconvolved timeseries, our method yields an ensemble of RFs for each event, whose features appear in proportion to their likelihood. We carried out one million iterations of the THBD, discarding the first half as burn-in, and saving every 1000th sample to the ensemble. A window between 8 to 9 seconds in duration, starting at the P- or S-arrival, was applied to remove later

arriving phases and pre-event noise while minimizing abrupt waveform truncation (dashed line, Fig. S3). We then estimated the up-going P and SV energy using a free surface transform matrix (*40*), using published back azimuths of 91° and 74° for S0173a and S0235b (*21*), respectively, and performing a grid-search on values of $V_P$, $V_P/V_S$, and ray parameter that minimize the correlation between the P and SV waveforms within 2 and 5 seconds of the P- and S arrival, respectively. To maximize the signal-to-noise ratio of the RFs, we also estimated two noise parameters that characterize the decay and oscillation rates of the noise correlation function derived from pre-event data. All of the parameters for processing the RFs are shown in Fig. S4 (see Fig. 1A for the suite of RFs computed by different methods).

S1.2 Method B: (Benoit Tauzin)

P-to-S RFs were computed for events S0173a, S0183a, S0235b and S0325a. Broadband records in the UVW system were deconvolved from the VBB instrumental response, synchronized, and rotated to the vertical-north-east (ZNE) system using information from the response file on May 23, 2019 (components azimuth and dip, poles and zeros). The information from MQS about the arrival times of the P-wave was then used to find the teleseismic P-wave coda on the records, and to normalize the traces with respect to the amplitude of the P-wave on the Z component. The onset time of the P-wave was measured by band-pass filtering (4th order Butterworth, forward and reverse) records within the 0.1-0.9 Hz frequency-band and picking the onsets on the Z component. The records are further analyzed to find the azimuths of arrival and polarizations of the P-waves in the vertical plane through principal component analysis, for component rotation from ZNE to PSvSh. The aligned and normalized waveforms were trimmed over a 5 s-long window after the onset of the P-wave. Covariance matrices were obtained (i) from the N and E components, for rotation from ZNE to vertical-radial-transverse (ZRT) directions, and (ii) from Z and R components for rotation from ZRT to the PSvSh system. Estimates for the best azimuth and polarization direction for the P-wave were obtained from the eigenvector direction minimizing the energy on the T and Sv components. The RFs were obtained from two methods, water-level deconvolution (*41*) and iterative time-domain deconvolution (*42*). The source was trimmed within -10 to +25 s from the P-wave onset, and tapered using a Tukey window. A low-pass Gaussian filter with parameter a = 3.0 rad/s was used in both cases. See Fig. S5 for the final RFs.

S1.3 Method C: (Felix Bissig, Amir Khan)

In order to compute P-to-S and S-to-P RFs for the events S0173a, S0183a, and S0235b, we first detrended and tapered waveforms in the ZNE-system and subsequently filter them by means of a Butterworth bandpass filter of 2nd order with corner periods at 2 and 10 sec or 1 and 8 sec, respectively. The former is referred to as “low-frequency”, the latter as “high-frequency” RFs, respectively. Seismograms were rotated to the ZRT-system on the basis of back-azimuth estimates provided by the MQS. Rotation to the LQT-system to further separate P- and SV-waves was achieved via a principal-component analysis approach, minimizing the energy on the R-/Z-component ±30 sec around the estimated P-/S-wave for P-to-S and S-to-P RFs, respectively. P- and S-wave arrival times were provided by MQS. For computing RFs, we utilized the iterative time-domain deconvolution (*42*), which requires appropriate estimates of the source- and response-signals. We therefore cut the L-/Q-components to [-20, +50 sec] around the picked P-wave for P-to-S RFs and to [-150, +50 sec] and [-100, +30 sec] around the S-wave for S-to-P RFs, respectively, and tapered them using a Hanning-window. Different source- and

response-windows were tested, but their influence on the final RF was found to be small. The so-obtained RFs were filtered between periods of 2 sec and 10 sec or 1 and 8 sec for low- and high-frequency RFs, respectively. See Fig. S6 for the final RFs.

S1.4 Method D: (Brigitte Knapmeyer-Endrun)

Data of events S0173a, S0183a, and S0235b were response corrected, rotated to the ZNE system and filtered by a Butterworth zero-phase bandpass of third order with corner periods at 0.1 and 0.8 Hz in the case of S0173a and S0235b and 0.3 and 0.8 Hz in the case of S0183a. Data were rotated to the ZRT system using the back-azimuth estimates by MQS, i.e. 91°, 74° and 73°, respectively. For further rotation to the LQT-system, the incidence angles were determined by polarization analysis via diagonalizing the coherence matrix of the P-wave onset. RFs were calculated by creating a time-domain Wiener filter that transforms the P-wavetrain on the P component into a band-limited spike (*43*,*44*). The three-component seismogram traces were then folded with the spiking filter to obtain the RFs. Various window lengths for the P-wave train, damping factors, and spike positions within the window were tested. The parameters actually used are deconvolution window length of 40 s for S0173a, 28 s for S0183a and 33 s for S0235b, with the spike position at the centroid of the signal (i.e., at 18.4 s, 11.5 s, and 14.4 s), and a damping factor of 0.1 for S0173a, 0.5 for S0235b and 1 for S0183a. Resulting P-to-S RFs, together with results for two additional, more noisy events, are shown in Fig. S7A. For these two events, S0407a and S0325a, only a distance estimate, but no azimuth was available from MQS. Thus, for determining the azimuths, a set of radial RFs were calculated after rotating the horizontal components of the waveform in 10° steps and compared to the radial RFs for the other three events, with special attention to the three arrivals within the first 8 s. The comparison pointed to a likely azimuth of 110±10° for S0325a and 90±10° for S0407a. The corresponding RFs still tend to have a lower signal-to-noise ratio than those of the three previous events, though, and stacking all five events only leads to small changes in the average waveform compared to the stack of only the three best events.

S-to-P RFs were computed in a similar fashion to P-to-S RFs for events S0235b, S0173a and S0325a. Results show a clear peak at 2.9 s, regardless of whether only data of S0235b and S0173a or all three events are stacked, and hints of later arrivals that are however not consistent between all three events (Fig. S7B).

S1.5 Method E: (Saikiran Tharimena)

The data for events S0173a, S0183a, and S0235b were corrected for the instrument response in the UVW system, and the resulting velocity seismograms were trimmed to 10 min before and 15 min after the P-wave arrival time as reported by MQS. For the S0173a event, deglitched data were also corrected for the instrument response. Data were rotated to the ZNE system and then to the ZRT system using back-azimuths of 91°, 73°, and 74° respectively, as reported by MQS. Furthermore, the waveforms were rotated to the LQT system, which separates P- and SV- energy on the L- and Q- components respectively. The incidence angles for rotation to the LQT system were estimated by principal component analysis where P-wave energy, around the estimated P-wave arrival, was minimized on the SV component. A second order Butterworth, zero-phase bandpass filter was applied with corners at 1 and 10s. The time axis of the resulting waveforms was centered on the P-wave arrival.

P-to-S receiver functions were calculated using the iterative time-domain deconvolution (ITD, *42*) and extended-time multi-taper deconvolution (EMTD, *45*) methods. For the ITD

method, the waveform in a time window 30s before and after the P-wave arrival on the L-component was chosen as source function and a Gaussian filter parameter of 5 rad/s was used. For the EMTD method, the source waveform was chosen on the L-component by manually selecting a window around the visible P-wave arrival. Deconvolution was then performed using a 50s window, a time-bandwidth product of 3 that translates to a frequency bandwidth of permissible spectral leakage of 0.2 Hz, and 4 tapers (*46*). For both methods, the source function was deconvolved from the SV component. Different time windows for the source function were tested and found to produce similar results.

S1.6 Method F: (Matthieu Plasman)

Data of events S0173a, S0183a and S0235b were detrended, response corrected and first rotated to the geographical system (ZNE). We then applied a Butterworth band-pass filter between 0.1 and 0.8 Hz for S0235b and S0173a and between 0.3 and 0.8Hz for S0183a and a symmetric taper using a Hanning-window. We next rotated data to the ZRT system using the back-azimuth estimated by MQS, i.e. 91°, 74° and 73°, respectively. We then finally rotated to the LQT system using the same incident angles computed in method D (18° for S0183a, 24.5° for S0235b and 29.5° for S0173a). RFs were computed from an iterative time-domain deconvolution on a 95 s time window (15s before P and 80s after) with a Gaussian width of 2.5s (*42*). The quality of the computed Q-RF is defined by how well it reproduces the initial Q signal when convolved with the source signal on the L-component. The recovered RFs reproduce 73.3%, 76.7% and 76.9% of the Q-component, respectively, for S0173a, S0183a and S0235b.

S1.7 Method G (Paul Davis):

Receiver functions were generated from 20 sample-per-second UVW deglitched data (*38*) taken 3 sec before the P arrival and 30 sec after for events S0173a, S0235b, S0183a, S0105a, S0325a, S0395a, S0421b. The data were corrected for the instrument response, filtered with a causal, 4-pole, bandpass, Butterworth filter between 0.25 and 0.8 Hz, and rotated, as in Method F to the LQT system using surface velocities of Vp=3.5 km/s and Vs=1.95 km/s. The receiver function analysis used Chuck Ammon's water level code, with water level 0.1 (*41,47*). The three events with known azimuths and ray parameter values (S0173a, S023b, S0183a) were used to construct a summed reference receiver function, $R_{ref}$ (Fig. S8). We then tested all 28 deglitched event RFs for cross-correlation with $R_{ref}$, finding the maximum correlation by varying their unknown azimuths between 0 and 360 degrees in 10-degree steps, and setting the ray parameter inversely proportional to distance (determined by P-S times). Events with a cross-correlation greater than 0.5 were retained and are shown in Fig. S9. The 4 extra events, so found, are S0105a, S0325a, S0395a, and S0421b.

S2. Autocorrelations

S2.1 Method A (Nicolas Compaire, Ludovic Margerin, Raphael F. Garcia,)

To compute the autocorrelation functions (ACF) of the ambient noise recorded by SEIS, we based our approach on the workflow of Bensen et al. (*48*), but with two important differences. First, we compute the ACF by LMST (Local Mean Solar Time) hour, and not by day as it is the case in Bensen et al. *(47)*. This allows us to check the stability of the reconstructed Green's functions over the duration of a SOL (martian day). Second, we apply a modified version of the pre-processing of De Plaen et al. (*49*) which has been tested in single-station configurations. The only difference lies in the special attention given to the effect of the spectral normalization on the

waveforms of the ACF. Similar to De Plaen et al. (*49*) and Ito and Shiomi (*50*), we do not apply any spectral whitening. This choice can result in a reconstruction of the Green's function of lesser quality because the required equipartition of energy is not ensured. Nevertheless, it prevents us from adding pre-processing artefacts to the ACF waveforms. Moreover, it has been shown by various studies (*51,52*) that the equipartition of energy is only required to perfectly retrieve the Green's function. The various phase arrivals can be reconstructed without this prerequisite, which is the primary goal of this study.

Each trace of one LMST hour duration is band-passed and cut into windows of 60 seconds duration with 70% overlap. One-bit normalization is applied to these windows in order to remove the effect of transient signals (*48*). The normalized autocorrelations were computed in the spectral domain and then linearly stacked in time domain to improve the Signal-to-Noise Ratio (SNR). The resulting stacked function is the ACF computed for a particular LMST hour and a particular SOL.

In order to compute the ACF on the scattered part of the seismic event recordings (e.g. *52,53*), we applied the same processing. When a clear S-phase is visible, we used it as the beginning of the coda time window of interest, otherwise the whole duration of the seismic event is used. Obviously, no subdivision in LMST hours was applied in that case. The event nomenclature refers to the catalogue of the MarsQuake Service (MQS) *(54,23*).

After the computation of the ACFs, we performed a SNR analysis over the correlation lag-time using the definition given in Clarke el al. (*55*). This SNR is defined as the ratio of the envelope of the stack to the variance over the realizations (the various SOLs for the ACF computed on ambient noise and the various events for the ACF computed on the events). This SNR is a good indicator of the reliability of the phase arrivals.

Our analysis validates energy arrivals in the ACF when the amplitude of the waveforms are large, the SNR is high and the same energy arrival is retrieved for different types of data (background noise and events). With such criteria in mind, Fig. S10A suggests that four arrivals are visible in the various datasets (at 5.6 s, 10.6 s, 12.6 s and 21 s) on the vertical ACF. Fig. S10B suggests several arrivals in the North ACF at 11.9 s, 14.4 s, 16.5 s and 22.4 s. Fig. S10C suggests arrivals in the East ACF at 9.0 s, 12.4 s and 14.5 s. A conservative estimate of the error bar of these arrival times is 1 s. Only the frequency range of 1-3 Hz, which is dominated by a broad amplification around 2.4 Hz, is considered for the noise auto-correlations because only in this frequency range, during nighttime, high SNR values are observed (*23*). The ACFs of the 2.4Hz events, High Frequency events (HF) and Very High Frequency events (VF) are also computed between 1 Hz and 3 Hz because it is in this frequency band that these events have the major part of their energy.

### S2.2 Method B (Martin Schimmel, Eleonore Stutzmann)

In the following analysis, the main data pre-processing steps are correction to ground velocity, data segmentation and selection, and frequency band-pass filtering. These are common processing steps to prepare the data for the computation of autocorrelations. Often, these steps are expanded by amplitude normalization, such as by one-bit normalization and/or spectral whitening, to reduce bias due to outlying signals. Here, we do not make use of any amplitude normalization processing steps and focus our analysis on the vertical component VBB data at 20 samples-per-second (Sol 178-410).

Our data segmentation and selection *(56)* deviates from what is commonly used. In this step, we basically determine the seismic root-mean-square (RMS) amplitude variability with time. The measured RMS variability is then used to build a mask to select data segments without abrupt changes in the RMS amplitude. Data irregularities such as glitches and donks have an elevated RMS variability and are therefore excluded from further processing. Here, we use this data segmentation and selection step to build a smaller subsidiary dataset with a size of about 30% of the total data volume. The selected dataset contains only recordings with the lowest RMS amplitude variability. This processing step is justified since InSight seismic data contains many aseismic transient signals inherent to the difficult acquisition conditions *(18,57)*.

Further pre-processing consists only in filtering the data to the desired frequency bands and to attenuate the strongest lander modes and tick noise through three band rejection filters. The autocorrelations are computed using the Phase Cross-Correlation (PCC; *58*). This method is based on analytic signal theory and finds the coherent signals through their instantaneous phase coherence as a function of lag time. The approach is amplitude unbiased. PCC has proven to be efficient in various seismic monitoring and imaging studies, including ambient noise autocorrelation research (*59-62*; among others). It works in analogy to the classical correlation and can also be employed in a computationally efficient manner to process large data volumes (*63*).

The computed autocorrelograms are then stacked both linearly and employing time-frequency phase weighted stacking (tf-PWS; *64,65*) for comparison. tf-PWS can further attenuate incoherent signals because it uses the instantaneous phase coherence.

Fig. S11 shows an autocorrelogram section for three-sol long, non-overlapping time windows. Negative amplitudes are in blue. The considered frequency band is 1.2-8.9 Hz and the three-sol binned autocorrelograms are stacked using tf-PWS. The figure shows three lag time windows to improve the visibility of signals through amplitude normalization in each of the lag time windows. The blue arrows mark signals which coincide with the expected P-to-P wave reflections (Fig. 3 D,E) for the proposed discontinuities. Similarly, the green arrows point to P-to-S or S-to-P reflection conversions from the same discontinuities. Fig. S11 presents these signals as stable features over the considered time span. Also note that the 6.14 s signal has a higher frequency content than the other signals. Further, this figure reveals the presence of other signals which have not yet been identified.

The total data stacks using the tf-PWS are shown with red lines in Fig. S12 for different frequency bands. Black traces are tf-PWSs using 10% of the available PCC autocorrelations and are shown to visualize amplitude variability. The frequency bands of the top three and lower-most panel are 1.5-3.0 Hz, 2.4-4.8 Hz, 3.6-7.2 Hz, and 1.2-8.9 Hz. The fourth panel contains the three total data tf-PWS stacks from the top three panels. The blue line in the lower-most panel shows the linear stack of all PCCs for comparison. The 6.14 s signal becomes visible only at the higher frequencies while the 10.46 s signal is coherent for the lower frequencies. The polarities are negative as expected for an impedance increase *(56)*. Linear and tf-PWS stacks both consistently show both signals.

### S2.3 Method C (Doyeon Kim, Vedran Lekic, Nicholas Schmerr)

Similar to SEIS data from Mars where we only have seismic measurements from a single station, such single station driven constraints produced from both RF and autocorrelation function on Earth have shown to be consistent (*20*). To verify our RFs and their structural signals from the Martian subsurface, we use continuous seismic recordings of ambient noise (e.g., Fig.

S13) as well as high-frequency (HF) events on Mars (e.g., Fig. S14A-B) and compute autocorrelation functions (ACFs) to approximate the impulse response at InSight's seismometer. First, we take 6 months (between April and September, 2019) of deglitched continuous data (*38*) recorded by the very broadband (VBB) sensor. The instrument response is removed from the data to obtain velocity recordings and the three SEIS-VBB components are rotated to the ZNE coordinate frame. An example of the amplitude measurements from ambient noise waveforms is shown in Fig. S13. The ambient noise recording on Mars shows a clear contrast between the time-frequency character of daytime and nighttime signals (Fig. S13; *18*). This first order difference reflects the bimodal noise regime on Mars, with the current interpretation being that it is associated with the atmospheric boundary layer activity related to the transition from nighttime laminar flow to daytime turbulent flow (*18*). Data is segmented by a 30-min window and further separated into two groups using a Gaussian mixture model. The two groups represent signals from high vs. low amplitude noise regimes (e.g., day vs. night portions of the data).

Data from the two groups (Fig. S13D) are processed in the following manner. We apply a bandpass filter to the waveforms between 0.05-3.5 Hz. To suppress nonstationary noise, we normalize the data using a weighting function (*48*) that computes running absolute median amplitudes with a 300 s sliding window. We further apply spectral whitening (with a whitening width of 0.1 Hz) prior to autocorrelation in order to obtain stable autocorrelation functions in the lower frequencies. The power spectral density (PSD) of the noise records shows a relatively larger spectral amplitude below 1 Hz so an adaptive weighting function was used to address this bias toward lower frequencies in the records (*66*). The autocorrelation is computed in the spectral domain for each 30-min data segment using a 70% overlap between successive segments. Phase-weighted stacking is then performed on the autocorrelations, after which they are bandpass filtered between 1.5–3 Hz (e.g., Fig. S14C). To minimize the effect of 1 Hz instrument tick artifact and its overtones (e.g., Fig. S13C and S13E), a notching comb filter is applied to the processing flow. Source effects in the ACFs are suppressed by applying a cosine taper at lag-times <1.8 s. ACFs for the high-noise (daytime) and low-noise (nighttime) regimes are shown in Fig. S14C, in blue and red, respectively.

In addition to ambient noise, we perform autocorrelations on P- coda signals from 48 HF events (Fig. S14B lists HF events used). For each event, we used a standard algorithm of STA/LTA triggering on the corresponding Hilbert envelope averaged across components (Fig. S14A) to pick the P- and S-arrivals. Then, the P-arrival times are refined using an implementation of MCCC *(67)*, and used to precisely align the vertical component waveforms (Fig. S14B). Only the P-coda portion of the vertical component waveforms (Fig. S14A-B yellow vertical lines) is used for computing P-coda ACFs, and we maintain most of the steps from the ambient noise processing described above. These include minimization of the 1 Hz tick artifact, spectral whitening, post-filtering 1.5–3 Hz, and cosine tapering. The P-coda signal start time, relative to each P arrival, is taken to be the average across events of the times when the component-average envelope reaches its maximum value, prior to the arrival of the S wave. The P-coda signals used in the ACF construction have a duration of 148.7s, which corresponds to the shortest P-coda length amongst the HF events (e.g., Fig. S14A). Comparison with predicted arrival times from representative models produced by the RFs (e.g., Fig. 2) shows that many of these arrivals can be explained by P-wave reflections from interfaces within the crust ($P_1P$, $P_2P$, $P_3P$ and $P_2P_2$ in Fig. 3).

S3. RF inversion

S3.1 Method A (Felix Bissig, Amir Khan, Domenico Giardini)

Inversion method A follows Bissig et al. *(68)* in parametrizing the crust, modeling of RFs, and inversion strategy. A visualization of the model parametrization is given in Fig. S15. We invert for the seismic structure, i.e., density, S-wave, and P-wave velocity, from the surface to 100 km depth. Within the crust, we adopt a staircase-like structure, where the depth and magnitude of discrete S-wave velocity jumps across crustal discontinuities are free parameters in the inversion. At greater depth, we employ linear gradients in velocity from the Moho to 100 km depth and from there to 400 km, respectively. To allow for variations in mantle structure, the S-wave velocity at 100 km is a free parameter. Elastic properties are fixed to the seismic reference model TAYAK (*69*) below 400 km. We assume constant ratios of density- and P-to-S-wave velocity, i.e., $\rho$/Vs and Vp/Vs, respectively, from the surface to 100 km depth and invert for them. The quantity of model parameters depends on the number of crustal layers used (Tab. S3). Here we explore 2-, 3-, 4-, 6-, and 8-layer models.

For a given 1-D seismic model and event, we compute waveform synthetics via the reflectivity method (*70*). We vary epicentral distance for each of the three events separately, but use only one source depth value for all events in order to reduce computational costs by a factor of three. These four location parameters are treated as unknowns in order to achieve a greater variation in P-wave incidence angle. The moment tensor is set to that of an explosion and back-azimuth estimates are provided by Giardini et al. (*21*). Anelasticity is included through shear- and bulk-attenuation quality factors, which are held constant to their respective values in model TAYAK. Processing of synthetic and real waveforms are equivalent (cf. section S1.3), except that 1) the orientation of the LQ-axes is equal to that of real data, and 2) arrival times of P- and S-waves are computed via ray tracing (*71*).

The probabilistic solution to the inverse problem, $\boldsymbol{d}$ = g($\boldsymbol{m}$), where $\boldsymbol{d}$ are the observed data, $\boldsymbol{m}$ the model parameter vector, and g the forward operator mapping from model to data space, is expressed by (e.g., *72,73*):

$$\sigma(\boldsymbol{m}) \propto h(\boldsymbol{m})\mathcal{L}(\boldsymbol{d},\boldsymbol{m})$$

where $h(\boldsymbol{m})$ is the prior probability distribution of model parameters (cf. Tab. S3), $\mathcal{L}(\boldsymbol{d},\boldsymbol{m})$ is the likelihood-function quantifying the misfit between synthetic and observed data, and $\sigma(\boldsymbol{m})$ is the posterior distribution. We consider low- and high-frequency Ps RFs (processing method C) of events S0235b, S0173a, and S0183a in the inversion and discriminate between distinct time windows, *i*, in computing the likelihood-function for a given event, *e*:

$$\mathcal{L}_{e,i}(\boldsymbol{d}_e,\boldsymbol{m}) = exp(-\Phi_{e,i}(\boldsymbol{d}_e,\boldsymbol{m}))$$

where $\Phi_{e,i}(\boldsymbol{d}_e,\boldsymbol{m})$ is the L2-norm misfit between synthetic, $\boldsymbol{d}_e^{syn}$, and observed RF amplitudes, $\boldsymbol{d}_e^{obs}$, scaled by an uncertainty estimate, $\sigma_e$, and weighting factor, $\chi_e$, for that particular event and window:

$$\Phi_{e,i}(\boldsymbol{d}_e,\boldsymbol{m}) = \chi_e\left(\frac{1}{2N\sigma_e^2}\sum_{j}^{N} || \boldsymbol{d}_{e,j}^{obs} - \boldsymbol{d}_{e,j}^{syn} ||^2\right)$$

We use four windows in total per event, one for the P-wave at time zero and three for the positive arrivals within the first 10 seconds. The windows are defined separately for each event and are shown in Fig. S16 and S17. Uncertainty is set to 50% of the mean absolute Ps RF amplitude within 0–10 sec. We opted for this rather conservative value to allow for an extended exploration of the model space. The weighting factor $\chi_e$ is set to 2/3 for S0235b and to 1/6 for S0173a and S0183a, respectively, reflecting the higher confidence in the Ps RF from event

S0235b. The conjunction of the likelihood-functions for each event and window results in the total likelihood-function:

$$\mathcal{L}(d,m) = \prod_{e,i} \mathcal{L}_{e,i}(\boldsymbol{d}_e, \boldsymbol{m})$$

We sample the posterior distribution by means of the cascaded Metropolis-Hastings algorithm (*74*). At iteration $n$, a model, $\boldsymbol{m}^n$, is proposed and retained only if the following criterion is true for each event and window:

$$\frac{\mathcal{L}_{e,i}(\boldsymbol{d}_e, \boldsymbol{m}^n)}{\mathcal{L}_{e,i}(\boldsymbol{d}_e, \boldsymbol{m}^{n-1})} > \alpha$$

with $\alpha$ being a random number between 0 and 1.

We invert Ps RFs for S0235b, S0173a, and S0183a jointly in ten separate inversions that differ in the number of crustal layers and corner-frequencies of RFs. For each inversion, we ran 32 chains in parallel, each starting at a different initial model and subsequently sampling ~12,000 – 25,000 models of which every 10th was retained for further analysis. Overall, this results in ~40,000-80,000 collected models per inversion.

Inversion results are presented in blue color in Figs S18 and S19. All parametrizations are capable of fitting the timing of Ps RFs for events S0235b and S0173a, while a slight phase-shift is apparent in S0183a. Amplitudes are more difficult to model, in particular because observed Ps RFs of the different events disagree on the relative amplitudes of peaks and hence velocity-contrasts across discontinuities. However, we emphasize the large uncertainties associated with amplitudes, as evident for S0173a where differently deglitched data sets result in distinct amplitudes (Fig. S6). Parametrizations with more layers tend to produce gradient-like discontinuities that result in overall diminished RF amplitudes. From the model ensembles (Fig. S18A and S19A) and the discontinuity depth distributions (Fig S18B-G and S19B-G), we observe three discontinuities at depths 8±2 km, 20±5 km, and 39±8 km.

S3.2 Method B (Rakshit Joshi, Brigitte Knapmeyer-Endrun)

Here we have employed a modified version of the Neighbourhood Algorithm (NA) (*75,76*) for the simultaneous inversion of the three receiver functions computed from events S0173a, S0183a and S0235b *(77)*. The forward calculation of receiver functions is based on the code of Shibutani et al. *(78)* that uses a simple reflectivity matrix approach to provide the P-to-S response of a layer stack. The resulting synthetic vertical and radial RFs are convolved with the measured vertical RF to consider source complexity. An additional step of coordinate rotation and re-scaling is performed to transform the RF components into the ray coordinate system. Tests with synthetic seismograms for Mars models have shown that this allows obtaining results comparable to full Instaseis synthetics based on an AxiSEM data base *(79)* with a greatly reduced computation time *(80)*. Density was not used as an independent parameter during the inversion, but calculated from P-wave velocity values using Birch's law *(81)*. In addition to the layer thickness and the S-wave velocity within the layer and the half-space, the $V_p/V_s$ ratios of all the layers and half-space were also included as model parameters (Tab. S4). The two parameters that control the NA need to be tuned depending on the problem and the style of sampling needed. For an explorative search that is robust against local minima, we perform 2000 iterations in each inversion run with 200 models produced at each iteration and 200 cells re-sampled at each iteration, resulting in an ensemble of 400,000 models per run. Furthermore, each inversion was repeated several times with a different starting random seed value to test the stability of the results.

We invert the RF waveforms generated by processing methods C (Section S1.3), considering both low- and high-frequency P-to-S RFs. For each of these data sets, we tested the data against models with increasing degree of complexity. Starting with 2 layers with constant velocities over a half space, we subsequently increased the complexity to include cases with 3, 4, 6 and 8 layers. The L2 norm misfit was then used to compare observations to synthetic RFs using the same misfit function as described in Section S3.1. The uncertainty level along with the weighting factor and the time windows for misfit calculation for each event were also left unchanged in order to minimize any processing differences between the two inversion methods. From the resulting ensemble, we first retained every $5^{th}$ model which down-sampled our ensemble to 80000 models. In order to reduce the bias in NA sampling, we then compared the distance of each model to the best fitting model within this subset using multi-dimensional mapping, and binned these models into 50 bins according to this distance. Finally, we selected 100 models from each bin, giving us a total of 5000 models. The results of the inversion are shown in yellow color in Figs S18 and S19, indicating that the data can be explained either by two discontinuities at depths 8±2 km and 20±5 km, or with an additional discontinuity at 39±8 km.

S4. Comparison with waveform modeling for source inversion (Nienke Brinkman, Simon Stähler, Domenico Giardini)

The first effort on fitting waveforms of observed marsquakes was done by Brinkman et al *(81*) in the context of seismic source inversion. This study was performed to find optimal source mechanisms of three high-SNR marsquakes (S0173a, S0183a, S0235a), and tested different crustal models. Considering P- and S-wave phases, the proposed two-layer model of this study provided well-matching waveform fits, specifically for the coda of the P-waves on the radial component and S-wave precursors, interpreted here as a S-to-P conversion at an interface in 24 km depth. Crustal models where the Moho was located deeper did generally not result in stable source results. For S0235b, we illustrate this agreement in Fig. S20 by showing waveform fits for two different crustal models.

S5. Global crustal thickness from gravity, topography, and seismic constraints (Mark Wieczorek, Adrien Broquet)

Our global crustal thickness modeling employs standard methods that have been applied previously to the terrestrial planets and Moon using spacecraft data *(83)*. In particular, the observed gravity field is assumed to be the result of surface relief, relief along the crust-mantle interface, and hydrostatic density interfaces in the mantle and core. The crust has a constant density in our models, with the sole exception of the low-density polar ice cap deposits. We make use of 13 *a priori* density profiles of the mantle and core *(25)* that span the range of plausible pre-landing Martian compositional models and core radii. In addition to these reference models, we also include two additional reference density profiles based on the Martian bulk composition model of Yoshizaki and McDonough *(84)*.

For each reference interior model, the global crustal thickness model was computed as follows. First, the gravitational attraction of the surface was computed using finite-amplitude techniques *(85)*. Second, the gravitational attraction of the low-density polar caps was accounted for using densities of 1250 and 1300 kg $m^{-3}$ for the north and south polar caps, respectively, along with the polar cap thickness model of Broquet et al. *(86)*. Third, the gravitational attraction of hydrostatic relief in the mantle and core beneath the lithosphere was computed using the method described in Wieczorek et al. *(25)*. Fourth, for an assumed average crustal thickness, and

using the uppermost mantle density of the reference interior model, we inverted for the relief along the crust-mantle interface that satisfies the observed gravity field. Finally, the average crustal thickness was adjusted iteratively in order to obtain the desired value at the InSight landing site.

We made use of the MarsTopo2600 spherical harmonic shape model of Mars *(87)* and the GMM-3 gravity field model *(88)*. Spherical harmonic degrees were considered up to degree 90, and a downward continuation filter was employed that has a value of 0.5 at degree 50. For each reference interior model, we tested all bulk crustal densities that were greater or equal to 2550 kg $m^{-3}$, which is a reasonable lower bound taken from Goossens et al. *(10)*. It was found that as the crustal density increases, the minimum crustal thickness of the model decreases. The maximum permissible crustal density is thus obtained when the minimum crustal thickness reaches zero, which always occurred within the Isidis impact basin. Tests showed that the inclusion of a constant thickness layer at the surface with reduced densities (from meters to kilometers thick) had only an extremely minor impact on the results presented here. Further tests that made use of lower crustal densities in the southern highlands than in the northern lowlands *(26)* showed that the maximum permissible crustal densities were unchanged with respect to our constant density model. Fig. S21 shows a representative global crustal thickness model for one set of model parameters: Other models are, to first order, simply scaled versions of this model.

The two parameters that have the largest impact on the global crustal thickness model are the difference in density between the upper mantle and crust, and the seismic thickness of the crust at the InSight landing site. The average thickness of the crust for each model is plotted as a function of the crust-mantle density contrast in Fig. S22 for various assumed crustal thicknesses at the InSight landing site (text annotation) and reference interior models (legend). For a given InSight crustal thickness, the average thickness of the crust is seen to decrease with increasing density contrast, and this dependence is only weakly sensitive to the specific reference interior model that was used. Nevertheless, the reference interior model fixes the density of the upper mantle (which ranges from 3352 to 3492 kg $m^{-3}$), and this affects the permissible values of the crustal density and crust-mantle density contrast. The minimum density contrast for each curve corresponds to the maximum crustal density, and also corresponds to that model where the minimum crustal thickness is zero.

The average crustal thickness is plotted in Fig. S23 as a function of crustal density, for assumed thicknesses at the InSight landing site of either 20 or 39 km, central values for the two-layer and three-layer seismic models, respectively. For the 20-km thick case, the range of allowable crustal densities is small (2550-2700 kg $m^{-3}$), and the average crustal thickness is well constrained to 28-31 km. In contrast, for the 39-km thick case, the range of allowable crustal densities is larger (2550-3050 kg m-3), and the average crustal thickness varies from 47 to 59 km. When the uncertainties associated with the InSight seismic thicknesses are considered, the two-layer model predicts an average crustal thickness between 24 and 38 km with a maximum permissible crustal density of 2850 kg $m^{-3}$. For the three-layer seismic model, the average crustal thickness is predicted to lie between 39 and 72 km with a maximum permissible crustal density of 3100 kg $m^{-3}$.

## S6. Implications for the heat-producing element budget and the thermo-chemical history of Mars (Chloé Michaut, Ana-Catalina Plesa, Henri Samuel, Scott McLennan)

The crustal thickness inferred from RFs and gravity data allows placing constraints on the composition of the crust and of the mantle both in terms of major and trace elements. Due to

enriched HPE, crustal thickness is a key parameter in predicting present-day heat flux. The present-day crustal thickness is an essential anchor point for thermo-chemical evolution models that predict past mantle rheology and cooling rates.

S6.1 Constraints from 1D parameterized models considering bulk crust formation by melt extraction over time

To exploit the relationship between the present-day crustal thickness and the planet's history, we conducted an extensive exploration of the possible thermo-chemical histories of Mars using parameterized convection calculations to model the evolution of a Mars-like planet for 4.5 Gyr. This approach models the heat transfer and the chemical element partitioning within the main planetary envelopes: an adiabatic convecting iron alloy core overlaid by a silicate mantle convecting underneath an evolving, stagnant lithospheric lid. The latter includes a crust enriched in radioactive heat producing elements (HPE). Both the crustal and lithospheric thicknesses evolve as a result of the thermal history of the planet. The crust is assumed to progressively form via magmatic processes triggered by shallow mantle melting. Details of the model can be found in Samuel et al. (*27*) and references therein. The only difference is that we now use melting curves that are more appropriate for a Martian-like composition (*89*) instead of the solidus and liquidus derived for a peridotitic mantle (*90*) that are more appropriate for an Earth-like composition. We note that the solidus of Ruedas and Breuer (*89*) is similar to the solidus of Duncan et al. (*91*), and nearly identical for the relevant pressure, at which partial melting takes place (i.e., up to 8 GPa). While this parameterized modelling approach is computationally efficient, it accurately reproduces 1D structures obtained in curved geometries (*27,28,92,93*). We explored a wide range of Martian evolutions by randomly sampling the values for the main governing parameters within plausible bounds. The sampling space is composed of mantle rheological parameters (effective activation energy $E^*$ and activation volume $V^*$, reference viscosity $\eta_0$), initial thermal state (core-mantle boundary temperature $Tc_0$ and temperature at the top of the convecting mantle $Tm_0$), and the crustal enrichment factor, $\Lambda$ (*i.e.,* the ratio of HPE content in the enriched crust to that of the primitive mantle). We fixed the bulk HPE content corresponding to the values suggested in Wänke and Dreibus (*29*) (i.e., U=16 ppm, Th=56 ppb, K=305 ppm). The explored bounds of the governing parameters are listed in Table S5. The values of other model parameters can be found in Tab. 1 in the supplementary material of Samuel et al. (*27*).

Fig. S24 displays the sampled input range of governing parameters and several resulting distributions that lead to a present-day average crustal thickness in the range 39-72 km, as proposed by the three-layer crust inferred by RF analysis and gravity-topography considerations. The latter correspond either to present-day model output (e.g., surface heat flow) or input governing parameters. The crustal thickness requirement considered here does not strongly constrain mantle activation energy or volume (Fig. S24a,b), but favours 1-$\sigma$ range mantle reference viscosity around $10^{21\pm0.5}$ Pa s (Fig. S24c), which is in line with pre-mission estimates (*6,27*). The initial mantle temperature is also not strongly constrained, but relatively cold values (1770±50 K) are favoured in a statistical sense (Fig. S24d). The lack of strong constraints on the mantle rheology and its initial thermal state essentially stems from the trade-offs between temperature and viscosity, which require additional independent constraints such as orbital data (*27*) and/or tighter ranges of inferred crustal thickness to resolve. The predicted present-day surface heat flux ranges between 20 and 25 mW/m$^2$ (Fig. S24e), which is consistent with pre-mission estimates (*6,27,69,94*) and corresponds roughly to the sampled (i.e., *prior*) range. The

latter is considerably influenced by the assumed bulk HPE content (*92,942*). The most strongly constrained quantity is the crustal enrichment with a corresponding range of 5-24 and a 1-$\sigma$ range $\Lambda$=15.5±3.5 (Fig. S24f). This range is consistent with recent estimates that rely on elastic thickness constraints (*28*) and with a crustal HPE content inferred at the surface by GRS data corresponding to a crustal enrichment of 8.7 to 10.6 for crustal densities between 2550 and 3100 kg $m^{-3}$. We note that these crustal enrichment factors have been calculated based on the Wänke and Dreibus (*29*) bulk abundance of heat producing elements. The compositional model of Taylor (*30*) has a similar bulk abundance of radioelements, and, hence, will lead to similar enrichment factors. Other compositional models such as Yoshizaki and McDonough (*84*) with a higher bulk abundance of radioelements would require in a higher crustal enrichment to match the same geodynamical and geological constraints.

Performing the same exercise for the two-layer, thinner crust end-member (24-38 km) yields more constrained matching histories corresponding to a smaller solution subset (Fig. S25). A thinner crust requires an even colder mantle, triggering smaller amounts of partial melt at shallow depth. This colder mantle state calls for a higher HPE content in the crust (at the expense of that of the underlying mantle), and/or an initially colder mantle. These two effects can be observed in Fig. S25d and Fig. S25f, respectively. The initial mantle temperature is therefore more strongly constrained than in the thick crustal end-member case to 1750±40 K for the 1-$\sigma$ range, (see Fig. S25d). The crustal enrichment relative to the primitive mantle is constrained to values distinctly larger than 16 (24.9±3 for the 1-$\sigma$ range, see Fig. S25f). The reference viscosity remains constrained to $10^{21.3\pm0.5}$ Pa s (Fig. S25c) as in the thick three-layer crustal end-member. The temperature and pressure dependence of viscosity are constrained to relatively smaller values than in the thick crustal end-member. However, due to the persisting trade-off between temperature and viscosity such constraints remain relatively weak (with the corresponding 1-$\sigma$ ranges: $V^*$=3.3±2 $cm^3$/mol, and $E^*$= 260±114 kJ/mol, see Fig. S25a and Fig. S25b). Finally, due to the same bulk HPE content considered for the two-layer and the three-layer cases, the corresponding present-day surface heat flux compatible with the thin end-member case is 20-24 $mW/m^2$ (Fig. S25e), which is very similar to the range inferred for the thick crustal end-member (Fig. S24e).

### S6.2 Constraints from 3D convection models and 1D parameterized models accounting for regional variations in crust thickness and looking for present-day mantle melting

The surface of Mars is on average very old (>3 to 3.5 Gyr), showing that volcanism and resurfacing by lava flows was mostly active early in the Martian history, and then became much sparser. Although recent lava flows have been observed, visible only in the Tharsis province (*95, 96*), thermal evolution models producing widespread melting in the Martian mantle at the present-day are unlikely. For a given crustal HPE concentration, the occurrence of mantle melting is dependent on the crustal structure since the thicker the crust, the higher the amount of heat sources at that location and the larger the temperature at depth. To exploit this relationship, we also conducted an extensive exploration of the possible thermal history of Mars using parameterized convection models accounting for two different hemispheres with different crustal properties (*28*) as well as 3D convection simulations accounting for lateral variations in crustal thicknesses (*6*). In contrast to the previous set of numerical experiments (Section S6.1), the crustal structure is set at the start of the simulations (t=0) to account for an alternative crustal formation that would result from the differentiation of a magma ocean. The model is let to evolve for 4.5 Gyr in both the parametrized models and 3D simulations, where we used the

Wänke and Dreibus (*29*) model for radioelement concentration for the bulk silicate Mars. We also note that the bulk of the Martian crust has been built during the first 500 to 700 Myr (*96*), therefore the present-day thermal state is not sensitive to the exact mechanism of crustal growth but rather to the final crustal thickness.

We used the model of Thiriet et al. (*28*) to account for the two hemispheres and consider a uniform crustal density, thermal conductivity and enrichment factor, but two different average crustal thicknesses for the North and the South, which respectively cover 40% and 60% of the planet's surface. One difference with the model of Thiriet et al. (*28*) is that here we parameterized the average crustal thickness in the South, $D_S$, based on that in the North, $D_N$, using $D_S = D_N + h(1+\rho_c/(\rho_m-\rho_c))$, where $\rho_m=3500$ kg m$^{-3}$ is the mantle density, $\rho_c$ the crustal density, and $h$=3.3 km (instead of 6 km), a value that is in good agreement with inversions of gravity and topography data presented in this manuscript (Section S5). Another difference is that we estimated *a posteriori* the lithosphere thickness below the Tharsis province accounting for a thicker crust, which we also parameterized from the results of gravity and topography data inversions using $D_T = D_N + h_T(1+\rho_c/(\rho_m-\rho_c))$, where $h_T$=4.45 km and $D_T$ is the average crustal thickness below the Tharsis province. The temperature at the radius at the base of the crust below the Tharsis province, $T_C(R_{MT})$, is then calculated assuming a steady-state temperature profile in the crust below Tharsis from the Moho heat flux, $Q_{Moho}$, which we estimate from the heat flux at a radius $r=R_{MT}$ in the southern hemisphere: $T_C(R_{MT})=A_C(R_P^2-R_{MT}^2)/6k+R_{MT}^2(A_CR_{MT}/3-Q_{Moho})(1/R_P-1/R_{MT})/k+T_S$, where $T_S$ is the surface temperature, $k=3$ W m$^{-1}$ K$^{-1}$ is the crust thermal conductivity and $A_C$ the present-day crustal heat production. Transient effects due to the decay of heat producing elements that are neglected in this calculation would increase the temperature at the Moho below Tharsis. Although they are not negligible in a lithosphere that is several hundreds of kilometres thick (*97*), they are much more limited in a crust of several tens of kilometres thickness. The lithosphere thickness, $H_L^T$, below the Tharsis province is then found by interpolating the temperature profile starting from the temperature at Moho depth considering a constant heat flux equal to the Moho heat flux in the lithospheric mantle and up to the temperature characterizing the base of the lithosphere, $T_L$.

For each model, we checked whether melting would occur at the present-day:

- within a plume ascending from the core-mantle boundary and up to the base of the lithosphere below Tharsis, by comparing the temperature of the plume (*28*) to the solidus temperature at the pressure of the base of the lithosphere below Tharsis (contrary to Thiriet et al. *(28)* we do not consider that the plume penetrates through the lithosphere),
- within local, smaller-scale, upwellings below the South, as well as below the North, by comparing the solidus temperature at the pressure of the lithospheric base in the South, respectively North, to the mantle temperature.

We assume that the melt reaches the surface and is responsible for the recent volcanic activity in Tharsis.

We used the parameterization of the solidus temperature $T^T_{solidus}$ by Ruedas and Breuer (*89*) applying a correction for crustal extraction from the primitive mantle: $T_{solidus}=T^T_{solidus}+d_{crust}\Delta T_{sol}/D_{ref}$, where $\Delta T_{sol}$=150K, $d_{crust}$ is the average crust thickness and $D_{ref}$ =190 km.

The results of the parameterized model described above are in good agreement with fully dynamical 3D simulations (Figs. S26, S27), where the locations at which partial melt is produced in the mantle have been estimated by comparing the local temperature to the solidus (*6*). In both

1D and 3D models, melting occurs only below Tharsis if the percentage of the bulk radioelement content in the crust is about 55% or higher (Figs. S26 and S27). This is the case if the average GRS-derived concentration in HPE is used for the bulk crust in the 3-layer (thick crust) model ($\overline{\Lambda}$=12.2±2.0). On the contrary, for the 2-layer (thin crust) model, a GRS-derived concentration in HPE for the bulk crust amounts to about 30% of bulk radioelement content in the crust and would lead to widespread melting as shown in both Fig. S26 and Fig. S27. While melts may not reach the surface and remain intrusive today, such widespread melting areas would be difficult to reconcile with the geological history of Mars since evidence of recent eruptions is only present in localized areas. As shown in Fig. S26, successful models that consider a thin crust can be found if the crustal enrichment of radioelements is increased ($\overline{\Lambda}$=19.6±2.4). Given the range of surface concentration in HPE derived from GRS measurements, this would imply, however, that the lower crust contains significant amounts of HPE, and, hence, was formed by a different mechanism than the basaltic surface layer.

S6.3 Combining all constraints together

Overall, the consistent results obtained independently by the complementary approaches described above indicate that the thin crustal end-member requires a large concentration of radioelements in the crust ($\Lambda$>15 and a consistent most probable value of 22), larger than GRS estimates (7.8-9.5 and 8.7-10.6; Table S6) *(31,98,117)*, which would point towards the presence of a buried enriched component. Such a large concentration of radioelements in the crust may imply an upward segregation of heat producing and incompatible elements during the solidification of an initial magma ocean as is observed on the Moon, or secondary differentiation events for the crustal, as for the continental crust on Earth. On the other hand, the thicker three-layer model appears to be consistent with a crustal enrichment compatible with estimates from GRS, as well as progressive crust formation triggered by shallow melting. The commonly accepted estimates from Wänke and Dreibus (*29*) and Taylor (*30*), favor the thicker crustal end-member. In addition, considerations on crustal production via magma extraction (Section S6.1) favor a crustal enrichment factor $\Lambda$=5-22 and a 1-$\sigma$ range of 16.2±4.2 (Fig. S24f), while constraints on the occurrence of present-day melting underneath Tharsis only (Section S6.2) suggest a crustal enrichment factor of $\Lambda$=9-18 with 1-$\sigma$ range of 12.2±2.0, leading to a consistent overlapping interval of $\Lambda$=9-18 and a consistent most probable (1-$\sigma$) overlapping range $\Lambda$=12.0-14.2 for the crustal enrichment of Mars.

In both thin or thick end-member cases, the reasonable assumption of a bulk HPE content from commonly accepted estimates by Wänke and Dreibus (*29*) and Taylor (*30*) implies a present-day surface heat flux range of 20-25 mW/m$^2$ (Figs. S24e and S25e), which is consistent with the average values of 22.5-23.6 mW/m$^2$ associated with the 3D models (Figs. S26 and S27).

S7. Do GRS HPE Abundances Reflect the Uppermost Igneous Martian Crust?

The Mars Odyssey GRS instrument interrogates the upper few decimeters of the Martian surface and the analytical signal is dominated by what is generally considered to be well-mixed regolith and in places, also by dust *(98,99)*. Use of GRS HPE data (K and Th measured abundances and U based on an assumed Th/U ratio of about 3.8) as a crustal composition model (Table S6) assumes the HPE abundances reflect the uppermost igneous crust and are not significantly affected by upward or downward secondary mobility on a scale significantly greater than the GRS interrogation depths. There have been suggestions that GRS data are influenced by secondary aqueous processes, resulting in enrichments in the surficial regolith relative to

protolith igneous materials *(e.g. 99)*, in part to explain differences between compositions (including HPE) in Martian meteorites (SNC) and the GRS data. However, in situ measurements of a wide variety of Martian rocks and regolith by rovers suggest that potassium abundances are significantly enriched, on average, compared to SNC meteorites *(e.g. 13,31,100)*. In addition, analyses of the NWA7034 Martian meteorite breccia (and its multiple pairs) has greatly expanded the range of HPE concentrations observed in Martian crustal rocks, consistent with elevated crustal HPE compared to SNC meteorites *(e.g. 14,101)*. A consequence of these observations is that the SNC meteorites are now widely considered to be non-representative of the overall crust *(e.g. 100)*. Many workers have instead observed spatial correlations of the GRS data that mostly align with factors such as apparent crustal age and crustal terrane type *(102,103,104)* and have further noted the lack of geochemical fractionation between K and Th that might be expected during alteration processes *(104)*, consistent with the compositions being representative of their igneous protoliths. If correct, then the GRS HPE data would be representative at least to the average impact gardening and sedimentary erosion depths that produce the regolith. Accordingly, while the possibility that GRS data reflect secondary alteration processes, leading to significant enrichments in average HPE abundances at the near-surface, cannot be entirely discounted, currently it is not a favored model.

On the other hand, there is a possibility of a slight "dilution" effect in the near-surface HPE concentrations due to hydrogen (likely both free and structural water) enrichments and accumulation of Cl- and S-bearing components measured by GRS *(98,105)*, and perhaps a meteoritic component, within the Martian regolith. Enrichments of H-, S- and Cl-rich materials ultimately result from various outgassing processes that accumulate at the near surface. The overall effect would be to lower the levels of HPE compared to the ultimate igneous protoliths. Taking these "dilution" factors into account is basically the procedure that Taylor and McLennan *(31)* carried out in order to arrive at their estimates of crustal HPE (Table S6).

S8. Implications for magnetization (Catherine Johnson, Anna Mittelholz)

The InSight fluxgate magnetometer, IFG, is the first surface magnetometer on Mars *(106)*. Prior to the InSight landing, satellite vector field measurements, $B_{orbit}$, allowed global modelling of the crustal magnetic field at the surface, $B_{surf}$, by downward continuing models derived from orbital data *(107,108)*. $B_{surf}$ is to proportional to the product of the magnetization and the thickness of the magnetized layer. Previous satellite-based models have typically assumed the layer thickness to be a constant value globally of 40 km *(107,108)*, in the absence of seismically-constrained values for absolute crustal thickness or other constraints on the magnetized layer thickness. From IFG data, the local magnetic field strength at the surface, $B_{surf}$ was found to be an order of magnitude larger than satellite-based models *(106)*. Combined with geological information on the maximum burial depth of the magnetized layer these new observations allowed the minimum magnetization strength required to explain the surface field to be estimated for different maximum depths of the magnetized layer *(106,109)*. In this study, we extend our earlier work *(106)* to also include bounds on the maximum depth of the magnetized layer derived from the seismic data. We use the approach of *(109)*, summarized and applied in *(106)*, to estimate the minimum magnetization that is compatible with the surface magnetic field strength measured at the InSight landing site *(106,109)* and is also constrained by the two estimates for crustal thickness. The two crustal thickness models also have implications for the minimum magnetization that is compatible with the surface magnetic field strength measured at the InSight landing site (*106,109*). Deep magnetization extending to the Moho but confined below the

seismically-determined layer 1, would have an amplitude of 1.8 A/m and 3.3 A/m for the ~20-km and ~37-km crustal thicknesses respectively. This represents a case in which the first layer transition around 10 km is indicative of a change in mineralogy or deposition age leading to no substantial magnetization acquisition in the upper layer. If substantial magnetization is carried in the upper seismically-determined layer (but beneath the thin few-hundred-meter-thick veneer of Amazonian and younger Hesperian flows), compatible with a longer-lived dynamo (*110*), magnetizations are <1 A/m for either crustal thickness model (Fig. S28).

S9. Matching moment of inertia and tidal Love Number (Attilio Rivoldini)

Further constraints on the set of average crust thickness and density pairs inferred in this study can be obtained from the moment of inertia (MOI) and tidal Love number $k_2$ of Mars (i.e. *69*). The moment of inertia provides a direct constraint on the crust of interior structure models as it is highly depending on the mass of the crust and mantle. The Love number $k_2$ of Mars requires a large core (i.e., *111*) and can for this reason further reduce the set of crust models. To assess the effect of the geodesy data (*111,112*) on the crust we use the same mantle composition models employed in this study (section S5) together with two plausible mantle temperature end-members (*113)*.

Following Rivoldini et al. *(114)*, we construct global interior structure models that use the two end-member temperature profiles in the mantle and assume a convecting liquid iron-sulfur core. The thermoelastic properties of the mantle for the studied compositions are computed with PerpleX *(115)* using the thermodynamic database and formulation of Stixrude and Lithgow-Bertelloni *(116)*. The crustal density and thickness of each model are chosen according to the relation depicted in Fig. S23. For each interior structure model, the MOI is then calculated and only models that agree with the measured value *(111,112)* within its uncertainty ($1\sigma$) are retained. A further down-selection of compatible models is achieved by retaining only those that have a core radius large enough to agree with the tidal Love number $k_2$ *(111)*.

We find that geodesy data favours for all composition models but the Yoshizaki and McDonough (*84*) composition a thick crust and hot mantle temperature (Fig. S29). Among the used composition models, the Yoshizaki and McDonough (*84*) model has less iron and for this reason a different mass distribution in the mantle that results in a weaker constraint on the crust density and thickness for the hot mantle temperature but it is in favor of thicker crust if the mantle temperature is colder.

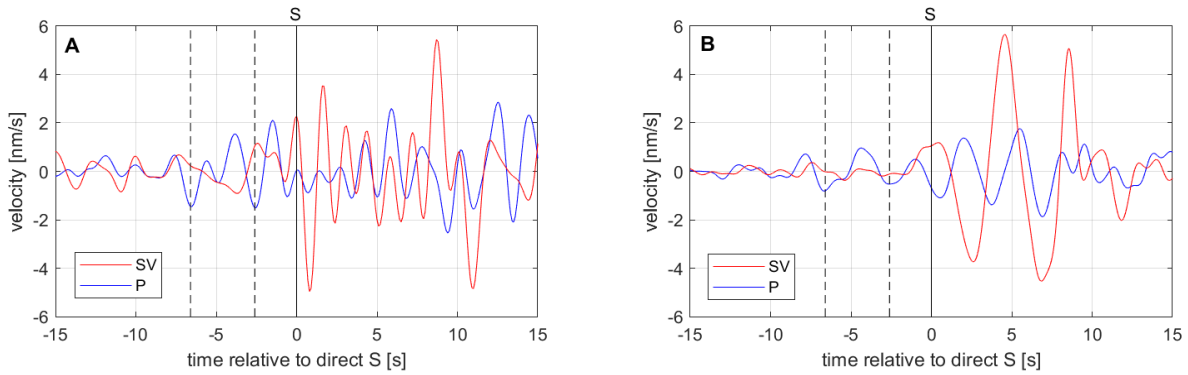


**Fig. S1. S-onsets of events (A) S0173a and (B) S0235b, showing two precursory phases on the P-component.** Data are band-pass filtered between 0.1 and 0.8 Hz and rotated in the P-SV coordinate system. Vertical solid black lines mark the S-onset, vertical dashed black lines the two precursors (with inverted sign, as expected for S-to-P conversions) at about 2.6 s and 6.6 s. Note that the definition of coordinate systems implies a change in sign between the radial component, as shown in Fig. S2, and the SV-component shown here. Phase picks are on the first local maximum rather than on the onsets here as those are easier to identify for the precursors.

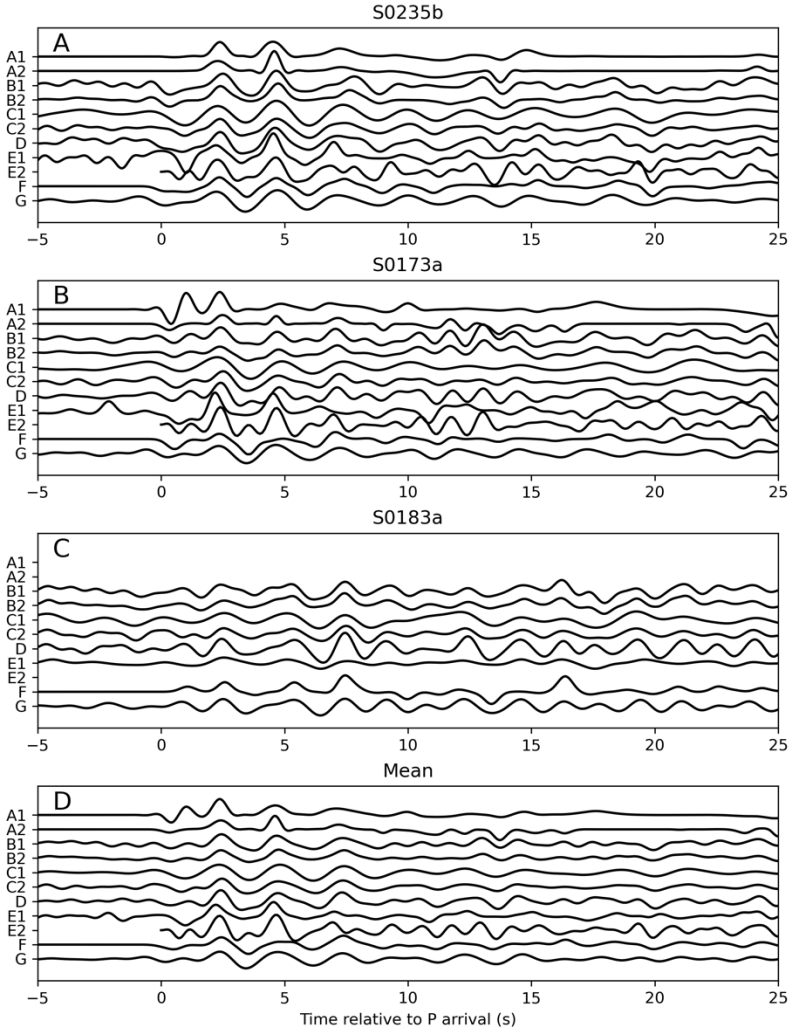


**Fig. S2. All P-to-S receiver functions estimated by different groups plotted with identical amplitude scaling and offset for clarity.** Data are shown separately for events S0235b (A), S0173a (B), S0183a (C) and the mean across all events calculated with the specific method (D). For clarity, data using a slightly higher frequency passband in method A (panels A2 and B2 in Fig. S4) are plotted as A1, while the remaining P-to-S receiver functions are plotted as A2.

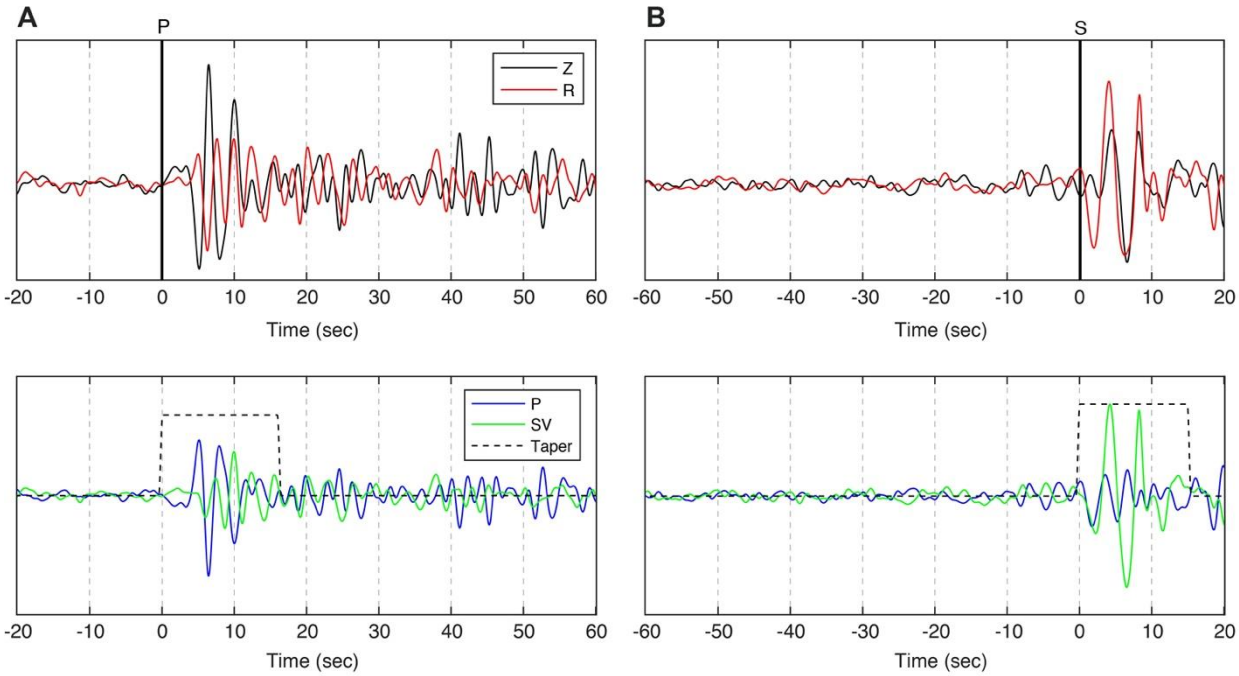


**Fig. S3. Waveforms of event S0235b used in the (A) P-to-S and (B) S-to-P RF analysis**. Waveforms plotted here are bandpass filtered 0.1-0.7 Hz and 0.05-0.7 for (A) and (B), respectively. We estimate the up-going P-SV waves (bottom) from the recorded Z-R waveforms (top) using the free surface transformation by minimizing the correlation between P- and S-energy at the time of the P or S arrival, computed in 8s-long windows starting at the P or S arrival.

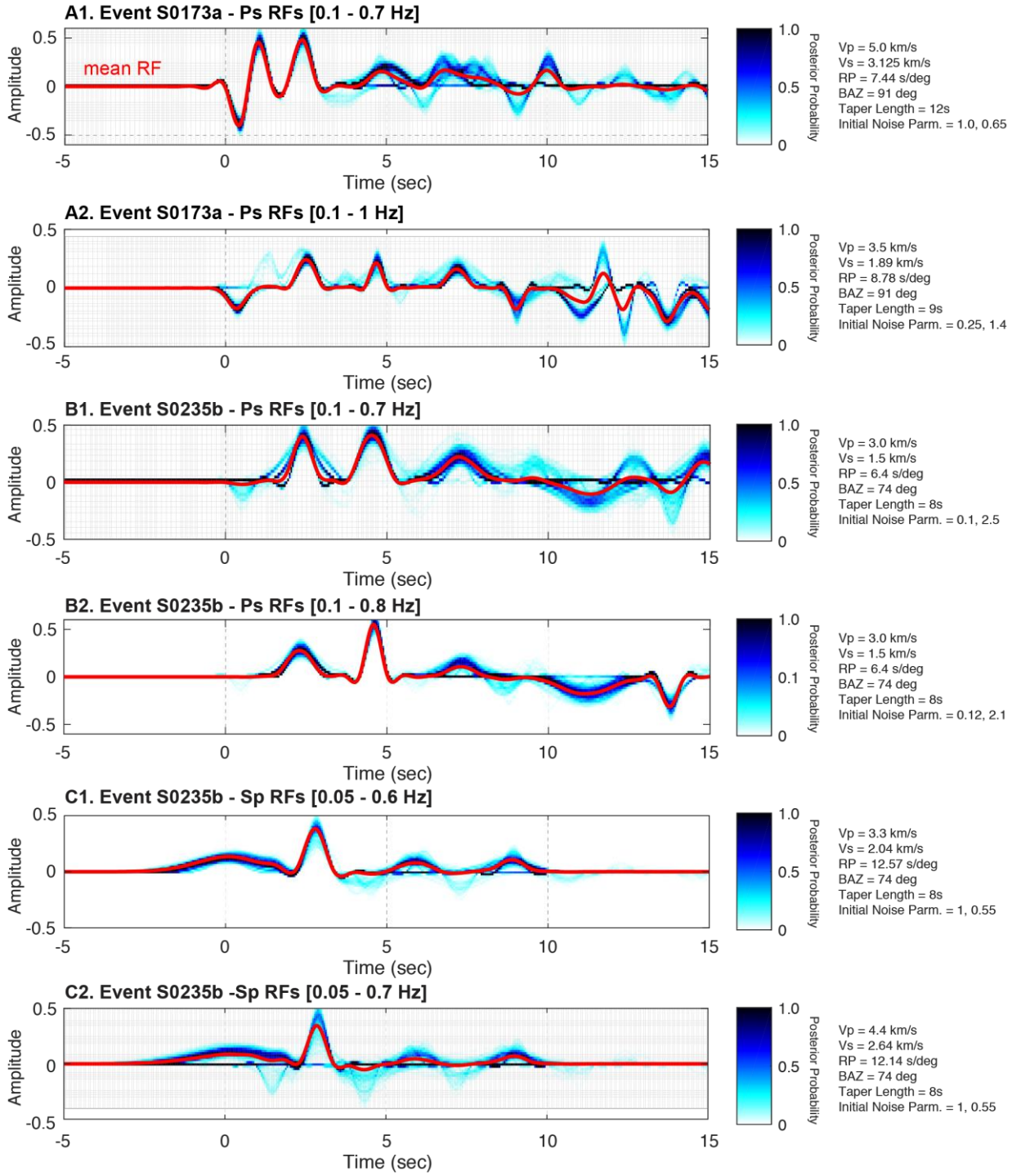


**Fig. S4. Ensemble P-to-S and S-to-P RFs combining all of the models.** For each event, one million iterations of the THBD were performed, discarding the first half as burn-in, and saving every 1000$^{th}$ sample to the ensemble. The average RF for each of the ensembles is shown in red. All of the parameters used to process the RFs (parameters associated with taper length, free surface transformation, and noise parameterization) are shown in the right-hand side of each ensemble solutions. NB: the acronyms for Vp, Vs, RP and BAZ refer to P-wave velocity, S-wave velocity, ray parameter, and back azimuth, respectively.

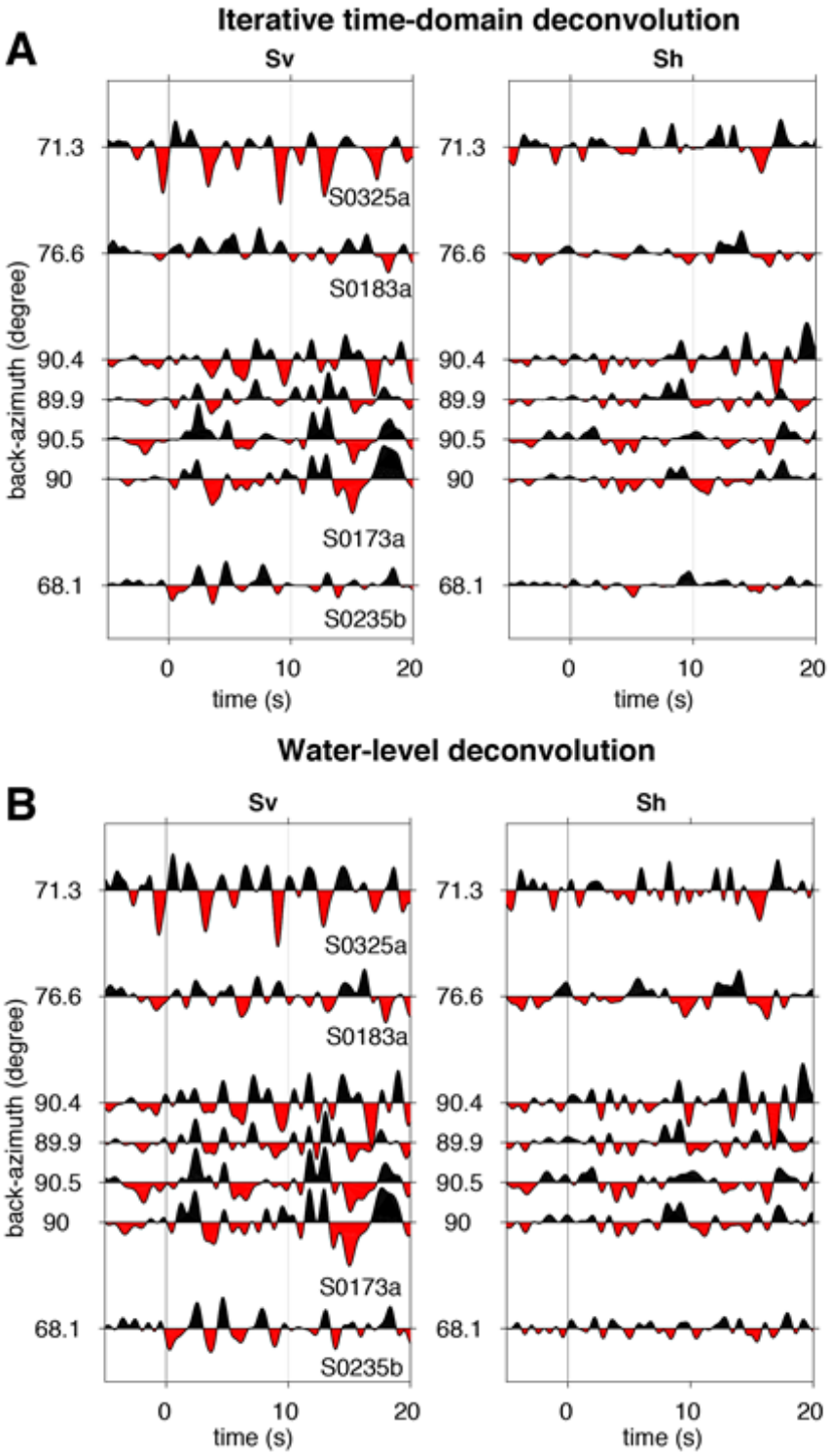


**Fig. S5. RFs obtained from iterative time-domain (A) and water-level (B) deconvolutions as described in Methods B.** Left and right panels show the Sv and Sh components for the four marsquakes, whose names are indicated at the bottom of the Sv traces. Estimated back-azimuths are indicated along the vertical axis. For S0173a, results of four different deglitching algorithms are shown *(38)*.

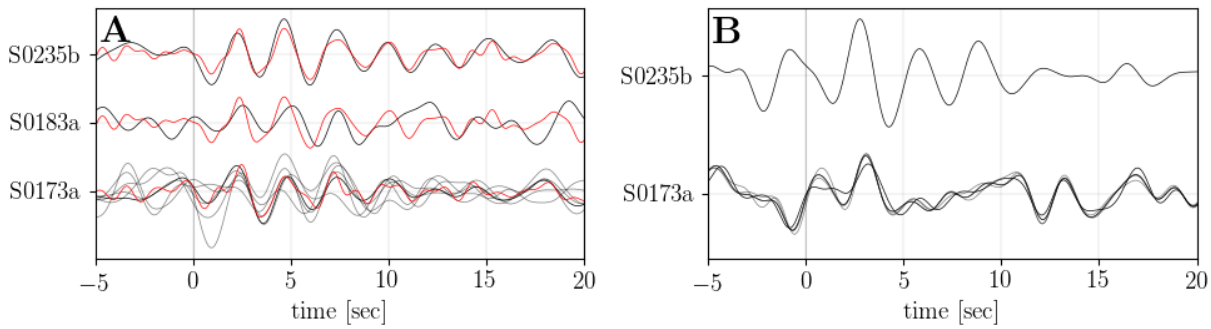


**Fig. S6. P-to-S (A) and S-to-P RFs (B) for events S0173, S0183a, and S0235b using method C.** RFs for event S0173a are based on waveforms deglitched by different groups (grey lines), whereas the RF based on the "final" deglitched data set and used for the inversion is depicted in black. The additional set of P-to-S RFs filtered at higher frequencies are shown in red.

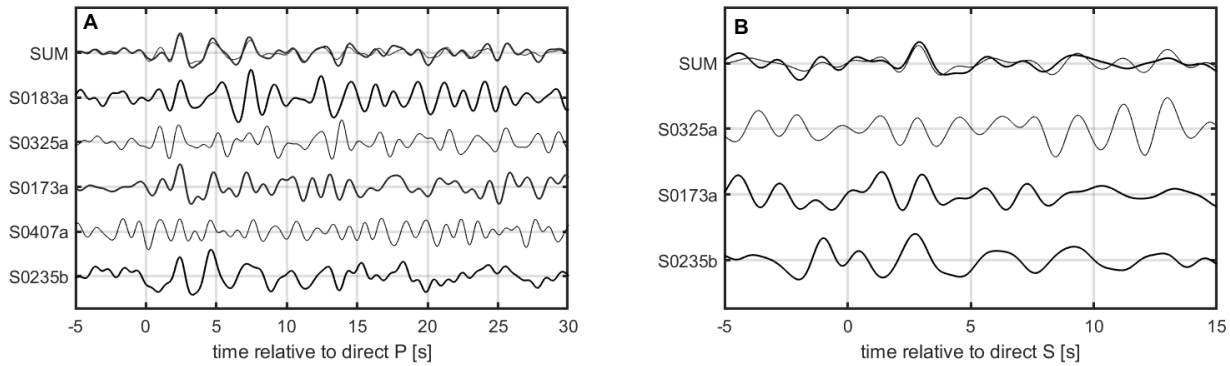


**Fig. S7. P-to-S and S-to-P RFs using method D.** (A) P-to-S RFs for events S0235b, S407a, S0173, S0325a and S0183a. Summed trace either contains only the three best events (S0235b, S0173a, S0183a; thick black line) or all five events (thin black line). (B) S-to-P RFs for events S0235b, S0173a and S0325a. Summed trace either contains only the two clearest traces (S0235b, S0173a; thick black line) or all three events (thin black line).

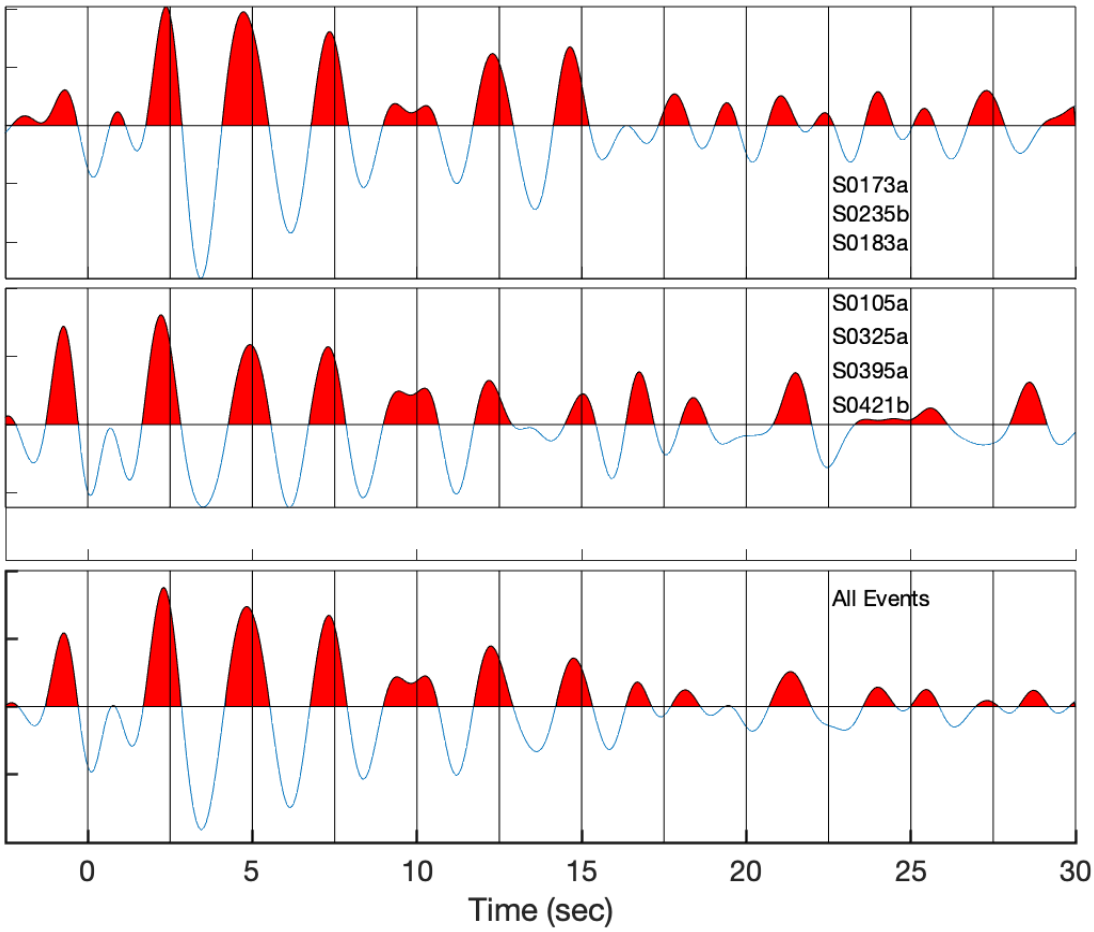


**Fig. S8. Comparisons between stacks of receiver functions computed with method G.** The top stack is $R_{ref}$. The events in the second stack were inverted for azimuth by comparing with $R_{ref}$. The third stack is for all events.

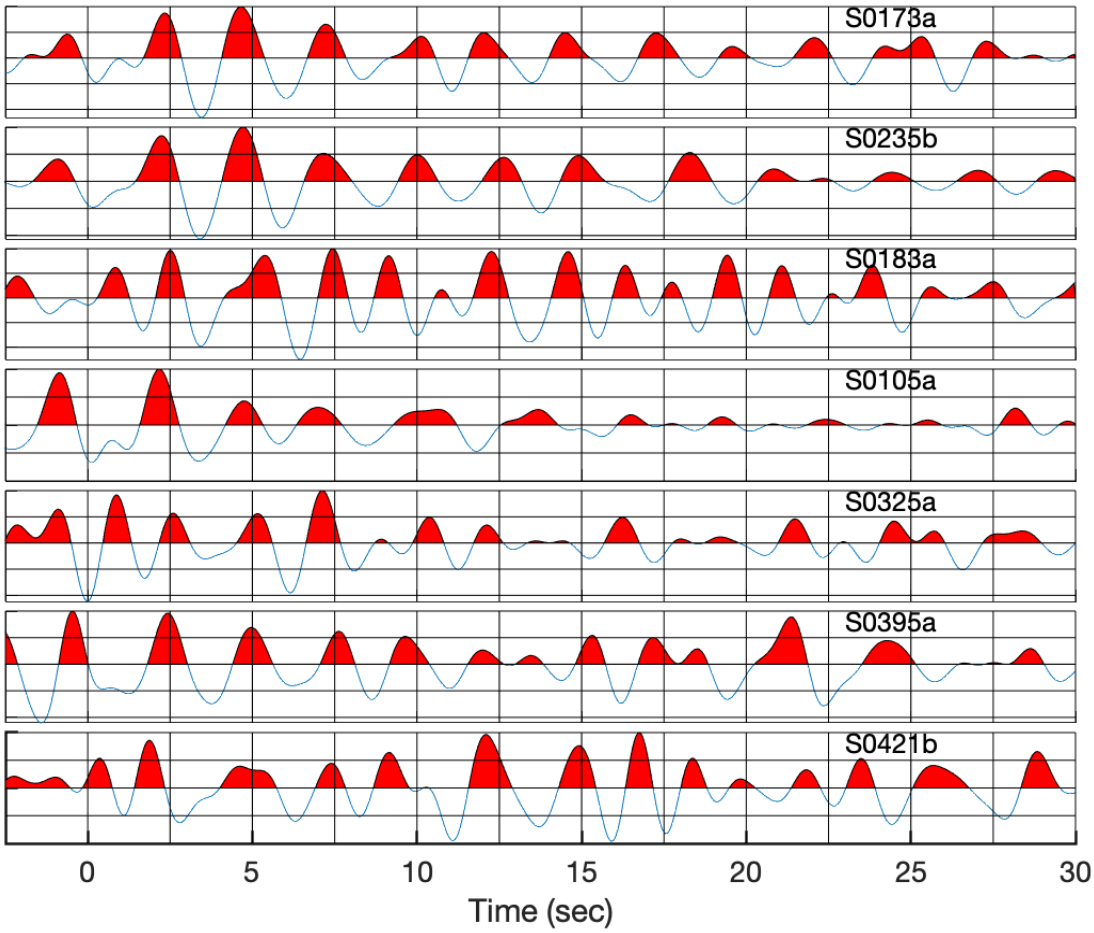


**Fig. S9. Receiver functions for 7-deglitched events marked, using method G.**

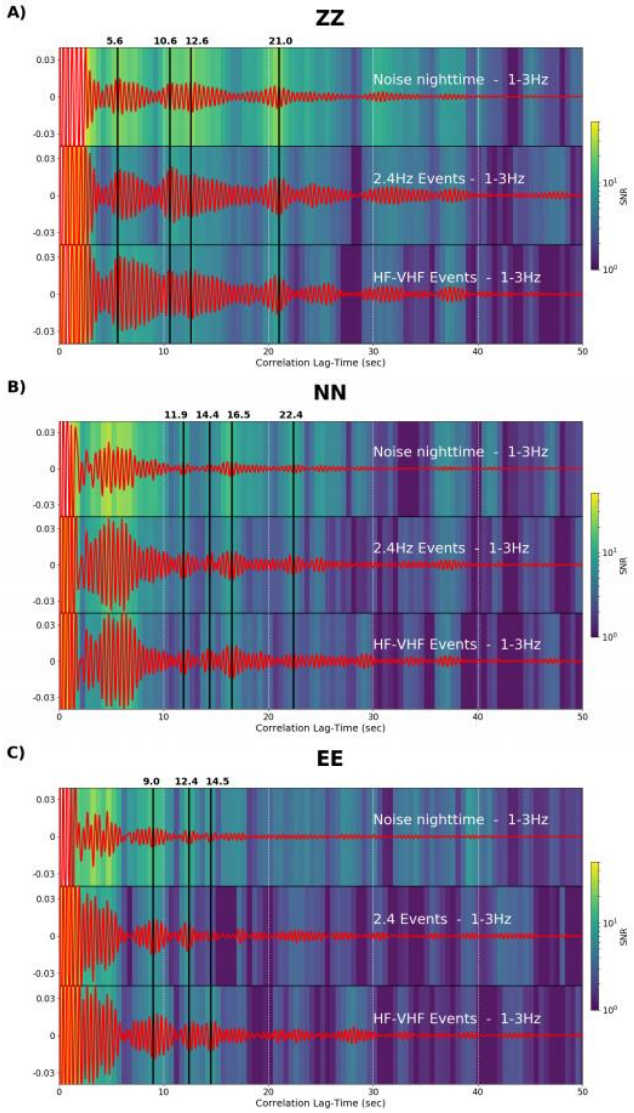


**Fig. S10. Comparison of waveforms (in red) and SNR (color bar) of the ACFs for (A) the vertical (ZZ) component, (B) the North (NN) component and (C) the East (EE) component.** From top to bottom: ACF computed on the ambient noise between 1 Hz and 3 Hz during nighttime (17:00 LMST to 23:00 LMST) (149 SOLs); ACF computed on 2.4 Hz events between 1 Hz and 3Hz (69 events); ACF computed on high frequency (HF) and very high frequency (VF) events between 1 Hz and 3 Hz (55 events). The colored background corresponds to the signal-to-noise ratio (SNR) in logarithmic scale. The various vertical black lines indicate potential energy arrivals corresponding to large amplitudes in the waveforms, and large SNR. (A) On the ZZ component we identify arrivals at 5.6 s, 10.6 s, 12.6 s and 21.0 s. (B) On the NN component we identify arrivals at 11.9 s, 14.4 s, 16.5 s and 22.4 s. (C) On the EE component we identify arrivals at 9.0 s, 12.4 s and 14.5 s.

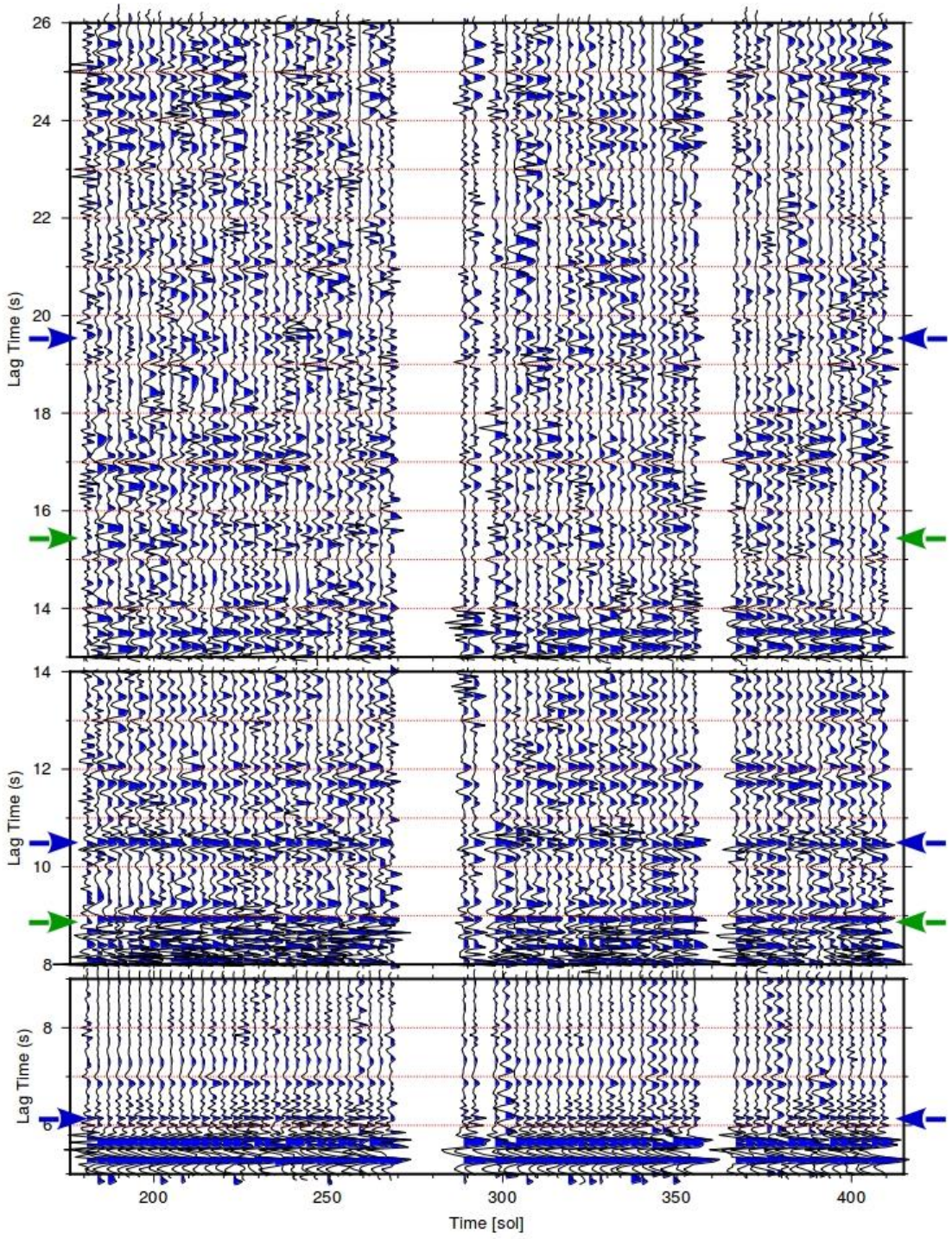


**Fig. S11. Vertical-component noise autocorrelation stacks for sliding three-sol data windows**. The frequency band is 1.2-8.9 Hz and data windows do not overlap. Shown are time-frequency phase weighted stacks of phase autocorrelations. Blue marks negative amplitudes. The blue and green arrows point to expected or observed P-wave reflections and converted P-to-S (and vice versa) reflections. The three lag-time windows have been used to improve the visibility through independent amplitude normalization.

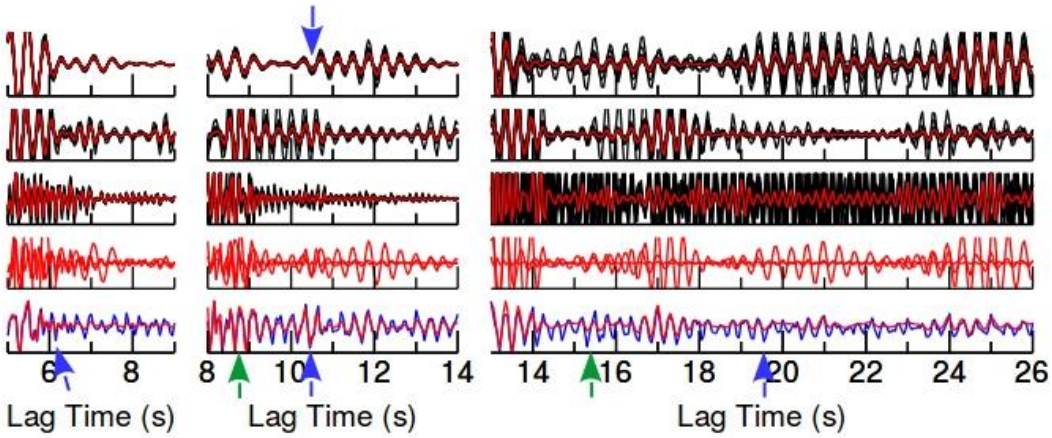


**Fig. S12. Vertical-component noise autocorrelation stacks.** The three lag-time windows correspond to those of Fig. S11 and have been chosen to improve signal visibility. Red and black traces show time-frequency phase weighted stacks of phase autocorrelations. Red and black mark the stacks for all data and subsidiary data sets of 10%, respectively. The first three panels are for 1.5-3.0 Hz, 2.4-4.8 Hz, and 3.6-7.2 Hz band-passed filtered noise. The fourth panel compares the stacks from the top three panels. The lowermost panel shows the linear stack (blue line) and phase weighted stack (red line) of phase autocorrelations in the frequency band 1.2-8.9 Hz. Arrows are the same as for Fig. S11.

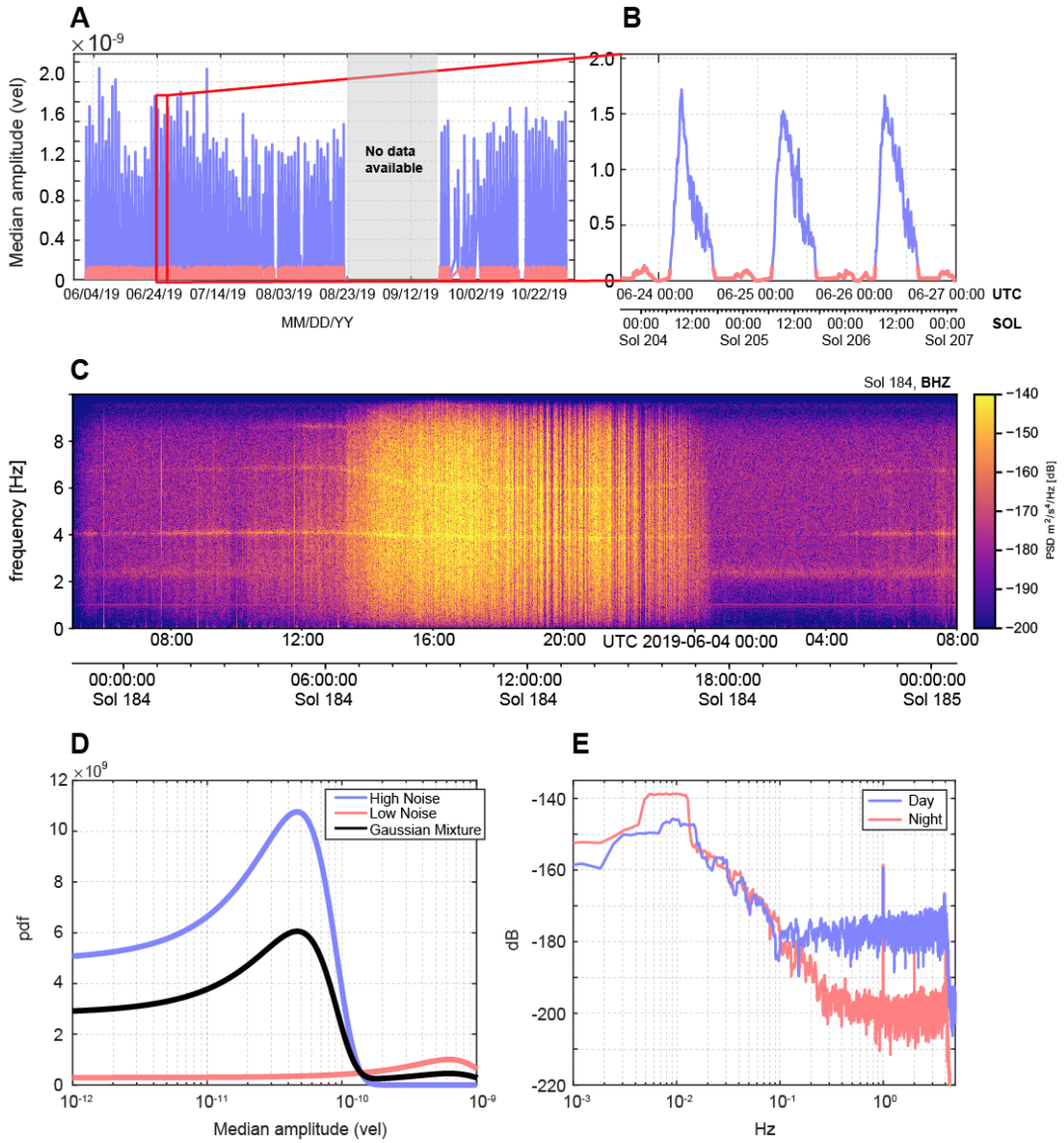


**Fig. S13. Seismic noise recordings at Mars.** (A) Median amplitude of 20 Hz broadband velocity recordings (VBB) during June-November, 2019. Blue and red lines indicate low and high noise level recordings modeled in (D). SEIS data in gray shaded box is not available due to solar conjunction. (B) Outset shows rise and fall of the amplitudes between three sols of recording (June 24-27, 2019). (C) Spectrogram of one sol of SEIS data recorded on the vertical component, showing a clear contrast between the nighttime and daytime signal. During the day, large signals are generated by windy conditions, while at night the signals approach the noise floor of the VBB. Several resonance modes are apparent, including tick noise at 1 Hz (with its overtones) and a potential structural resonance at 2.4 Hz. (D) PDF of a Gaussian mixture model with two components (high and low noise) used for distinguishing day vs. night portions of the data. (E) Average power spectral density of daytime (blue) and nighttime (red) signals. NB: the acronyms for MM/DD/YYYY, UTC, pdf, and PSD refer to month/day/year, universal time coordinated, probability density function, and power spectral density, respectively.

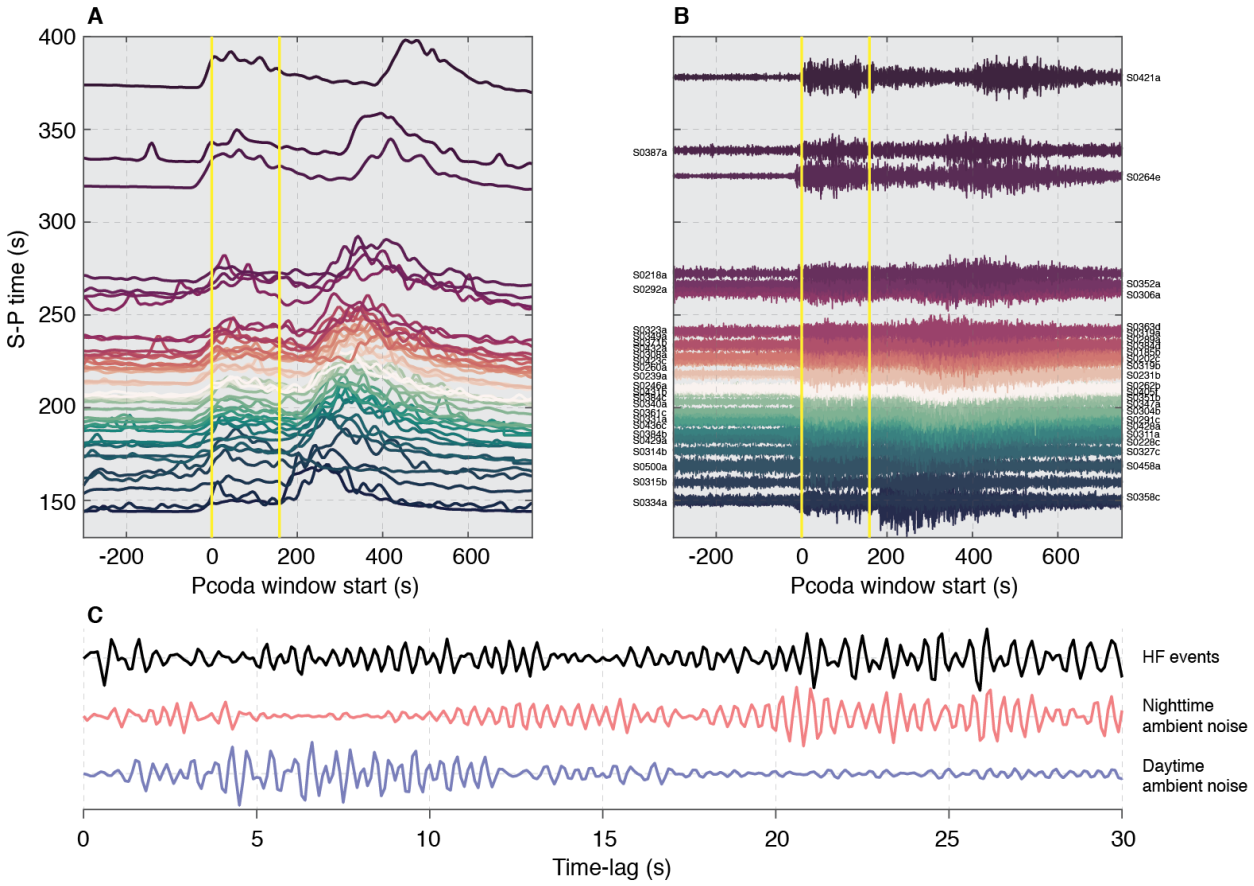


**Fig. S14. HF event data, and comparison of the ACF stacks.** (A) Average three-component envelopes aligned by P arrival from the 48 HF marsquakes analyzed, and the corresponding (B) vertical component waveforms. Yellow lines denote the P-coda analysis windows used in the correlation analysis. (C) Comparison of phase-weighted ACF stacks computed from day- and night-time continuous ambient noise recordings (blue and red, respectively) and P-coda energy from the HF events (black), post-filtered between 1.5-3.0 Hz.

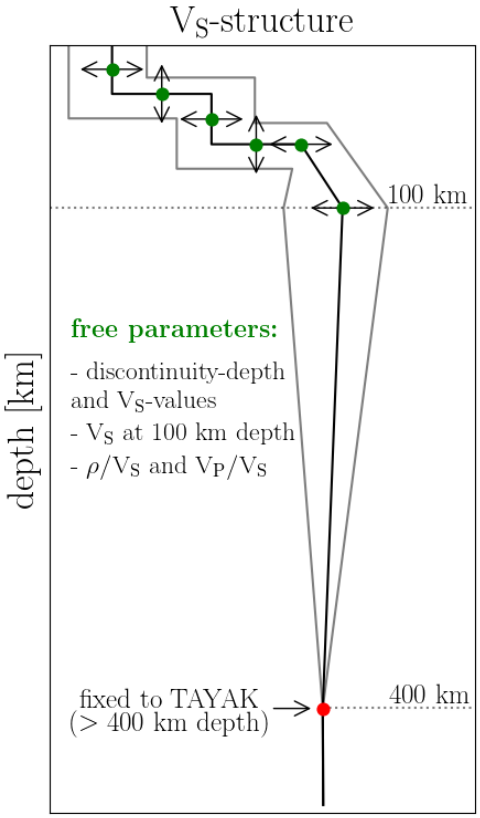


**Fig. S15. Sketch of model parametrization (inversion method A).** The black and grey lines indicate example-profiles of S-wave velocity ($\overline{V_S}$), while free parameters are visualized as green dots in contrast to fixed nodes in red. See text for further explanations.

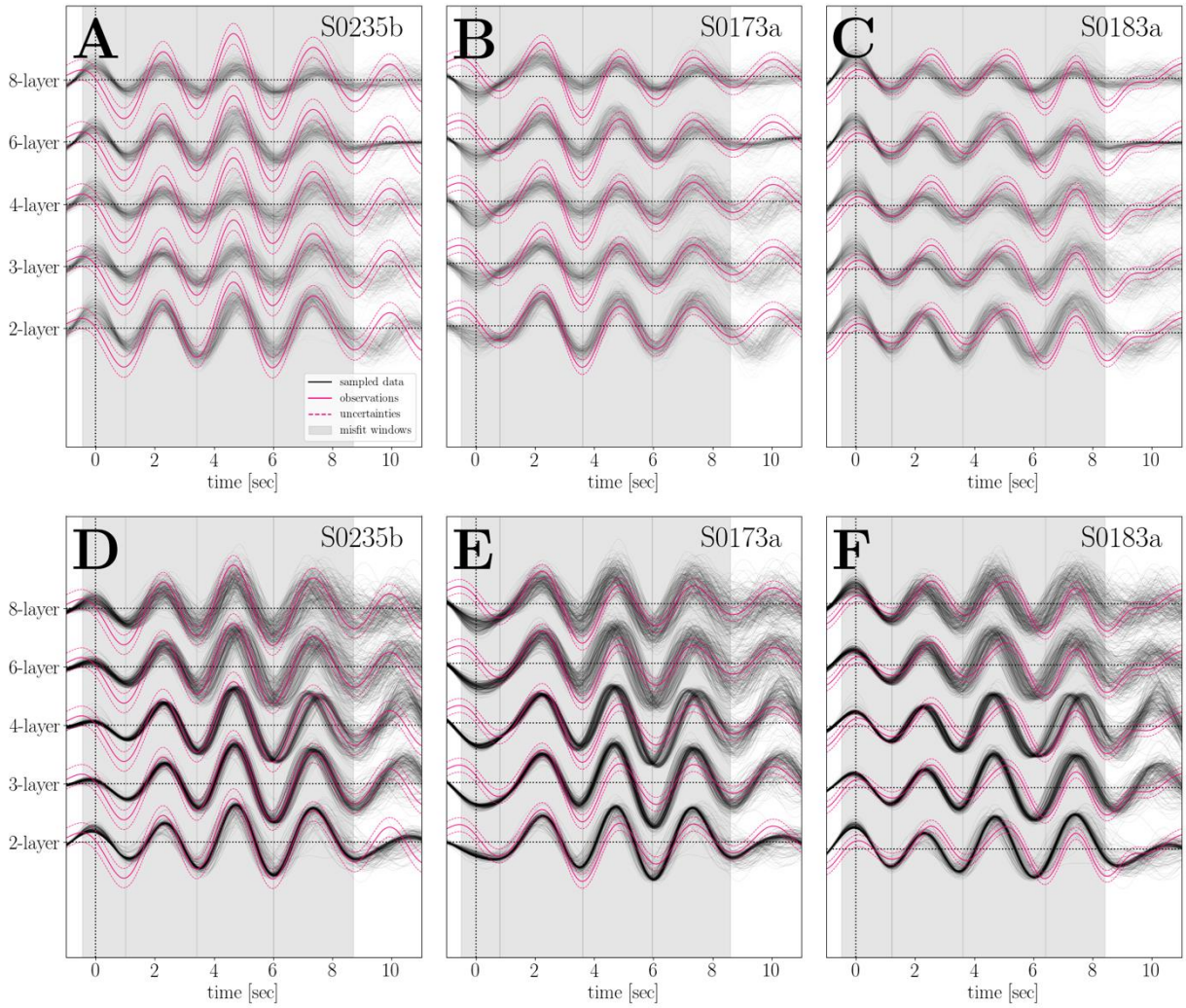


**Fig. S16. Data fit resulting from joint inversions of S0235b (A, D), S0173a (B, E), and S0183a (C, F) low-frequency Ps RFs using inversion method A (top) and B (bottom), respectively.** Inversions differ in the number of crustal layers included (vertical axis). Observed data and their uncertainty bounds are plotted in magenta as solid and dashed lines, respectively. Synthetics picked from the model samples are shown in grey. Grey shaded areas indicate time windows employed in misfit computation.

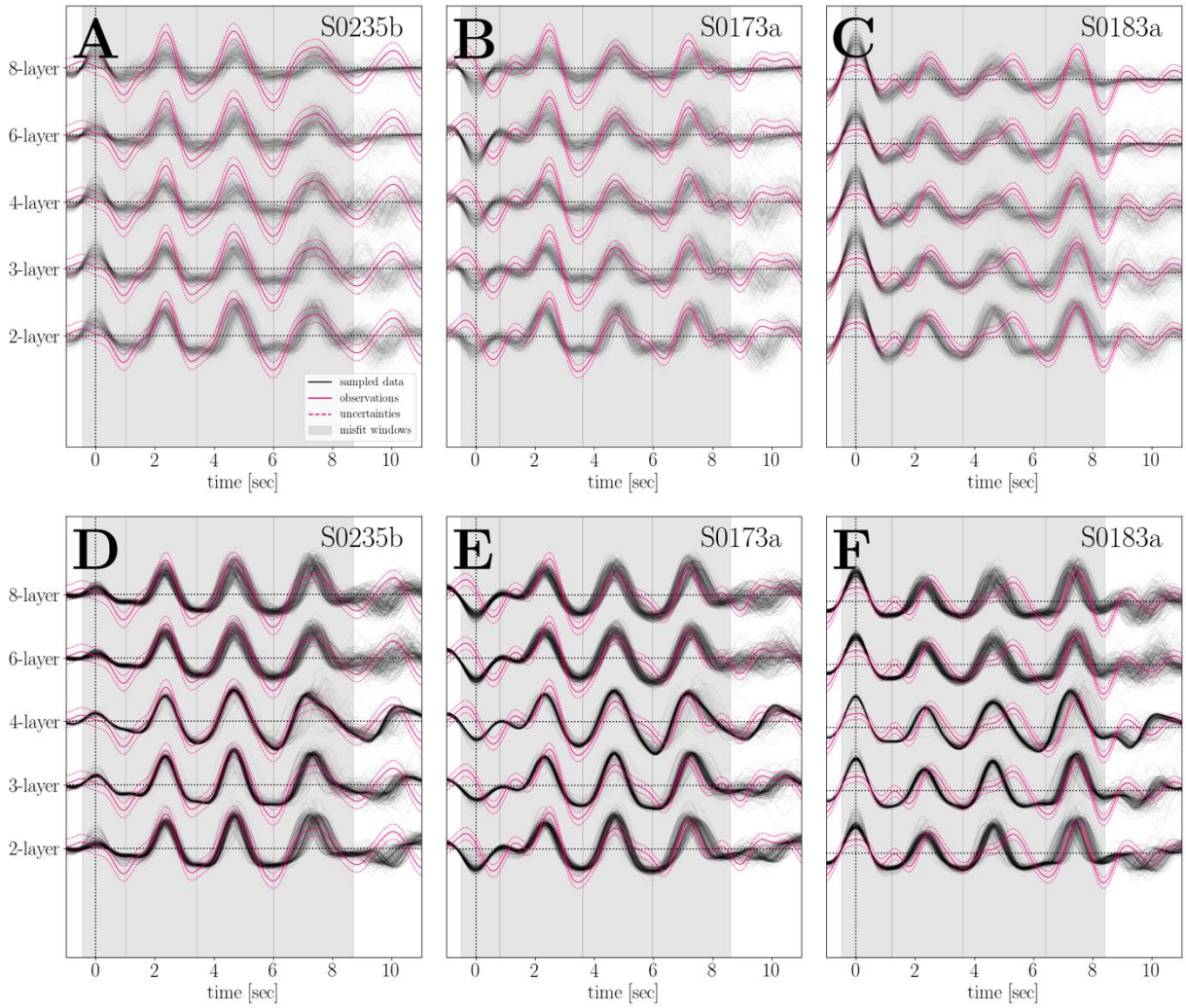


**Figure S17**: **Same as Figure S16, but for high-frequency Ps RFs.**

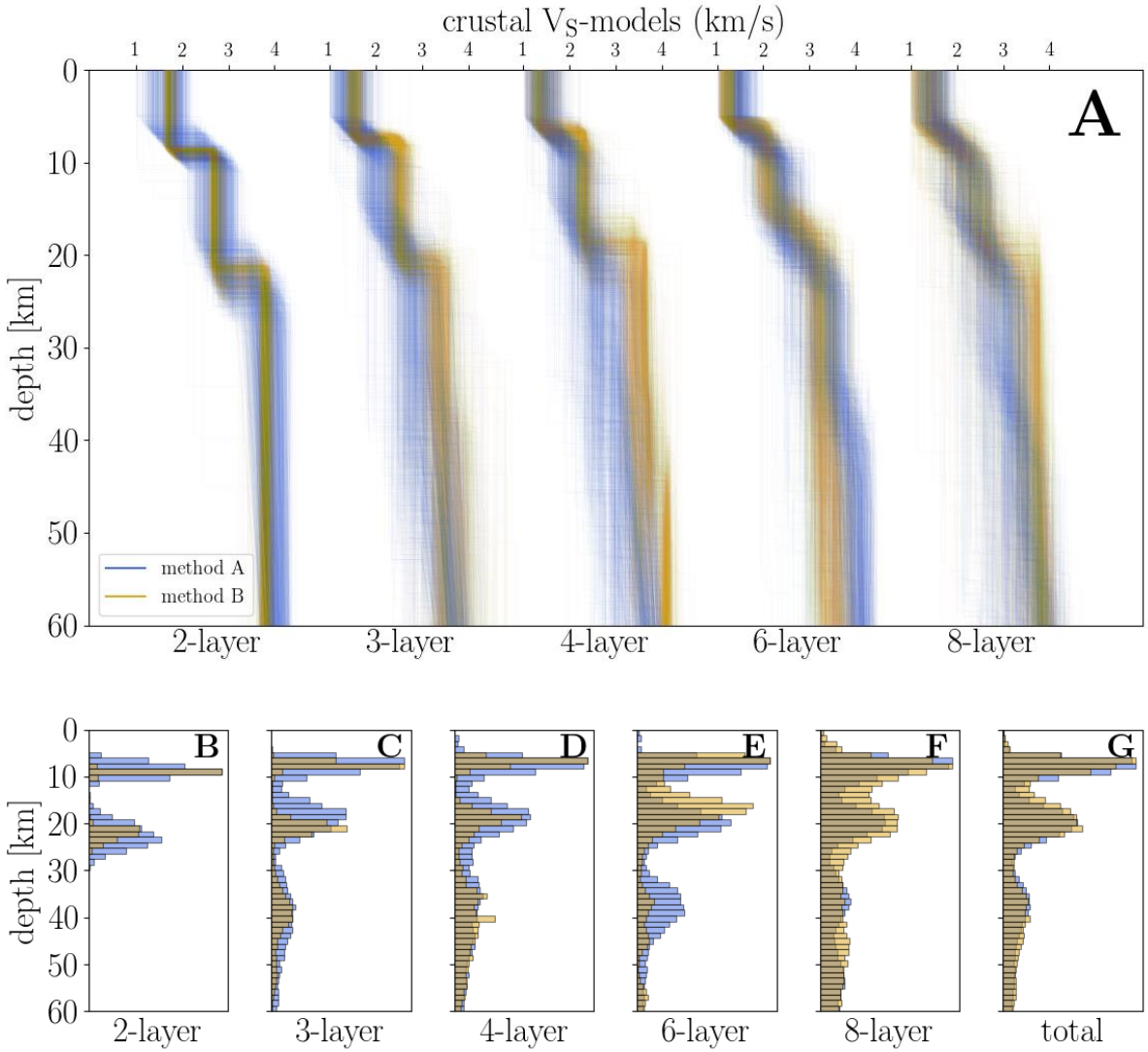


**Fig. S18. A collection of S-wave velocity profiles (A) extracted from the model ensemble from low-frequency Ps RF inversions differing in number of crustal layers for inversion method A (blue) and B (orange), respectively, and corresponding discontinuity-depth histograms (B-G).**

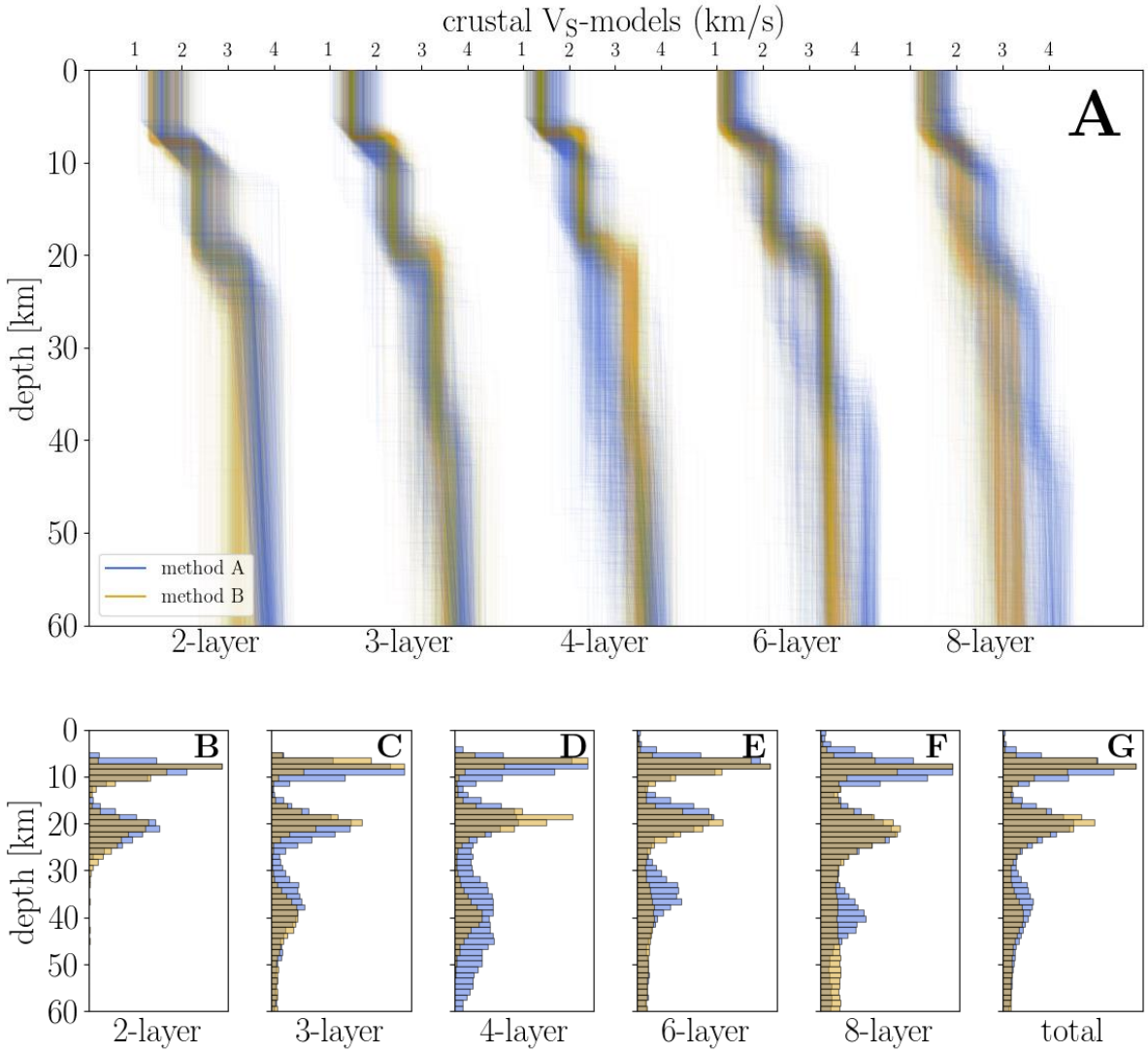


**Fig. S19. Same Figure S18, but for high-frequency inversions**

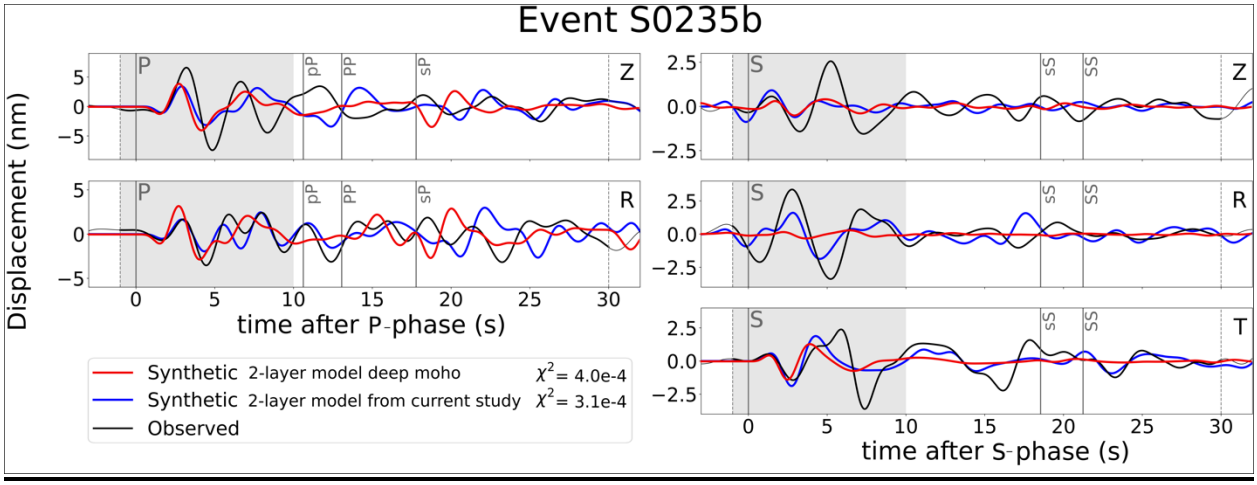


**Fig. S20. Source inversion results for event S0235b (black lines show the recorded data) taken from Brinkman et al. (*82*) for 2 layer-models with the Moho at 80 km (red lines) and 24 km (blue lines)**. The latter model is equivalent to the 2-layer model of this study. The two left panels represent from top to bottom the vertical (Z) and radial (R) component of the P-waveform. The right three panels show from top to bottom the vertical (Z), radial (R) and transverse (T) component of the S-waveform. The dashed gray lines and area present the total length of the inversion window and higher weighted part of the inversion window, respectively. The solid gray vertical lines denote the first arriving P- and S-waves and later-arriving phases (pP, PP, sP, sS and SS) calculated using ray theory. The misfit value ($\chi^2$) for each of the inversion is specified in the legend.

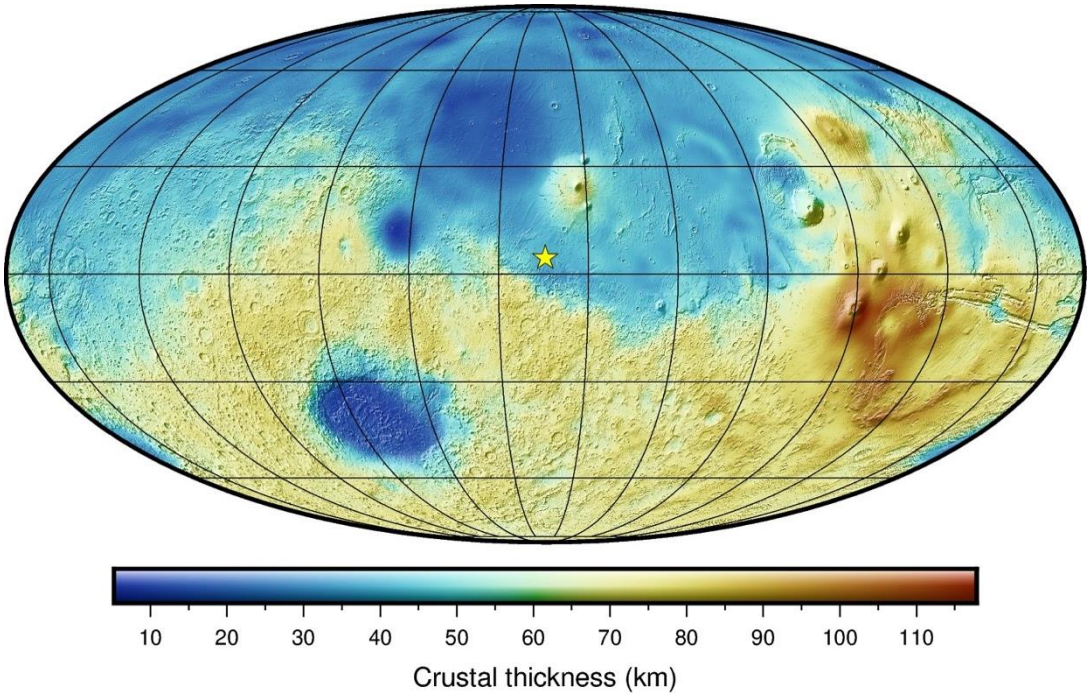


**Fig. S21. A representative global crustal thickness model of Mars.** This model uses the reference interior model of TAYAK (*26*), a crustal density of 2900 kg $m^{-3}$, and an assumed crustal thickness at the InSight landing site of 39 km. The average crustal thickness for this model is 56 km, the minimum thickness is 5 km (located in the Isidis impact basin), and the maximum thickness is 118 km (located in the Tharsis plateau). The yellow star denotes the location of the InSight landing site, grid lines are spaced every 30° of latitude and longitude, and the image is presented using a Mollweide projection with a central meridian of 135.6° E longitude.

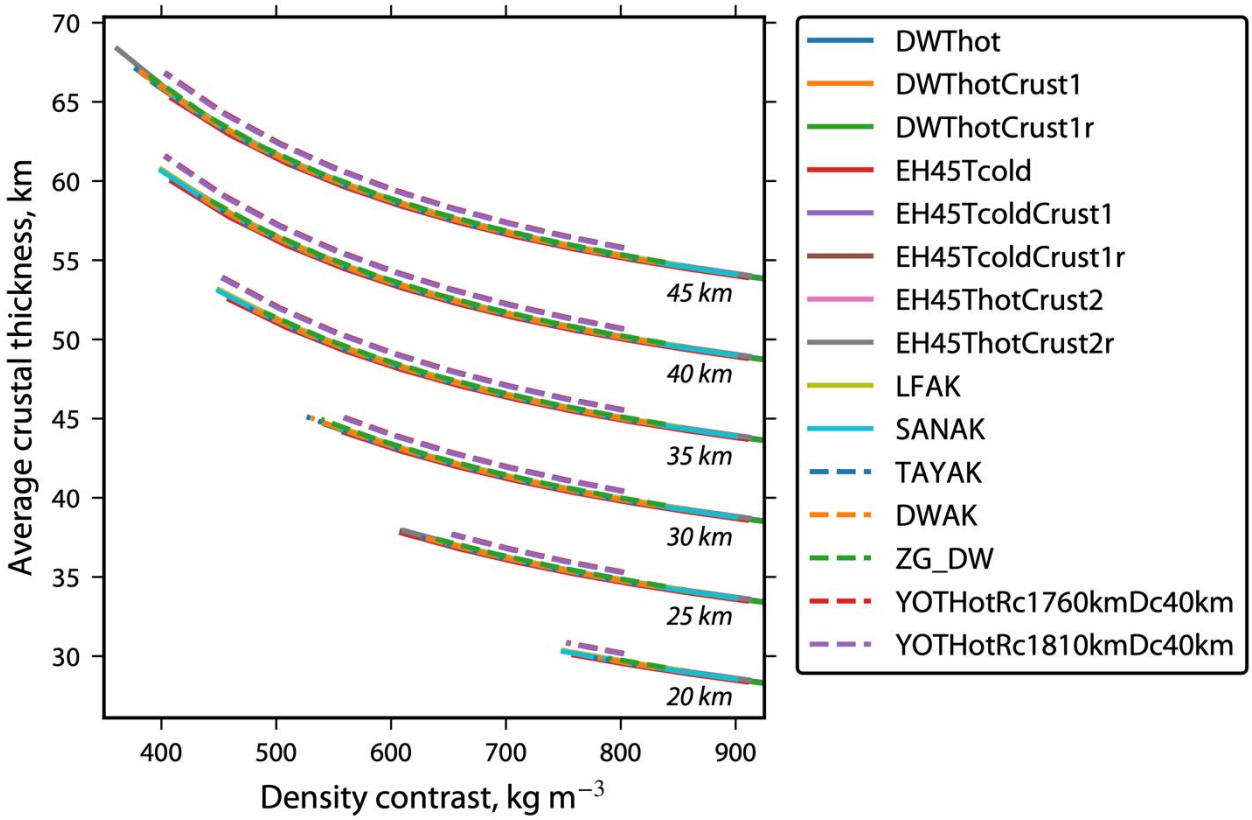


**Fig. S22. Average thickness of the Martian crust as a function of the density contrast across the crust-mantle interface from inversions of global gravity and topography data.** Each curve corresponds to a different reference interior model that specifies the density profile of the mantle and core (legend) and an assumed seismic thickness at the InSight landing site (text annotation). Shown are suites of models for InSight seismic thicknesses from 20 to 45 km. The minimum crustal density is assumed to be 2550 kg m$^{-3}$, and the maximum density is limited by the ability of the model to fit the observed seismic thickness and gravity field. The interior reference models are described in Smrekar et al. (*26*).

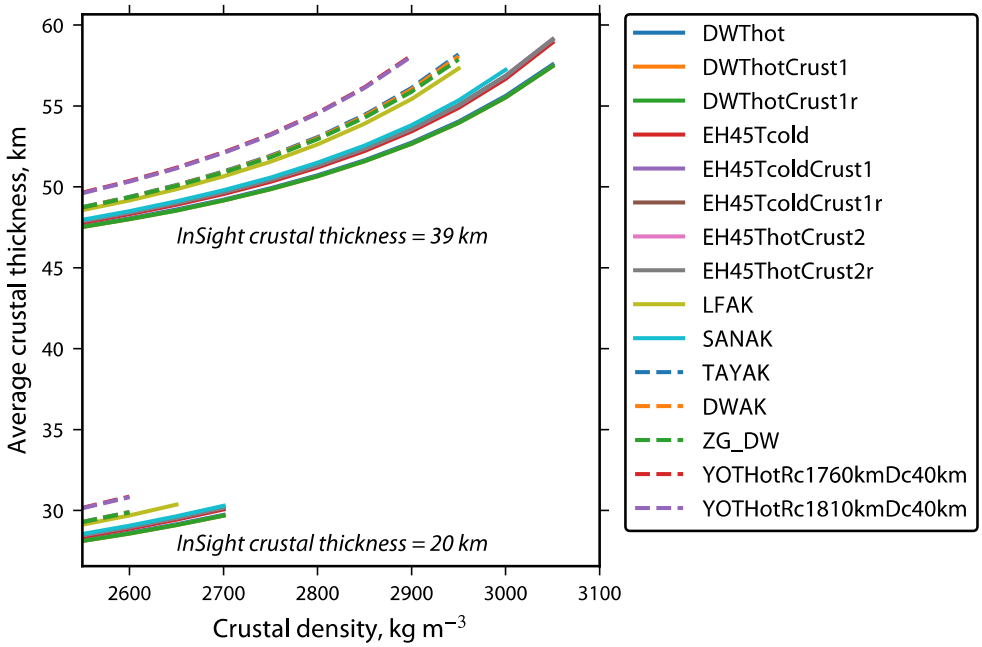


**Fig. S23. Average thickness of the Martian crust as a function of crustal density from inversions of global gravity and topography data.** Each curve corresponds to a different reference interior model that specifies the density profile of the mantle and core (legend). Shown are two suites of models that satisfy two possible seismic thicknesses at the InSight landing site of 20 and 39 km. The minimum crustal density is assumed to be 2550 kg $m^{-3}$, and the maximum density is limited by the ability of the model to fit the observed seismic thickness and gravity field. The interior reference models are described in Smrekar et al. *(26)*.

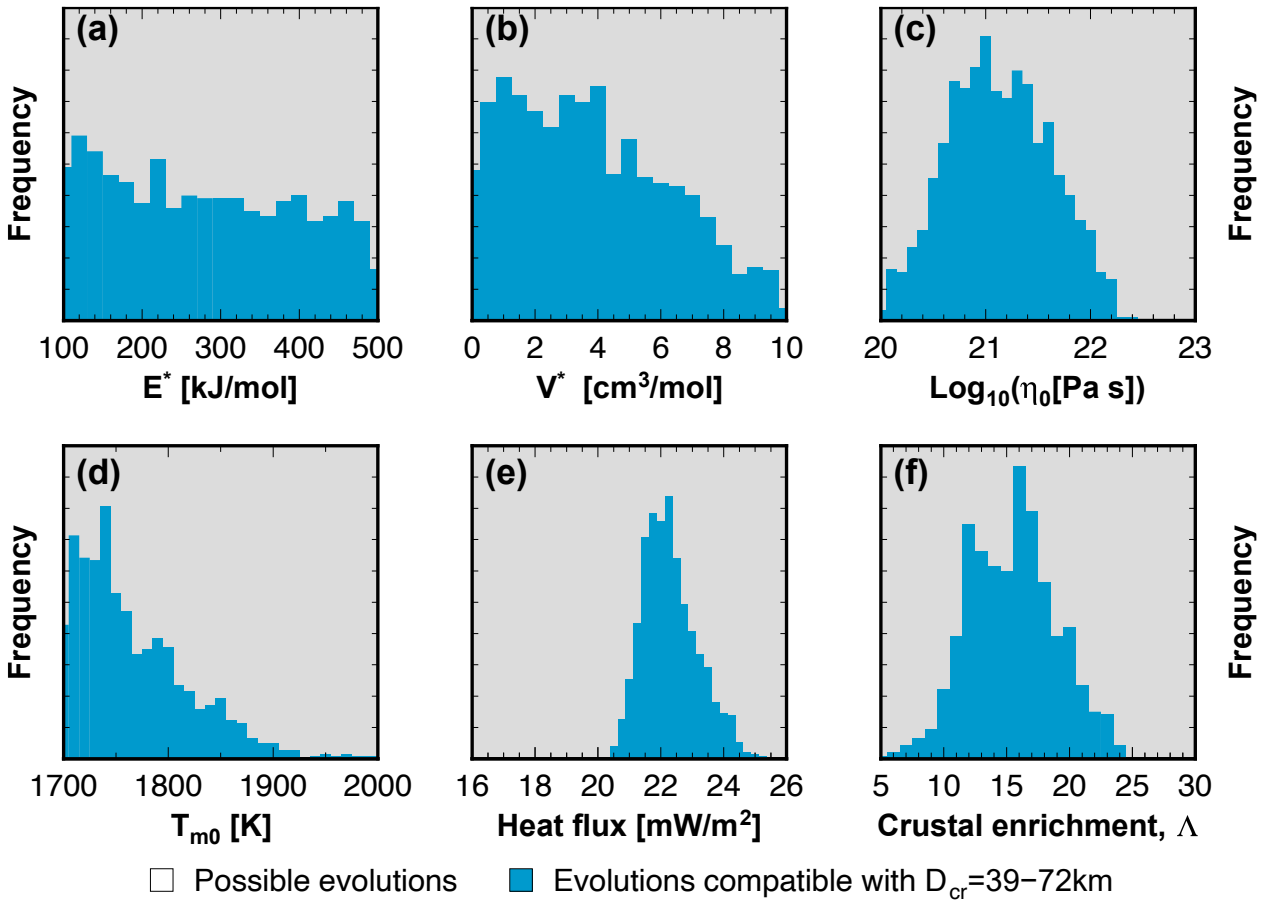


**Fig. S24. Results of the parameterized convection modelling.** Exploration of the parameter space for the thermo-chemical evolution of a Mars-like planet, showing the input governing parameters and output quantities associated with $n$=$10^4$ possible histories and a subset ($n$=$10^3$) of modelled histories that are compatible with a present-day crustal thickness ranging between 39 km and 72 km.

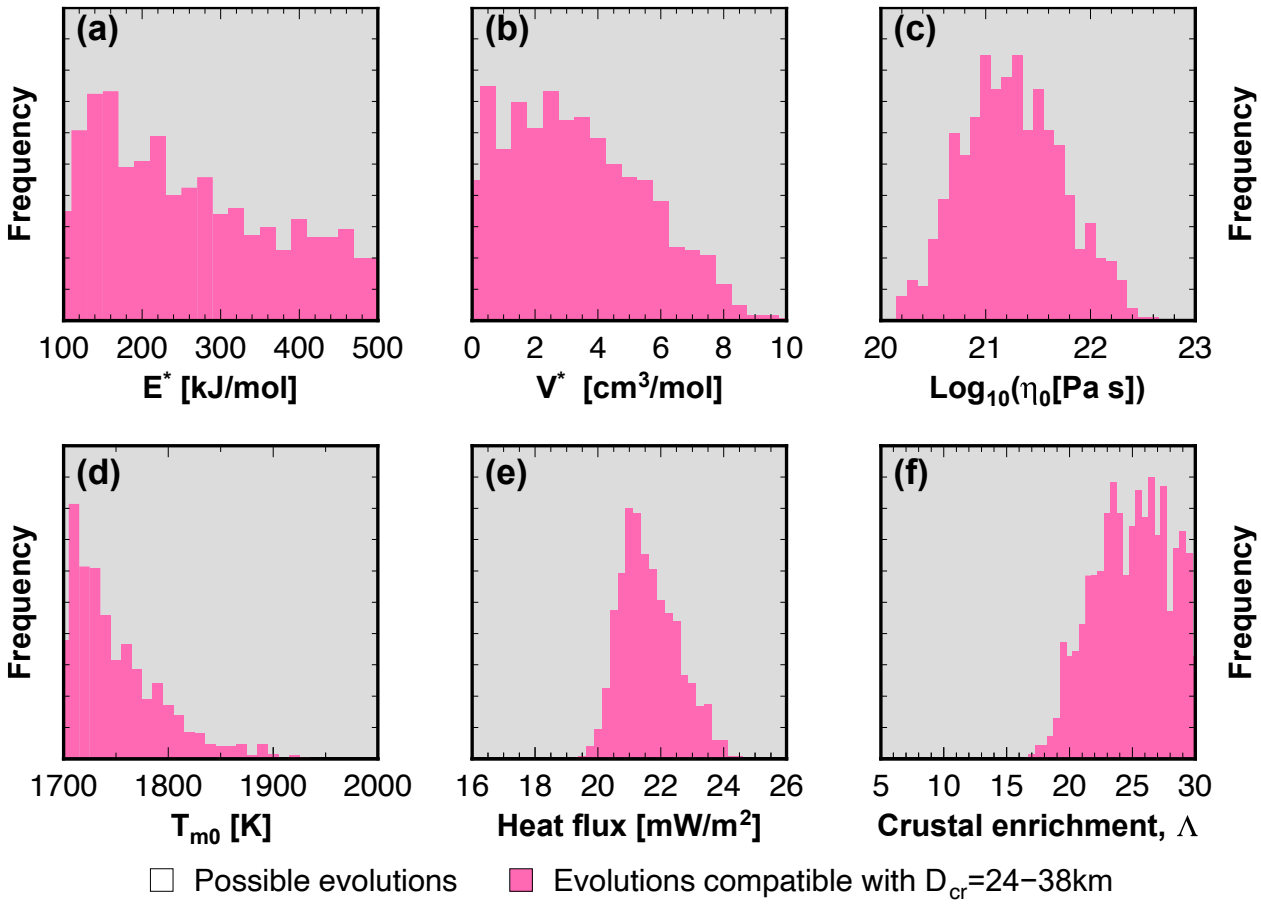


**Fig. S25. Results of parameterized convection modelling.** Exploration of the parameter space for the thermo-chemical evolution of a Mars-like planet, showing the input governing parameters and output quantities associated with $n=10^4$ possible histories and a subset ($n=10^3$) of modelled histories that are compatible with a present-day crustal thickness ranging between 24 km and 38 km.

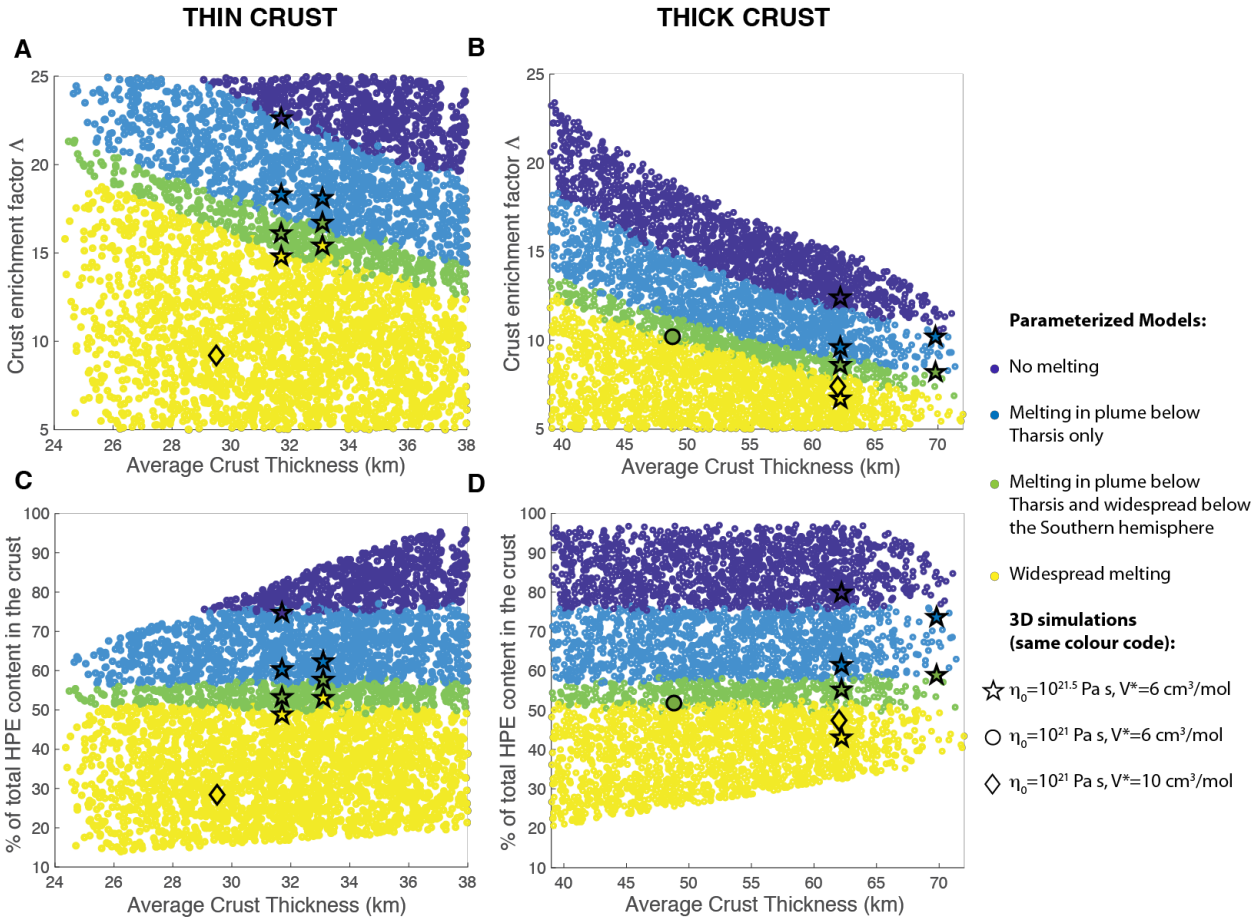


**Fig. S26. Results of parameterized convection modelling accounting for different crustal structures in the geological provinces of Mars, testing for melting in a plume below Tharsis.** 5000 models randomly sampled in terms of crustal density (2550-2850 kg $m^{-3}$ in the thin crust case, 2550-3100 kg $m^{-3}$ in the thick case), northern crustal thickness (16-28 km in the thin crust case, 28-55 km in the thick crust case), these a priori ranges being given by topography and gravity data inversion (Section S5). The crustal enrichment factor Λ is in the range 5-25. The rheology is fixed with a reference viscosity $\eta_0$=$10^{21.5}$ Pa s at $T_0$=1600 K and $E$*=300 kJ $mol^{-1}$, $V$*=*6* $cm^3$/mol. The initial mantle temperature is $T_{m0}$=1800 *K* and the core radius is $R_C$=1850 km. Results for 6 of the 3D simulations indicated on the graph are shown on Fig. S27.

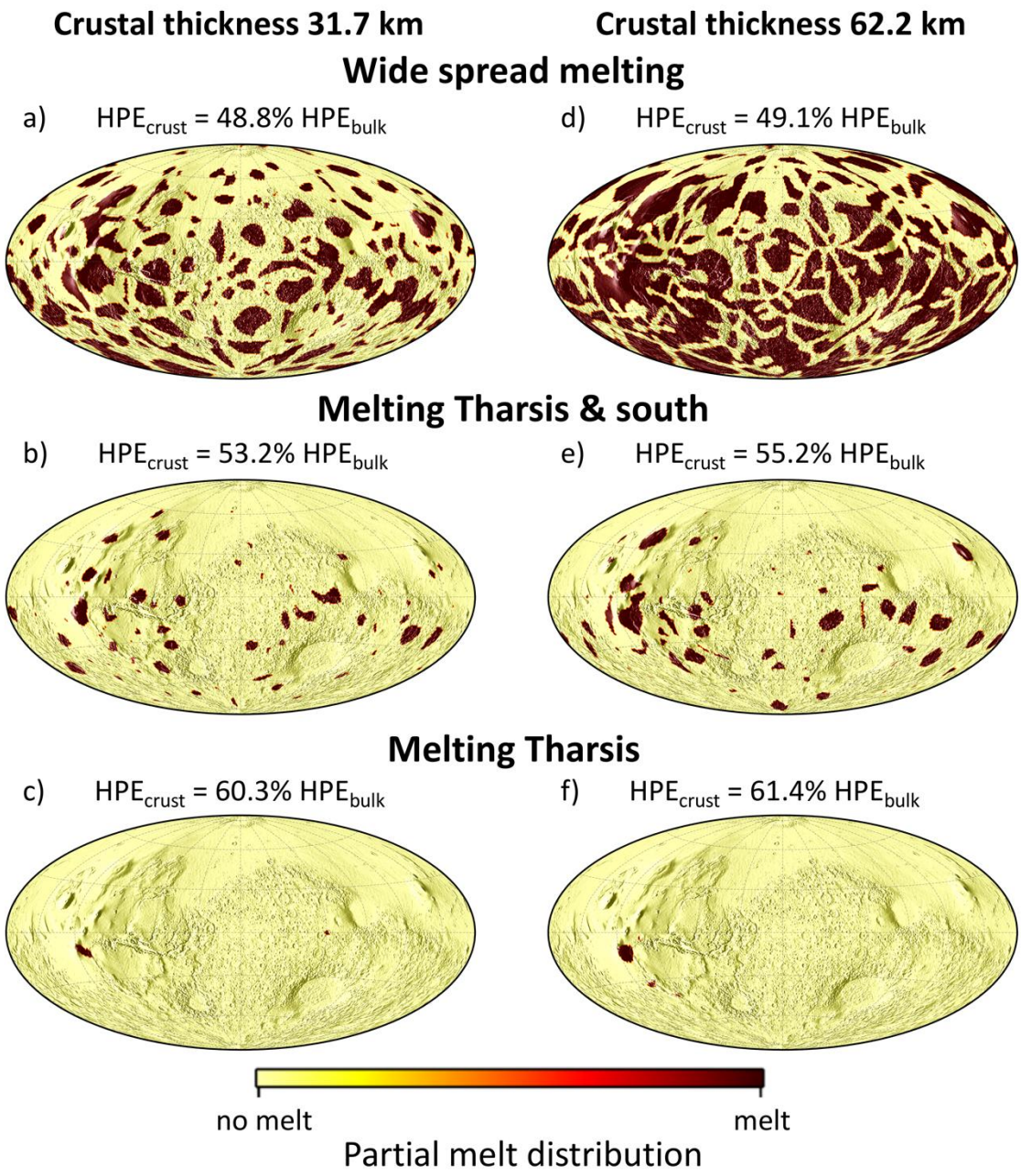


**Fig. S27. Distribution of partial melt produced by mantle plumes in the interior of Mars at present day.** The left column shows the models that employ a thin crust (31.7 km) and contain the following amounts of radioelements in the crust: a) 48.8%, b) 53.2%, and c) 60.3% of the total bulk content. The right column shows models with a thick crust (62.2 km) that contains: d) 49.1%, e) 55.2% and f) 61.4% of the total heat-producing element content. All models use the same parameters as the parametrized thermal evolution models in Fig. S26 and are indicated by star symbols on Fig. S26. The amount of melt reduces with increasing radioelement content in the crust, and the melt distribution becomes confined to smaller regions on the southern hemisphere and finally to Tharsis.

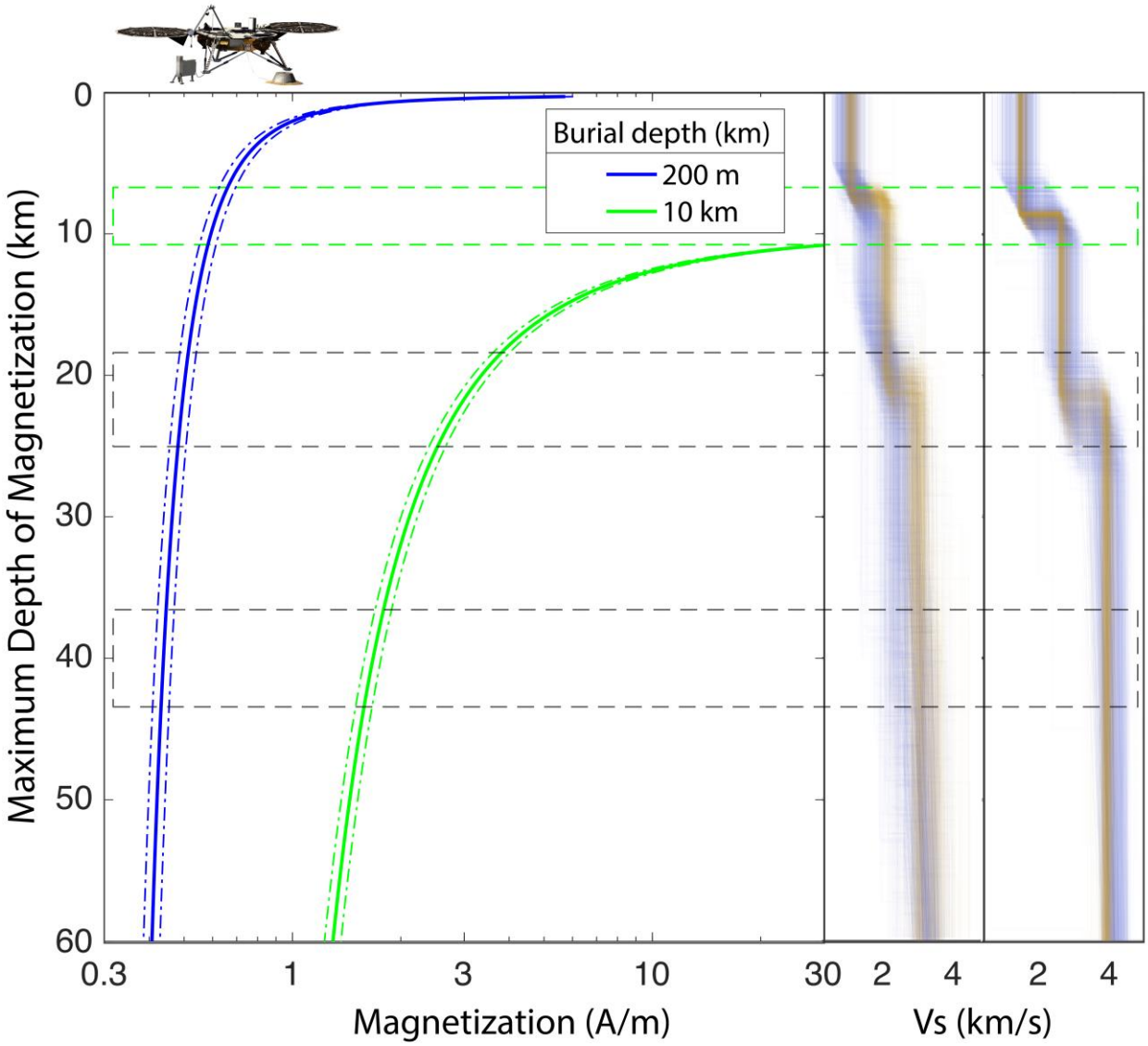


**Fig. S28. Estimation of minimum magnetization.** The minimum magnetization required from a surface field of 2013 nT and the upper and lower 99% confidence intervals on the surface field strength (*107*). Burial depth describes the depth extent of the unmagnetized layers above the top of the magnetized layer. For a burial depth of 200 m (blue), corresponding to burial beneath the young, Amazonian-Hesperian, near-surface lava flows (*107*) magnetizations are ~0.4 A/m if the entire underlying crust is magnetized. A burial depth of 10 km requires magnetizations larger than 1 A/m. The velocity profiles show the range of seismically-determined interface depths as in Fig. 2 of the main paper.

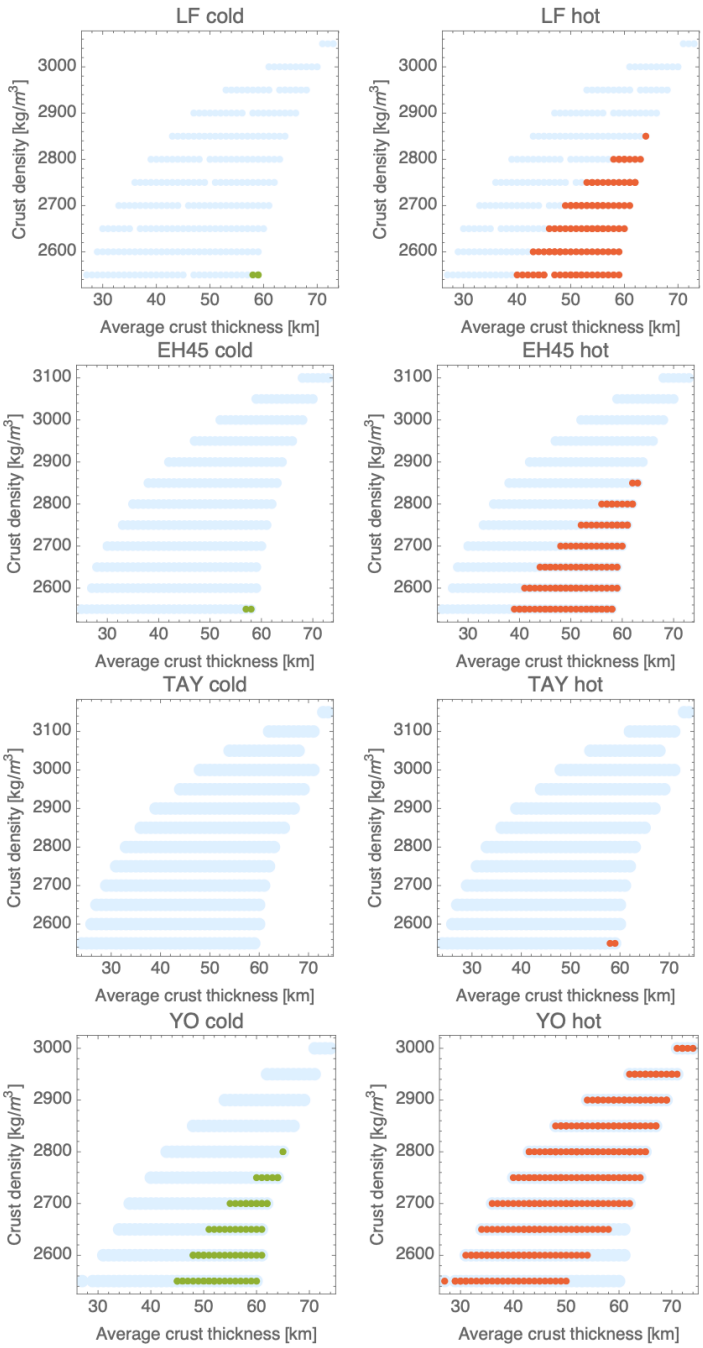


**Fig. S29. Ability of crustal models to match moment of inertia and $k_2$.** Each panel shows the average crust density and thickness pairs (blue dots) resulting from this study for different mantle composition and two mantle temperature end members (hot and cold). The colored dots represent the crust density and thickness pairs of interior structure models that agree with the moment of inertia of Mars and have a core large enough to agree with the tidal Love number $k_2$. Figures are labelled with the composition models discussed in section S5.

| Method | RFs | Rotation angles | Deconvolution method | Length of source window for deconvolution | Filter band [Hz] |
|---|---|---|---|---|---|
| A | P-to-S and S-to-P | MQS backazimuths and free surface transfer matrix for incidence angles *(39)* | transdimensional hierarchical Bayesian *(39)* | 8-9 s after P- or before S-arrival | event dependent: 0.1-1 or 0.1-0.8 for P-to-S, 0.05-0.7 for S-to-P |
| B | P-to-S | principal component analysis for both azimuth and incidence angle | water-level *(41)* | -10 to +25 s around P-wave onset | 0.1-0.9 |
| | | | iterative time-domain *(42)* | | |
| C | P-to-S and S-to-P | MQS backazimuths and principal component analysis for incidence angles | iterative time-domain *(42)* | -20 to +50 s around the P-wave onset -150 to +50 s and -100 to +30 s around the S-wave onset | 0.1-0.5 (low-frequency), 0.125-1 (high-frequency) |
| D | P-to-S and S-to-P | MQS backazimuths and principal component analysis for incidence angles | Wiener filter *(43,44)* | event dependent, between 28 and 40 s after P- or before S-arrival | event dependent: 0.1-0.8 or 0.3-0.8 |
| E | P-to-S | MQS backazimuths and principal component analysis for incidence angles | iterative time domain *(42)* | 30 s around P-wave onset | 0.1-1 |
| | | | extended-time multi-taper deconvolution *(45)* | 50 s around P-wave onset | |
| F | P-to-S | MQS backazimuths and incidence angles from D | iterative time domain *(42)* | -15 to +80 s around the P-wave onset | event dependent: 0.1-0.8 or 0.3-0.8 |
| G | P-to-S | MQS backazimuth and | water-level *(41,47)* | -3 to + 30 s around the P-wave onset | 0.25-0.8 |

| | | | | | |
|---|---|---|---|---|---|
| | | incidence from ray parameter and assumed near-surface velocities | | | |

**Table S1. Summary of processing methods and parameters used by different groups to compute RFs.**

| Data set / lead team | SEIS sensors | Sol range | Number of events | Pre-processing | Comments |
|---|---|---|---|---|---|
| Continuous Noise Analysis / ISAE-IRAP | three components VBB-VEL channels | 222 to 399 | N.A. | Tick-noise and glitch removal | Deglitch by ISAE |
| HF events / ISAE-IRAP | three components VBB-VEL channels | N.A. | 41 | Tick-noise and glitch removal | Deglitch by ISAE / Event quality: B and C |
| VHF events / ISAE-IRAP | three components VBB-VEL channels | N.A. | 14 | Tick-noise and glitch removal | Deglitch by ISAE / Event quality: B and C |
| 2.4Hz events / ISAE-IRAP | three components VBB-VEL channels | N.A. | 69 | Tick-noise and glitch removal | Deglitch by ISAE / Event quality: B and C |
| Continuous Noise Analysis / CSIC, IPGP | vertical component VBB-VEL channel | 178 to 410 | N.A. | Data selection based on RMS amplitude; band rejection filtering to remove lander modes and tick noise | PCC, linear and tf-PWS stacks |
| Continuous Noise Analysis / UMD | vertical components VBB-VEL channels | 123 to 301 | N.A. | Glitch removal: moving median or comb filter to remove tick noise | Consider day time vs. night time data |
| HF events / UMD | three components VBB-VEL channels | N.A. | 48 | moving median filter to remove tick noise | Event quality: B and C |

**Table S2. Summary of data sets and processing used by different groups to compute ACFs.**

| Description | Parameter | Quantity | Prior range |
|---|---|---|---|
| Crustal layer thickness (km) | $\delta z$ | $N_{lay}$ | 0.1-50 km<br>$\sum_j \delta z_i < 100\ km$ |
| S-wave velocity of uppermost crustal layer (km/s) | $V_S^0$ | 1 | 1.0-4.0 |
| S-wave velocity jump across crustal discontinuities (km/s) | $\delta V_S$ | $N_{lay}$ | 0.0-1.5 |
| S-wave velocity at 100 km depth (km/s) | $V_S^{100}$ | 1 | 4.0-4.5 |
| Density- and P-to-S-wave velocity crustal ratios | $\rho/V_S$ | 1 | 0.7-0.9 |
| | $V_P/V_S$ | 1 | 1.7-1.9 |
| Source depth (km) | $Z_{src}$ | 1 | 40-100 |
| Epicentral distance (°) [cf. Giardini et al., *21*] | $\Delta$(S0235b) | 1 | 25-30 |
| | $\Delta$(S0173a) | 1 | 25-30 |
| | $\Delta$(S0183a) | 1 | 40-60 |
| total | | $8 + 2 \cdot N_{lay}$ | |

**Table S3. Overview of model parameters and the range of the uniformly distributed prior values for RF inversions described in section 3.1.** $N_{lay}$ denotes the number of crustal layers used in the crustal parametrization.

| Parameter | Range |
|---|---|
| layer depth (km) | 0-100 |
| S-wave velocity (km/s) | 1 - 5 |
| $V_P/V_S$ ratio | 1.5 - 2.1 |

**Table S4. Parameter range used in the inversion of RFs with method B (section S3.2).** The same limits were used for all the layers in the respective model parameterization, and – for the velocity ranges – the half-space.

| Parameter | Meaning | Range |
|---|---|---|
| $E^*$ | Mantle effective activation energy | 100-500 kJ/mol |
| $V^*$ | Mantle effective activation volume | 0-10 $cm^3$/mol |
| $\eta_0$ | Mantle reference viscosity | $10^{20}$-$10^{23}$ Pa s |
| $\Lambda$ | Crustal HPE enrichment | 5-30 |
| $Tm_0$ | Initial uppermost convecting mantle temperature | 1700-2000 K |
| $Tc_0$ | Initial CMB temperature | $Tm_0$ + [100-300] K |

**Table S5**. **Ranges considered in the governing parameter space for the exploration of the thermo-chemical history of a Mars-like planet.** See text for further details.

| | K (μg g$^{-1}$) | Th (μg g$^{-1}$) | U (μg g$^{-1}$) | Λ | Reference |
|---|---|---|---|---|---|
| ***Martian crust*** | | | | | |
| Bulk crust | 3,740 | 0.70 | 0.18 | 8.7 – 10.6 | *31* |
| "GRS crust" | 3,300 | 0.62 | 0.16* | 7.8 – 9.5 | *117* |
| 2-layer crust | 8,240 – 9,210 | 1.51 – 1.69 | 0.43 – 0.48 | 22 | |
| 3-layer crust | 4,132 – 5,861 | 0.76 – 1.08 | 0.22 – 0.31 | 12 – 14 | |
| ***Martian primitive mantle*** | | | | | |
| Wänke & Dreibus | 305 | 0.056 | 0.016 | | *29* |

*-assuming Th/U=3.8.

**Table S6. Estimates of HPE concentrations in the Martian crust and primitive mantle.** The conversion between the enrichment factors and concentrations of heat producing elements has been calculated assuming a bulk density of 3500 kg/m$^3$. For the crustal density the range of 2550-2850 kg m$^{-3}$ and 2550-3100 kg m$^{-3}$ has been used for the 2-layer and 3-layer crust, respectively.